Structure-Property Relationships for Energy- and Charge-Transfer Processes

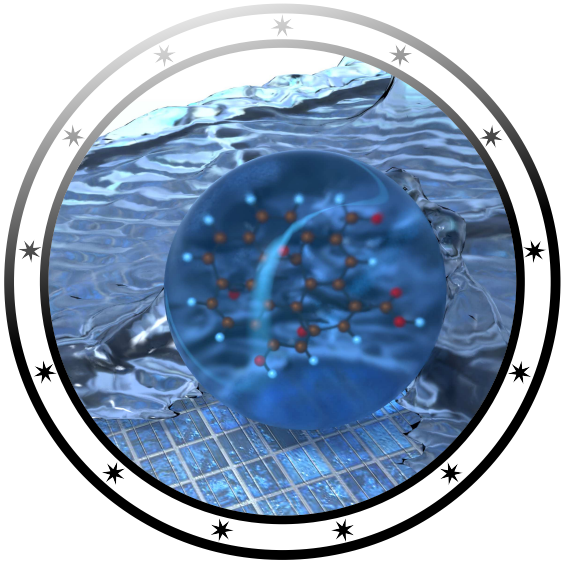

Inaugural-Dissertation

to obtain the academic degree

Doctor rerum naturalium (Dr. rer. nat.)

submitted to the Department of Biology, Chemistry, and Pharmacy
of Freie Universität Berlin

by

Fabian Weber

Berlin, 2019

This work was prepared under the supervision of
Dr. Annika Bande at the Helmholtz-Zentrum Berlin
from October 2015 to December 2019.

Second Examiner : Prof. Dr. Beate Paulus

Date of Defense : 28.1.2020

"Our lives are not our own. We are bound to others, past and present, and by each crime and every kindness, we birth our future."

- David Mitchell, *Cloud Atlas*

To everyone that helped me in becoming who I am today.

Acknowledgements

An effort as large as a PhD research project is one that cannot just be accomplished by a single individual, but which is instead a large group effort involving colleagues, mentors and mentees, as well as family and friends. Therefore, I would like to spend a fair moment to acknowledge all the hours that others spent on helping me taking this next step on my journey. A good way to convey what I mean and to say "thank you" could be by explaining what the German word that describes the PhD candidate phase "Promotion" means to me.

In its more practical sense, the word means the promotion of an individual into the ranks of PhD (*philosophiae doctor* - "wisdom-loving scholar"). To me, this meaning of "Promotion" reflects a long-living tradition in science, in which one generation of scholars passes on the art of how to conduct research onto the next by teaching "how to ask questions", "how to answer them" and "how to present findings in an understandable way". These three most noteworthy disciplines and many more, then make up the pillars of what is called good scientific practice and which is what the PhD candidate is repeatedly challenged to display. These traditions, however, are in principle self-enacted rules without an immediate gain for the individual - but which serve to repeatedly renew the public trust in the independence of science. Especially in times, where lots of misinformation are spread for personal gain, I believe that this safe haven of trustworthy information has gained more weight than ever and needs to be protected. Thus, I would like to thank my supervisors Annika Bande and Beate Paulus for their continued trust in me over these years and their efforts to support and guide me in becoming a wisdom-loving scholar myself.

More importantly in my opinion, though, the word carries the meaning of "promoting an idea". In this sense, I think everyone who ever tried to start something new by themselves - regardless of how big or small that something was - realized at some point that this path is often paved with insecurities, doubts and sometimes even rejections about whether their idea or approach was good, practicable or understandable. In such cases, it is important to have a group of peers who try to understand your perspective on things, such that one can then search for flaws in the presentation or approach together. This continued support then also helps building trust in ones own capabilities and allows for true growth. At the same time, the seniors of the group can offer their experience to the candidate such that one can learn also new methods and techniques. Since this kind of support is mostly happening behind the scenes of all projects, I would therefore like to use this opportunity to thank all colleagues in and outside of my group

for sorting out ideas with me and for spending hours of discussions that helped me in finding a way to present my work in a more understandable way. In this regard, I especially want to thank my senior colleagues M. Berg and P. Krause who taught me how to enjoy a good scientific discussion.
Finally, in face of all scientific (and also non-scientific) challenges we all remain human beings. So as to prevent myself from experiencing a "critical data overflow", both colleagues, friends and family were regularly keeping me company and shared their everyday struggles with me to help me regain my focus. Especially in times where my work (and consequently also mood) was throwing me for loops of "inexplicable oscillations", you weathered with me and helped me in sorting out my troubles. I therefore want to thank everyone that patiently lent me their ears and helped to pull through the weights during all these times.

Summary

The study of structure-property relationships is one of the key steps in developing efficient materials for challenging processes of our time, e.g. energy conversion and charge-transfer processes. In this regard, especially computer simulation techniques that enable insights on an atomistic scale are a powerful tool for finding new ways of improving material properties. However, since such predictions become increasingly difficult to perform depending on factors like energy gauges, extended system sizes and timescales of the processes, highly advanced simulation techniques and carefully selected model systems are required. In this dissertation, three examples for studying material properties on different timescales (nanoseconds to femtoseconds), energetic regimes (infra-red to X-ray response) and system sizes (nanoscopic to molecular) are presented for applications in energy and charge-transfer-related technologies.

In the first study, the aim is to find the best-possible arrangement for a pair of charged quantum dots that drive the interatomic Coulombic decay (ICD) process after excitation with infra-red light. In this process, one of the charged quantum dots is excited by an external field to drive an electron ejection from a neighboring quantum dot. For describing such a highly correlated system of several nanometers in size including electron transitions into the continuum, the effective mass approximation (EMA) is applied and the very flexible multi-configurational time-dependent Hartree (MCTDH) electron dynamics description is utilized. Upon quantum dot size variations, it is found that there exists an intricate balance between the polarization of the electron cloud within the quantum dots and the Coulomb repulsion between them, which drives the process. This balance leads to general curves of size ratios that lead to maximum ICD rates for a given distance between the quantum dots.

In a second project, the capabilities and limitations of a database approach are explored for interpreting X-ray absorption (XA) responses of amorphous substances. The approach is based on the fact that the absorption spectrum of any material can be obtained as a sum of all individual atom's responses in their exact environment. By establishing a database of XA fingerprint spectra for carbon atoms in unique surroundings up to a fixed radius, the most prominent oxidized functional groups are identified in different experimental samples of graphene oxides. The database of XA spectra is obtained by applying time-dependent density functional theory (TDDFT) calculations of local excitations in arbitrarily functionalized graphene oxide model molecules. The non-local effects following such high-energy excitations are shown to be in principle recoverable by expanding the radius for distinguishing the unique surroundings in this

database. Conclusively, the method is suitable for extracting local structural patterns from amorphous materials.

At last, the first partial reaction of the photochemical water-splitting on the edge of nitrogen-doped graphene oxides (NGO) is investigated. In this proton-coupled electron transfer (PCET), one electron and one proton of the water molecule are transferred onto the NGO catalyst in a concerted way. By performing TDDFT calculations on a large set of model molecules, the structural characteristics that lead to an efficient charge transfer are identified. Therefore, time-dependent configuration interaction (TDCI) calculations are applied for the electron dynamics that include explicit non-adiabatic coupling terms describing the hydrogen transfer. The results show that structures with conjugated ketone groups in the vicinity of the proton-accepting nitrogen atom are especially well suited for the electron transfer. Furthermore, the rate of the overall PCET process is strongly limited by the initial electronic excitation dynamics.

Zusammenfassung

Der Zusammenhang zwischen der Struktur eines Materials und seinen Eigenschaften stellt einen wichtigen Baustein in der Entwicklung effizienter Materialen für Energieumwandlung und Ladungstransfer dar. Um diese zu verstehen sind besonders computergestützte Simulationen eine hervorragende Methode, da sie es ermöglichen ohne vorherige Synthese die Eigenschaften von Substanzen auf atomarer Ebene zu untersuchen. Je nach der Größenordnung des Systems, der Energien und der Zeitskalen der untersuchten Prozesse müssen jedoch verschiedene, sorgfältig ausgewählte Modelle zur Berechnung genutzt werden. In dieser Dissertation werden daher drei verschiedene Charakterisierungsmethoden für Anwendungen aus dem Bereich der Energieforschung vorgestellt.

In der ersten Studie wird nach dem bestmöglichen Arrangement eines Paares geladener Quantenpunkte gesucht um den schnellstmöglichen interatomaren Coulombischen Zerfallsprozess (ICD) nach Anregung mit Infrarotlicht zu ermöglichen. Im ICD Prozess löst einer der geladenen Quantenpunkte nach Anregung mit einem Laser die Emission eines Elektrons in einem benachbarten Quantenpunkt aus. Um elektronische Übergänge in Kontinuumszustände zu beschreiben bei denen Elektronenkorrelation eine tragende Rolle spielt wird die effektive Massennäherung und die sehr flexible multi configuration time-dependent Hartree(MCTDH) Methode genutzt. Dabei wird festgestellt, dass ein empfimdliches Gleichgewicht von Polarisation der Elektronenwolke in den Quantenpunkten sowie der Coulombabstoßung zwischen ihnen existiert - wovon letztere für den ICD Prozess verantwortlich ist. Dieses Gleichgewicht führt schließlich zu optimalen Abstandsverhältnissen für maximale ICD Raten in Abhängigkeit von den Größenverhältnisse der beiden Quantenpunkte.

In einem zweiten Projekt werden die Möglichkeiten und Grenzen eines Datenbank-Ansatzes für die Interpretation von Röntgen-Absorptionsspektren (XA) amorpher Substanzen untersucht. Der Ansatz beruht auf der Erkenntnis, dass das kollektive Anregungsspektrum sich als Summe der Beiträge aller einzelnen Anregungen jedes Atoms in seinem genauen Umfeld darstellen lässt. Indem eine Datenbank von Röntgen-Absorptionsspektren von Kohlenstoffatomen in verschiedenartigen Umgebungen katalogisiert und bis zu einem selbst gewählten Abstand zusammengefasst wird, können die häufigsten, sauerstoffhaltigen funktionellen Gruppen aus verschiedenen experimentellen Proben von Graphenoxid identifiziert werden. Die zugrunde liegende Datenbank wird aus Rechnungen zu zeitabhängiger Dichtefunktionaltheorie (TDDFT) für die lokale Anregung einzelner Atome in verschieden funktionalisierten Graphenoxid

Modellmolekülen erhalten. Die Ergebnisse zeigen, dass die nicht-lokalen Effekte, die bei solchen hochenergetischen Anregungen von Bedeutung sind, prinzipiell durch die Ausdehnung des Katalogisierungs-Radius wiederhergestellt werden können und die Datenbank-Methodik somit ein systematisches Werkzeug für die Identifizierung amorpher Substanzen darstellt.
Schließlich wird der erste Teilschritt der photochemischen Wasserspaltung an der Kante von Stickstoff-dotierten Graphenoxiden (NGO) untersucht. In diesem so genannten Protonen-gekoppelten Elektronentransfer (PCET) wird ein Elektron und ein Proton gleichzeitig vom Wasser an den NGO Katalysator abgegeben. Aus TDDFT Berechnungen zu mehreren Modellmolekülen kann zunächst bestimmt werden, welche strukturellen Merkmale zu einem effizienten Ladungstransfer führen. Wegen der nicht-adiabatischen Natur des gekoppelten Elektronen- und Protonentransfer Prozesses wird eine modifizierte zeitabhängige Konfigurations-Interaktions (TDCI) Rechenmethode entwickelt, welche die nicht-adabiatischen Kopplungsterme explizit im Propagator berücksichtigt. Besonders Strukturen mit konjugierten Ketogruppen in der Nähe des Protonen-akzeptierenden Stickstoffs zeigen hiernach besonders geeignete Eigenschaften für den Elektronentransfer. Weiterhin wird die Rate für den gesamten PCET Prozess maßgeblich vom Absorptionsprozess sowie dem anschließenden Austausch der Besetzung der elektronischen Zustände durch thermische Dissipation beeinflusst.

Contents

List of Figures

1 Introduction

Computer simulation techniques have become an irreplaceable tool in material design since they enable studying material properties before conducting costly synthesis and experiments. Especially in the fields of drug and catalyst design, many materials can be optimized *in silico* for a desired application with the assistance of theoretical calculations. However, depending on the system size and timescale of the processes under consideration, highly advanced calculation techniques need to be applied and large amounts of data need to be collected. In this thesis I therefore present three theoretical case studies and discuss how these can be used to broaden our understanding of the structure-property relationships of processes on different timescales and system sizes in energy material research.

1.1 Motivation

Ever since realizing our role as the earth's caretakers, it has become a central goal of society to ensure a symbiotic co-existence with the ecosystem that we depend on. This way, future generations will be able to enjoy a similar level of comfort as we live in today without facing the repercussions of drastic environmental changes. However, as ecologist G. Hardin pointed out in the late 1960s, this task is tied to challenges that reflect typical examples for the "tragedy of the commons" and thus have no final technological solution.[1] His reasoning is based on the limited resources of our planet that will always remain limited, even if the efficiency with which they are used or harvested was maximized technologically and that only a redefinition of what society *should* maximize can lead to the desired long-term stability. He continues that such a redefinition could, however, only be carried out on a political and sociological level by implementing world-wide regulations and agreeing on a new system of values. Eventually, after many similar realizations in the following years, the environmental debates culminated in several politically binding agreements like the Montreal protocol (1987)[2] or the United Nations Framework Convention on Climate Change (UNFCCC, 1992)[3] that defined goals for reducing damage to the environment with respect to climate change, protection of resources and biological species across national borders. While it still remains to be seen whether all of these political agreements will have the desired effect of propagating a symbiotic

lifestyle with our planet, it has become clear that we will only be able to afford a similar quality of life in the future by developing more efficient technologies in parallel to the political measures so that we can drastically reduce and eventually end our dependence on non-regenerative resources by energy research.

For this scientific contribution, there are two major routes from which to approach energy-related research. The first route focuses on finding new ways to efficiently harvest sustainable energy sources. For this task, especially solar energy has been identified as one of the most attractive sources due to the practically infinite amount of available energy. With a mean solar power input of 120 PW[4] hitting earth's atmosphere for $365 \times 24 = 8760$ hours a year, the corresponding energy amounts to 1051200 PWh. Comparing this number to humankind's global energy consumption of 160 PWh per year (2019)[5] one realizes that only 0.015 % of this amount would need to be harvested (i.e. solar power collection of 18.3 TW). Assuming further a somewhat realistic mean device collection efficiency of 10 % (which is roughly half of reported peak performances[6]) and that the mean solar power input is directly proportional to half the surface area of our planet being hit with light (i.e. 255.05 million square kilometers[7]), this translates to a required solar cell coverage of

$$\frac{160\,\mathrm{PWh}}{(\frac{120\,\mathrm{PW}}{255.05\,10^6\,\mathrm{km}^2}) \cdot 8760\,\mathrm{h} \cdot 10\%} = \frac{0.00015}{0.1} \cdot 255.05\,10^6\,\mathrm{km}^2 = 388203\,\mathrm{km}^2 \ ,$$

which is roughly eight times the area of Lake Michigan,[8] the total area of Japan[9] or 0.76 permille of the overall planet's surface. Although such a basic estimate ignores many factors like device lifetimes, transport losses, weather and such, it can give a general idea on the orders of magnitude for the challenges that solar energy research is facing. However, it also shows the great potential of the technology, since each additional percent in device efficiency translates to enormous reductions in the area that theoretically would need to be covered.

The two prominent routes for harvesting solar energy are photovoltaics and photochemistry. In photovoltaics, the sunlight is converted into electrical power by creating photocurrents in efficient charge-separation devices that use one or several different highly developed materials in conjunction.[10] This electricity can then either be injected directly into the electrical power grid or be stored in chemical batteries, capacitors, water-pumping reservoirs etc.[11] While the direct usage of photovoltaic electricity results in a highly efficient one-time energy conversion before consumption, the storage of photovoltaics-generated energy is comparably inefficient, since it requires at least three conversion steps with their own respective energy-losses.

Photochemistry on the other hand encompasses all processes where the charge separation caused by the initial photon absorption is used for chemical reac-

tions.[12] This way, photochemistry is used to directly store solar energy by converting a basic chemical into a fuel that can be burned for the generation of electricity or heat in a CO_2-neutral manner. Although this means that at least two conversion steps (i.e. storing and burning) are needed until the energy can be used, photochemistry also offers the possibility to fixate carbon dioxide like in an artificial photosynthesis - which would in principle enable a CO_2-neutral fuel generation route, not counting the initial device production.[13] Furthermore, since most engine architectures and power production plants have been optimized for over a century for the combustion of hydrocarbon fuels, a CO_2-neutral process to generate them would not necessitate the implementation of new power plants.

Both of these promising research fields, however, still suffer from relatively low efficiencies, short device lifetimes and requiring rare chemical elements or any combination thereof. To find solutions, top-down as well as bottom-up research routes are pursued, where one either starts from a long-lived and highly capable material and tries to replace the rare components[14] or from a rather inefficient, short-lived but inexpensive material whose efficiency is then optimized,[15] respectively.

The second route, besides finding more efficient routes for energy generation, is by improving how we use the energy. This means especially to discover and study new processes or mechanisms that can potentially replace less efficient ones. One of the arguably most significant paradigm shifts in the last decades to this effect can be found in the replacement of incandescent light bulbs with advanced lighting technologies like light-emitting diodes (LED). In incandescent light bulbs, the underlying process is based on using electric energy to heat up a wire until it emits blackbody radiation[16] in the visible regime. For the longest time this was the most economic and convenient process for generating artificial light and thus research was focused to better understand the energy-transfer and conversion processes to improve device efficiency. However, with the invention of light-emitting diodes a more efficient process of generating light from electric currents was found and was ever since improved again with respect to its own unique mechanism. Since lighting accounts for almost 19 % of the total electricity consumption worldwide,[17] a lowering of the energy consumption by about 40 % after switching to LED technology[18] shows how much impact a change in the underlying energy usage mechanism can have.

One research field from which many new and interesting mechanisms with potential use in energy research have emerged lately is nanoelectronics. In this field, one categorizes three different types of materials with respect to their spatial dimensions which expand for less than 100 nanometers: 2-dimensional quantum sheets, 1-dimensional quantum wires and 0-dimensional quantum dots.[19] The reason for the special properties of such materials is often rooted in the so-called quantum size effects,[19] which roughly translates to scenarios where the device becomes

smaller than the space in which the electrons can occupy their excited states. Especially in quantum dots, where all three spatial dimensions are restricted, the excited states become fully discrete like in atoms[20] and their energetic positioning can be tailored by controlling the size of the device. This high control over the electronic structure gives quantum dots a very high versatility and opens up the possibility for several applications[21] that may be more efficient than the previously applied ones.
Finally, at the core of both efficient energy generation and consumption lies researching the structure-property relations for the underlying energy-transfer processes. Generally speaking, energy transfer occurs whenever it is transported from one medium to another - including the possibility of being converted to a different form of energy in the process. A "medium" in this sense can be of macroscopic size, as well as atomic size. For example, a macroscopic medium may be given by photon energy being converted into separated charges in an *extended solid*, such as a photovoltaic solar cell.[10] An atomic medium on the other side could for example be given by a local exciton on one part of a *molecule* being transferred in a so-called Förster resonance energy transfer (FRET) to a different part of the molecule.[22] By adapting a calculation method with respect to the system under consideration, theoretical calculations allow to gain an understanding of such energy-transfer processes and to propose optimizations for the current state of the art.
Following a short introduction on the processes, the underlying calculation methods will be introduced in chapter 2. The results of my doctoral research are presented in a cumulative collection of articles in chapter A. Finally, I conclude the findings of this research project and give an outlook for future studies in chapter 3.

1.2 | Interatomic Coulombic Decay in Charged Quantum Dots

The first process that was selected for investigation is the Interatomic Coulombic Decay (ICD). In its initial formulation,[23] ICD occurs in clusters of molecules or atoms, where one of the monomers is being ionized by removing an inner-valence shell electron. Since the resulting electron configuration belongs to an excited state of the singly ionized monomer, the system strives to relax towards its energetic ground state by transferring one of the outer-valence shell electrons into the inner-valence shell vacancy. If the excited ion is alone in a vacuum, the surplus relaxation energy can only be released by a radiative emission mechanism, because the released energy is insufficient to eject an outer-shell electron into the vacuum (compare figure 1.1a)). This is different, for example, in the Auger decay[24] where the vacancy is situated in the core shell instead and relaxation energies lie far

above the second ionization potential. However, when the ionized monomer is part of a cluster, the relaxation energy may be sufficient to overcome the first ionization potential in a neighboring charge-neutral monomer (see figure 1.1 b)). If so, the energy can be transferred via so-called virtual photon exchange[22] to the neutral counterpart and an electron may be ejected from there. This ultimately results in two singly charged ions and an electron ejected at relatively low kinetic energy in contrast to highly energetic Auger electrons.

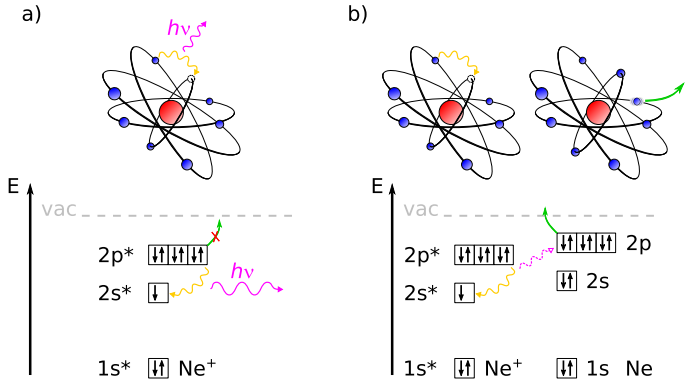

Figure 1.1: Comparison of inner-valence excitation in the monomeric Ne^+ cation (a) and the Ne^+-Ne dimer (b). Because the relaxation energy (yellow arrow) is insufficient to excite an electron from 2p* into the unbound vacuum levels, the only allowed decay mechanism in the monomer is de-excitation via photoradiation (purple arrow). In the dimer (b), the relaxation (yellow arrow) is followed by an energy transfer from Ne^+ to Ne via a virtual photon (dashed purple arrow) that is capable of initiating the ejection of an electron into the continuum (green arrow) with a kinetic energy depending on the remaining energy after the transfer.

Shortly after being predicted on a theoretical level,[23] the ICD process was verified experimentally in studies on weakly bound homogeneous noble gas dimers[25]–[27] by detecting the kinetic energy of two Ne^+ fragments in coincidence with the released slow electron. Since then, many more occurrences of ICD following inner-shell ionization have been found in other weakly bound systems, like hydroxide ions in water[28], [29] and hydrogen-bonded water dimers.[23], [30] Especially the latter study shows that ICD is in fact an ubiquitous and ultrafast process that could be closely connected to the cytotoxicity of ionizing radiation through the generation of slow electrons in the cell plasma.[30] Besides the homogeneous noble gas dimers, also asymmetric dimers and clusters have been studied to better understand the energy dependence and mechanism for ICD.[31]–[34] There, it was found that competing decay channels called electron-transfer-mediated decay (ETMD) can lower the ICD efficiency, if the energetics of the initial vacancy and the emitted electron differ too drastically, or if the atoms of the dimer get too close to each other. In this process, the vacancy in the ionized atom $\mathbf{A}^+$ is filled by an electron from the neighboring atom **B**, while also ejecting an electron from the same atom **B** leading to one doubly positively charged atom and one neutral one.

The ICD rate is closely related to the distance between the ionized monomer $\mathbf{A}^+$ and the emitter **B**. Therefore, at larger distances the process becomes less efficient. However, under specific conditions it is possible to increase the range of ICD, by inserting another atom **C** in-between $\mathbf{A}^+$ and **B** that itself may not decay via ICD with $\mathbf{A}^+$. If the energy levels in **C** are then suitable, an effect called superexchange ICD[35],[36] can be observed where the ICD proceeds via a lower-lying virtual state $\mathbf{A}^+\mathbf{-C}^-\mathbf{-B}^+$. This opens the possibility of triggering ICD in even more far apart moieties and effectively increase the number of overall possible neighbors.
Since it was found that the ICD efficiency drastically increases with the number of neighbors (i.e. number of possible decay channels),[37],[38] this finding presents yet another possibility of enhancing the likelihood and overall rate of the ICD process.
Finally, since the quantum confinement in quantum dots leads to a discretization of the energetic levels of excited states similar to atoms,[19] ICD was recently predicted to occur between charged quantum dots[39] in a similar way as for the aforementioned atomic dimers. However, due to the additional possibility to freely tune the electronic structure by changing the quantum dot sizes and their arrangement. This opens up the possibility to design an ICD-based device that generates an electric current, which means releasing an electron into a conduction band, analogous to the vacuum level of fig. 1.1.[39] Since this is a promising new route for ultrafast excitation-to-signal conversion I study the underlying structure-property relationships for the efficiency of such theoretical devices (section A.1 of this dissertation). In the related research project, I discuss the interdependence of the ICD rate with respect to changes in the geometry of a paired quantum dot system. The simulation model and calculation methods used in this study are described in detail in sections 2.2.3 and 2.3.1.

1.3 | Water-Splitting in Nitrogen-doped Graphene Oxides

The second research topic addressed in this dissertation is aimed at studying the water-splitting reaction driven by nitrogen-doped graphene oxides (NGO) and finding a method to characterize the responsible active sites in an example study on its parent material graphene oxide (GO). Graphene oxide is an oxidized derivative of graphene and similarly forms single layered sheets of nearly atomic thickness. Different from graphene, which is a perfect zero band gap 2-dimensional crystal,[40] GO is a proper semi-conducting material with a band-gap that is dependent on its defect concentration, degree of oxidation and particle size.[41],[42] All of these can be controlled by changing the reaction conditions during production and work-up, which is typically derived from the original Hum-

mers' method.[43] In this method, bulk graphite is first treated with sulfuric acid that intercalates between single layers of graphite.[44] In a second step, a strong oxidant is used to oxidize the graphite layers which ultimately results in the exfoliation of graphene oxide sheets (see schematic figure 1.2). However, due to harsh reaction conditions graphene oxides are a non-stoichiometric compound whose sheets typically show a large number of defects especially in places where oxidation leads to CO_2 generation.[45] These holes in the carbon network are also the still-standing obstacle for the large-scale preparation of pristine graphene from reduced graphene oxides.[46]

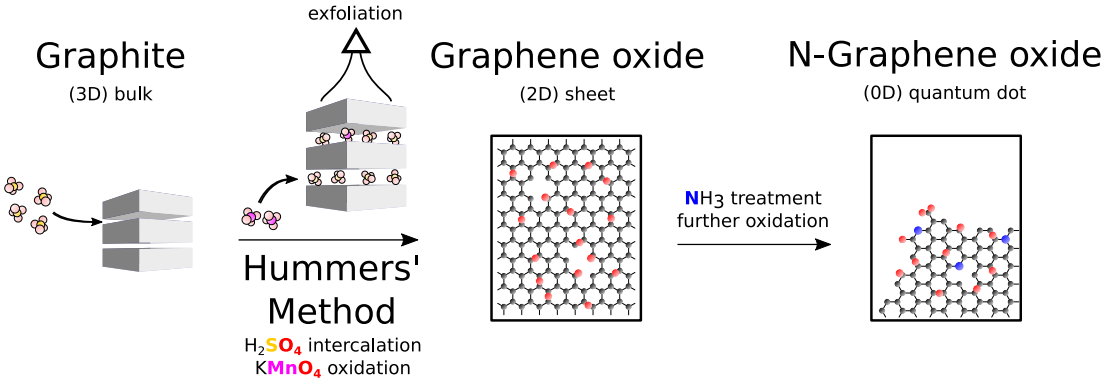

Figure 1.2: Schematic Scheme for preparation of NGO quantum dots.

Besides being a promising precursor material for the production of graphene, the band gap in highly oxidized GO can be tailored such that it may act as a photocatalyst for water splitting under irradiation with a mercury lamp emitting a mixture of UV and visible light.[41] Since the material consists of only earth-abundant materials such as carbon, oxygen and hydrogen, this in general presents a route for an environmentally friendly photocatalysis. Unfortunately, the material is sensitive to photocorrosion in which the functional groups on graphene oxides are steadily reduced to yield graphitic defect sites that are ultimately oxidized again until they eventually escape in the form of CO_2.[47] Therefore, over long irradiation times the material can be expected to completely lose its capability for driving the photocatalysis when no additional sacrificial reagent is used.

One chemical modification that increases both the photoreactivity as well as lifetime of GO is by doping the material with nitrogen.[42] In this process, the graphene oxide is treated with ammonia (NH_3, see figure 1.2) to incorporate the nitrogen atoms into the structure. Without being less environmentally friendly, the resulting NGO can produce considerable amounts of hydrogen and oxygen in an approximate 2:1 ratio,[42] which indirectly proves its photostability, since no side reactions or products seem to occur. The reason for the superior material capabilities are assumed to lie within the coupling of *n*- and *p*-type domains in the same molecule, like in a redox electrochemical cell. The domains are

junctioned by conducting, unfunctionalized areas of pristine graphene.[42] The n-type reaction domain carries more nitrogen atoms and is thus more likely to oxidize the water oxygen (electron accepting), while the p-type domain contains more oxygen functional groups, is more electron rich and therefore readily reduces protons (hole accepting). Since the parent material graphene oxide indeed shows recurrent islands of unfunctionalized carbon atoms in high-resolution transmission electron microscopy (TEM) images,[48] these could serve as such local active sites and explain the mechanism of the water-splitting reaction on NGOs.

To therefore characterize local active sites in a generally randomized structure, the first study of this project is dedicated to establishing a method that can find recurrent structural patterns from spectroscopic measurements. This method is based on comparing experimental spectra with a database of locally sensitive theoretical spectra to predict the most likely configurations that would give rise to the observed data. The suitable type of spectroscopy with such a sensitivity to atomic configurations is X-ray absorption spectroscopy. Here, the core-shell electrons of a specific chemical element may be excited into empty bound orbitals that can in principle extend over the whole material. Since the excited electron is, however, spatially localized at one single atom in the initial state, each atom gives a unique fingerprint that directly carries the information of the complete surrounding of the respective atom. In an experimental spectrum, all of these fingerprints are collected at the same time, and the resulting sum of fingerprints usually does not allow for reconstructing detailed structural information. In theoretical calculations, however, it is possible to simulate the fingerprint of each atom individually and thus deconstruct the experimental spectrum in terms of local patterns. Therefore, in section A.2 of this dissertation I present the capabilities of such a theoretical database deconstruction method and discuss its limitations and possible applications. The details of the underlying calculation techniques can be found in section 2.2.1 of this work and the database reconstruction of total X-ray absorption spectra is explained in section 2.3.2.

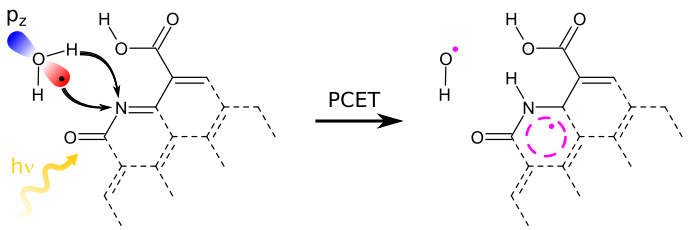

Figure 1.3: Proposed proton-coupled electron transfer (PCET) at the edge of nitrogen-doped graphene oxides (NGO). Following the photoexcitation (yellow arrow) an electron from water is transferred from the local p_z orbital (schematic orbital in red and blue) to the catalyst, while simultaneously a proton is transferred towards the nitrogen atom. The resulting product is a hydroxyl radical and an NGO+H radical complex.

Parallel to establishing a characterization method for local active sites in experimental samples, the second study focuses on identifying the key features of an optimized active site for the first part reaction of the photocatalytic water-splitting reaction in NGO model systems. This so-called proton-coupled electron transfer (PCET)[49] in which both an electron as well as a proton are transferred from water onto the catalyst (see figure 1.3), typically requires a coupled description of both the electron-transfer dynamics as well as the structural changes during proton transfer. In section A.4, I first conduct a general optimization of the electron-transfer properties of NGO model catalysts by altering the structure of a local active site. This optimization is followed by electron dynamics calculations in an explicitly coupled framework with the proton transfer to estimate the overall PCET rates. The model optimization follows the calculation methods described in section 2.2.1 and the electron dynamics are simulated as explained in section 2.2.2.

2 | Theoretical Background

In the following sections, the underlying theoretical background of the applied calculation methods will be explained. The chapter is divided in three major sections: Firstly, the general characteristics of quantum mechanics based on solving the time-independent Schrödinger equation are introduced in section 2.1. From a different point of view, the second section 2.2 then explains the time-dependent quantum dynamics and highlights similarities and challenges in different approaches for solving the time-dependent Schrödinger equation. Finally, section 2.3 gives a detailed description of the model systems applied throughout this work.

If not stated otherwise, atomic units were used in all equations to shorten the notation and improve readability. This means that the electron mass m_e, the elementary charge e, the reduced Planck constant $\hbar$ and the Coulomb constant $4\pi\epsilon_0$ are set to unity. Further, wavefunctions, matrix elements and integrals shall be abbreviated using the Dirac *bra-ket* notation.[50] Notethat if a specific function representation of the wavefunction is used outside an integral, the *bra* or *ket* is dropped according to

$$\Psi(\mathbf{r}) = \left\langle \mathbf{r} \,\middle|\, \Psi \right\rangle = \int \mathbf{r}\, \Psi \, d\mathbf{r} \ . \tag{2.1}$$

2.1 | Foundations of Quantum Mechanics

The concept of quantum mechanics was introduced in the early 20th century, following several peculiar experimental observations like the spectral density of black body radiation[51] or the wave-particle-dualism in the photoelectric effect[52] that were not explicable within the picture of physics of that time. Generally, quantum mechanics focuses on describing the behaviour of matter and its response under external stimuli on an atomic scale. Although the descriptions usually rely on probabilities and expectation values that strongly disagree with a deterministic picture of physics, many of the concepts can be identified as direct generalizations of macroscopic analogues. To highlight this rigorous (and in the early stages highly disputed) paradigm shift between the mostly deterministic picture of physics that had evolved for almost 300 years since Newton's "Principia",[53] a clear distinction between *classical* Newtonian mechanics and

non-classical quantum mechanics is made today.
Since most of the chemical properties relevant for this dissertation are a direct result of the behaviour of electrons, this first section shall cover the theoretical background necessary for their calculation. Later sections of the theory chapter then build up on these basic principles to smoothly introduce the more advanced concepts.
Finally, if not stated otherwise by additional citations, the explanations and concepts introduced in this section are a compilation from the books of Szabo and Ostlund (*"Modern Quantum Chemistry"*)[50] and Parr and Yang (*"Density Functional Theory of Atoms and Molecules"*).[54]

2.1.1 | The Many-Electron Problem

Time-Independent Schrödinger Equation

The main way to calculate the properties of a system of several electrons and nuclei is to numerically solve the Schrödinger equation

$$i\frac{\partial}{\partial t}\big|\,\Psi\big\rangle = \hat{H}\big|\Psi\big\rangle\ . \tag{2.2}$$

In this linear partial differential equation that is better known as the time-dependent Schrödinger equation (TDSE), $\frac{\partial}{\partial t}$ refers to a differentiation with respect to time t, $\hat{H}$ is the Hamilton operator (*Hamiltonian*) and $|\Psi\rangle$ the system wavefunction comprising all information about the electrons and nuclei at each time and point in space. The Hamiltonian

$$\begin{aligned}\hat{H} = & -\sum_{i=1}^{N}\frac{\nabla_i^2}{2} \quad -\sum_{A=1}^{M}\frac{\nabla_A^2}{2M_A} \quad -\sum_{i=1}^{N}\sum_{A=1}^{M}\frac{Z_A}{r_{iA}} \\ & +\sum_{i=1}^{N}\sum_{j>i}^{N}\frac{1}{r_{ij}} \quad +\sum_{A=1}^{M}\sum_{B>A}^{M}\frac{Z_A Z_B}{R_{AB}}\end{aligned} \tag{2.3}$$

includes the kinetic energies of all N electrons with coordinates $\vec{r}_i$ in the first term and all M nuclei with respect to their specific masses M_A and coordinates $\vec{R}_A$ in the second term. In these terms, $\nabla_i^2 = \frac{\partial^2}{\partial r_{xi}^2} + \frac{\partial^2}{\partial r_{yi}^2} + \frac{\partial^2}{\partial r_{yi}^2}$ is the Laplacian operator with respect to either the i^{th} electronic coordinate vector $\vec{r}_i$ or likewise the A^{th} nuclear coordinate vector $\vec{R}_A$, respectively. The attractive Coulomb potential between electrons and nuclei depending on their respective inter-particle distance $r_{iA} = |\vec{r}_i - \vec{R}_A|$ and the nuclear charge Z_A are found in the third term. The terms four and five introduce the repulsive Coulomb potentials between pairs of electrons and nuclei, respectively.
In cases where the Hamiltonian does not contain a time-dependent external potential $V(t)$, one may re-formulate the TDSE (2.2) to obtain the time-

independent Schrödinger equation (TISE). This can be achieved by separating $\Psi(\mathbf{r}, \mathbf{R}, t)$ into a product of a time-dependent function $\Theta(t) = e^{-iEt}$ and a time-independent, spatial function $\Psi(\mathbf{r}, \mathbf{R})$. Note that bold-font mathematical symbols indicate the use of a matrix:

$$\mathbf{r} = \begin{pmatrix} r_{x1} & r_{y1} & r_{z1} \\ r_{x2} & r_{y2} & r_{z2} \\ \vdots & \vdots & \vdots \\ r_{xN} & r_{yN} & r_{zN} \end{pmatrix} , \tag{2.4}$$

where the numbered indices count the N electrons, and row reflects the coordinates of this electron. Inserting the functions $\Theta(t) = e^{-iEt}$ and $\Psi(\mathbf{r}, \mathbf{R})$ into (2.2) and resolving the derivative then yields:

$$\begin{aligned} & i\frac{\partial}{\partial t}\, \Theta(t)\, \Psi(\mathbf{r}, \mathbf{R}) = \hat{H}(\mathbf{r}, \mathbf{R})\, \Theta(t)\, \Psi(\mathbf{r}, \mathbf{R}) \\ \Leftrightarrow \quad & i\frac{\partial}{\partial t}\, e^{-iEt}\, \Psi(\mathbf{r}, \mathbf{R}) = e^{-iEt}\, \hat{H}(\mathbf{r}, \mathbf{R})\, \Psi(\mathbf{r}, \mathbf{R}) \\ \Leftrightarrow \quad & e^{-iEt}\, E\, \Psi(\mathbf{r}, \mathbf{R}) = e^{-iEt}\, \hat{H}(\mathbf{r}, \mathbf{R})\, \Psi(\mathbf{r}, \mathbf{R}) \, . \end{aligned} \tag{2.5}$$

From the resulting equation (2.5), one finds that the left and right hand side are practically independent of e^{-iEt} and a new eigenvalue equation $\hat{H}|\Psi\rangle = E|\Psi\rangle$ can be written that features $\Psi(\mathbf{r}, \mathbf{R})$ as eigenvector and E as eigenvalue with respect to the Hamilton operator acting on $\Psi(\mathbf{r}, \mathbf{R})$. Since the eigenvalue E is the direct result of calculating the different energy terms from the Hamiltonian (2.3), E is also referred to as the (total) system energy of state $|\Psi\rangle$.

Electronic Wavefunction

To further reduce the problem of calculating the total system of all nuclei and electrons, the Born-Oppenheimer approximation is introduced. Since the nuclei are much heavier than the electrons, they can be approximately treated as stationary with respect to the electrons' movement. In other words, the approximation assumes that the electrons are fully (adiabatically) dependent on the nuclear motion and not dynamically coupled, since the electrons instantaneously adapt to any nuclear displacement. Consequently, the wavefunction is assumed to be separable, yielding:

$$\hat{H}(\mathbf{r}, \mathbf{R})\ \Psi_{nu}(\mathbf{R})\, \Psi_{el}(\mathbf{r}; \mathbf{R}) = (E_{nu} + E_{el} + E_{el,nu})\ \Psi_{nu}(\mathbf{R})\, \Psi_{el}(\mathbf{r}; \mathbf{R}) \, , \tag{2.6}$$

where the indices nu and el refer to the nuclear and electronic parts, respectively. The electronic wavefunction $|\Psi_{el}\rangle$ is then only parametrically dependent on the

nuclear coordinate matrix $\mathbf{R}$, as indicated by the semicolon. As a result of this separation, the total energy and Hamiltonian may also be rewritten into separate parts. These contain the terms that either carry only the coordinates of the nuclei and electrons (i.e. kinetic energies, electron-electron and nucleus-nucleus repulsions) or act on both coordinates (i.e. electron-nucleus attraction). When studying the behaviour of electrons in any system, the kinetic energies of the nuclei may therefore be neglected and the repulsion term needs to be calculated only once for a given atomic configuration. The remaining electronic TISE then reads:

$$\left(-\sum_{i=1}^{N} \frac{\nabla_i^2}{2} \; -\sum_{i=1}^{N}\sum_{A=1}^{M} \frac{Z_A}{r_{iA}} \; +\sum_{i=1}^{N}\sum_{j>i}^{N} \frac{1}{r_{ij}} \right) \Psi_{el}(\mathbf{r};\mathbf{R}) = E_{el} \; \Psi_{el}(\mathbf{r};\mathbf{R}) \; , \tag{2.7}$$

where the electronic Hamiltonian is contained in parentheses and E_{el} includes the energy for the repulsion between nuclei. For all further occurrences, the indices nu and el, as well as the parameter $\mathbf{R}$ will be dropped and only the electronic Hamiltonian and wavefunction are used, if not stated otherwise.

Finally, since electrons are fermions there are requirements that the wavefunction needs to fulfil. First of all, the antisymmetry condition has to be met, such that the sign of the wavefunction changes when switching the position of two electrons.

$$\Psi(\vec{r}_i, \vec{r}_j, \ldots, \vec{r}_N) = -\,\Psi(\vec{r}_j, \vec{r}_i, \ldots, \vec{r}_N) \tag{2.8}$$

Secondly, the wavefunction needs to follow the Pauli exclusion principle, which states that two electrons may never be equal in all four quantum numbers: the principal quantum number n, the angular quantum number l, the magnetic quantum number m and the spin quantum number s. The first three have a direct influence on the shape of the space that a single electron is likely to occupy and can thus be incorporated in the form of different spatial one-electron wavefunctions $\psi_i(\vec{r})$ that are required to be orthogonal to each other such that

$$\left\langle \psi_i(\vec{r}_1) \,\middle|\, \psi_j(\vec{r}_1) \right\rangle = \delta_{ij} = \begin{cases} 1 \;\; , \text{ if } i = j \\ 0 \;\; , \text{ else} \end{cases} \; , \tag{2.9}$$

where δ_{ij} is the so-called Kronecker Delta function. The spin quantum number is then introduced in the form of two spin wavefunctions $\alpha(\omega)$ or $\beta(\omega)$ that are multiplied to a spatial wavefunctions to yield the so-called spin-orbitals $|\chi_i\rangle$ and $|\overline{\chi}_i\rangle$, respectively. These depend on a combined spin and coordinate vector $\vec{x}_1 = (r_{1x}, r_{1y}, r_{1z}, \omega_1)$. Note that a convenient shorthand notation was applied here that uses a bar to distinguish two spin-orbitals which make use of the same spatial orbital but different spin wavefunctions according to:

$$\chi_i(\vec{x}) = \psi_i(\vec{r})\,\alpha(\omega) \quad \text{and} \quad \overline{\chi}_i(\vec{x}) = \psi_i(\vec{r})\,\beta(\omega)\ . \tag{2.10}$$

In all further occurrences, the different spins will be implicitly contained inside the indices i of the spin-orbitals, if not stated otherwise - thus allowing to replace all occurrences of $\vec{x}$ with $\vec{r}$. Further, the spin wavefunctions are required to be orthogonal to each other.
A functional form of the N-electron wavefunction $\Psi(\mathbf{r})$ that follows both the Pauli exclusion principle and antisymmetry condition can then be formulated as a so-called Slater determinant, that itself consists of one-electron spin-orbitals $\chi_i(\vec{r}_1)$ with a:

$$\Psi(\vec{r}_1, \vec{r}_2, \ldots, \vec{r}_N) \;=\; \frac{1}{\sqrt{N!}} \begin{vmatrix} \chi_i(\vec{r_1}) & \chi_j(\vec{r_1}) & \ldots & \chi_k(\vec{r_1}) \\ \chi_i(\vec{r_2}) & \chi_j(\vec{r_2}) & \ldots & \chi_k(\vec{r_2}) \\ \vdots & \vdots & & \vdots \\ \chi_i(\vec{r_N}) & \chi_j(\vec{r_N}) & \ldots & \chi_k(\vec{r_N}) \end{vmatrix} . \tag{2.11}$$

Note that each row contains the coordinate $\vec{r}$ of one of the N electrons, while each column marks one of the M spin-orbitals. The antisymmetry condition is met by the determinant structure, since switching of two electrons' coordinates would mean exchanging two rows of the determinant, leading to a sign change. Further, if two columns of a determinant would become the same, the value of the determinant becomes zero, thus also fulfilling the Pauli exclusion principle. The prefactor $\frac{1}{\sqrt{N!}}$ ensures normalization, such that $\langle\Psi|\Psi\rangle = 1$.

Hartree-Fock Equations

Given a normalized wavefunction Ψ, one can proceed to calculate the expectation values for the system's Hamiltonian by multiplication of the *bra* $\langle\Psi|$ from the left to equation (2.7) according to

$$\big\langle \Psi \,\big|\, \hat{H} \,\big|\, \Psi \big\rangle = \big\langle \Psi \,\big|\, E \,\big|\, \Psi \big\rangle = E \big\langle \Psi \,\big|\, \Psi \big\rangle = E\ . \tag{2.12}$$

Practically, while the form of the electronic Hamiltonian is in principle set for a specific arrangement of atoms, the best possible arrangement of electrons is not. However, through the variation principle it can be shown[50] that a numerical solution of the TISE with a trial wavefunction $|\tilde{\Phi}\rangle$ always yields an upper bound energy $\tilde{E}$ with respect to the exact electronic ground-state wavefunction $|\Phi_0\rangle$ and its energy E_0 (i.e. the energy of the system in its most relaxed state):

$$\tilde{E} = \big\langle \tilde{\Phi} \,\big|\, \hat{H} \,\big|\, \tilde{\Phi} \big\rangle \geq E_0 = \big\langle \Phi_0 \,\big|\, \hat{H} \,\big|\, \Phi_0 \big\rangle\ . \tag{2.13}$$

This way, the ground-state energy $\tilde{E}$ of a trial wavefunction is also a measure for the quality of the wavefunction itself. Using this finding in conjunction with the constraint of orthonormal spin-orbitals $\langle\chi_i|\chi_j\rangle = \delta_{ij}$, the problem of finding the ground-state N-electron wavefunction $|\Phi_0\rangle$ can be reformulated such, that instead one has to find the set of N orthonormal one-electron spin-orbitals $|\chi_i\rangle$ with minimum orbital energies ϵ_i. These energies can be obtained using the Hartree-Fock (HF) equations

$$\left(\hat{h}(\vec{r}_1) \; + \sum_{j\neq i} \hat{J}_j(\vec{r}_1) \; - \sum_{j\neq i} \hat{K}_j(\vec{r}_1)\right) \chi_i(\vec{r}_1) = \epsilon_i \, \chi_i(\vec{r}_1) \tag{2.14}$$

$$\hat{F} \, \chi_i(\vec{r}_1) = \epsilon_i \, \chi_i(\vec{r}_1) \; . \tag{2.15}$$

The so-called effective one-electron Fock operator $\hat{F}$ on the left hand side consists of a purely one-electron part $\hat{h}$ called the core Hamiltonian, whereas the Coulomb term $\hat{J}_j$ and exchange term $\hat{K}_j$ contain mean-field electron-electron interactions,

$$\hat{h}(\vec{r}_1) = -\frac{\nabla_1^2}{2} \; - \sum_{A=1}^{M} \frac{Z_A}{r_{1A}} \; , \tag{2.16}$$

$$\hat{J}_j(\vec{x}_1)\chi_i(\vec{x}_1) = \int d\vec{x}_2 \, \chi_j(\vec{x}_2)^* \; \frac{1}{r_{12}} \; \chi_j(\vec{x}_2) \; \chi_i(\vec{x}_1) \; , \tag{2.17}$$

$$\hat{K}_j(\vec{x}_1)\chi_i(\vec{x}_1) = \int d\vec{x}_2 \, \chi_j(\vec{x}_2)^* \; \frac{1}{r_{12}} \; \chi_i(\vec{x}_2) \; \chi_j(\vec{x}_1) \; . \tag{2.18}$$

From the two latter expressions, the exchange term $\hat{K}_j$ is a purely quantum mechanical contribution with no classical analogue. Furthermore, both $\hat{J}_j$ and $\hat{K}_j$ explicitly contain the j^{th} spin-orbital themselves. Hence, the one-electronic spin-orbitals $|\chi_i\rangle$ that are to be optimized during a calculation simultaneously form a median, self-consistent field (SCF) that acts on the system's electrons. Evaluation of the expectation values of all one-electron operators with respect to the spin-orbitals results in matrix elements of the form

$$F_{mn} = \left\langle \chi_m(\vec{x}_1) \,\middle|\, \hat{F}(\vec{x}_1) \,\middle|\, \chi_n(\vec{x}_1) \right\rangle \; . \tag{2.19}$$

Roothaan-Hall Equations

Based on this effective one-electron treatment, a numerical procedure can be formulated that minimizes the energy of the N-electron wavefunction $|\Psi\rangle$ by convenient matrix diagonalisation procedures. For restricted closed-shell systems this leads to the Roothaan-Hall equations or restricted Hartree-Fock (RHF) method. The restricted closed-shell case assumes that all spin-orbitals are doubly occu-

pied in the ground state and that the spin-orbitals $\chi_i(\vec{x}_1)$ and $\overline{\chi_i}(\vec{x}_1)$ make use of the same spatial wavefunctions $\psi_i(\vec{r}_i)$ according to eq. (2.10). This means, that the occupied N spin-orbitals can be replaced by $N/2$ one-electron spatial-orbitals $\psi_i(\vec{r}_1)$ that can be expanded into a basis of arbitrarily large, but finite size via linear combination of atom-centered orbitals (LCAO) $\phi_\mu(\vec{r}_1)$ according to

$$\psi_i(\vec{r}_1) = \sum_{\mu}^{K} C_{i\mu}\phi_\mu(\vec{r}_1) \ . \tag{2.20}$$

Note, that greek letter indices refer to the μ^{th} basis function, while the latin letter indices refer to the i^{th} spatial wavefunction. Also, the basis functions are not necessarily orthogonal but instead form a symmetric, quadratic $K \times K$ overlap matrix $\mathbf{S}$ with matrix elements $S_{\mu\nu} = \langle\phi_\mu|\phi_\nu\rangle$.
In the case of $N/2$ restricted closed-shell spin-orbitals, the Fock operator may be rewritten to yield

$$\hat{F}(\vec{r}_1) = \hat{h}(\vec{r}_1) + \sum_{j}^{N/2} 2\hat{J}_j(\vec{r}_1) - \hat{K}_j(\vec{r}_1) \ , \tag{2.21}$$

where the factor 2 in front of $\hat{J}_j$ is needed since the terms of $\hat{J}_j$ and $\hat{J}_{\bar{j}}$ constructed from the same and opposite spin (i.e. $\chi_j(\vec{r}_2)$ and $\overline{\chi}_j(\vec{r}_2)$, see equation (2.17)) would result in the same contribution regardless of the spin of electron 1. This is not the case for the exchange operator $\hat{K}_j$ that would become zero for anti-parallel spins of electron 1 and 2 (i.e. only one of the two $\hat{K}_j$ or $\hat{K}_{\bar{j}}$ would be non-zero).
Inserting the set of fixed basis functions with variable coefficients into the Hartree-Fock equation (2.14) then yields

$$\sum_{\mu}^{K} C_{i\mu}\hat{F}(\vec{r}_1)\ \phi_\mu(\vec{r}_1) \ = \ \epsilon_i \sum_{\mu}^{K} C_{i\mu}\ \phi_\mu(\vec{r}_1) \ . \tag{2.22}$$

Multiplication of this expression from the left by $\langle\phi_\nu(\vec{r}_1)|$ leads to the respective expectation value

$$\sum_{\mu}^{K} C_{i\mu}\big\langle \phi_\nu(\vec{r}_1) \,\big|\, \hat{F}(\vec{r}_1) \,\big|\, \phi_\mu(\vec{r}_1)\big\rangle = \epsilon_i \sum_{\mu}^{K} C_{i\mu}S_{\nu\mu} \ . \tag{2.23}$$

Finally, this can be conveniently expressed in the convenient matrix representation

$$\mathbf{FC} = \mathbf{SC}\boldsymbol{\epsilon}. \tag{2.24}$$

The energies of the one-electron wavefunctions $|\psi_i\rangle$ are then minimized by nu-

merical diagonalization of the energy matrix $\boldsymbol{\epsilon}$ for a trial wavefunction with an initial coefficient matrix $\mathbf{C}$. Note, that due to the size of the expansion, the diagonalisation of this expression yields the K energetically lowest spatial orbitals $\psi_i(\vec{r}_1)$ and thus returns both occupied as well as non-occupied spatial orbitals. The latter are also referred to as *virtual* orbitals.

2.1.2 | Electron Correlation and Excited States

Although HF theory is a systematic approach to calculate the properties of an N-electron wavefunction, the mean-field treatment of electron-electron interactions does not capture the electrons' *inter*dependent swarm-like nature, where a change in the behaviour of one of them has an instantaneous effect on the behaviour of all other electrons as well. This generalization leads to a missing energy with respect to the Hartree-Fock solution which is known as correlation energy E_c

$$E_0^{\mathrm{exact}} = E_0^{\mathrm{HF}} + E_\mathrm{c}. \tag{2.25}$$

Therefore, using the terminologies introduced in the previous section, two concepts of how to recover the correlation energy are briefly presented in this section. Since these concepts make direct use of the Hartree-Fock ground-state wavefunction as a reference, they are oftentimes referred to as Post-Hartree-Fock methods. The first of these concepts is referred to as configuration interaction (CI) theory. It is based on the idea, to systematically construct additional Slater determinants, so-called configurations, where electrons were promoted from the Hartree-Fock ground-state one-electron spin-orbitals into virtual spin-orbitals. This way, the N-electron wavefunction $|\Psi^{\mathrm{CI}}\rangle$ is expanded into a basis configurations according to

$$\big|\,\Psi^{\mathrm{CI}}\big\rangle = c_0\big|\,\Psi_0^{\mathrm{HF}}\big\rangle + \sum_{a,r} c_a^r\big|\,\Psi_a^r\big\rangle + \sum_{a,r}\sum_{b>a,s>r} c_{ab}^{rs}\big|\,\Psi_{ab}^{rs}\big\rangle + \ldots \quad . \tag{2.26}$$

This so-called CI expansion contains the ground-state reference Hartree-Fock wavefunction $|\Psi_0^{\mathrm{HF}}\rangle$ and excited configuration Slater determinants of the type $|\Psi_a^r\rangle$. Using the jargon of second quantization,[50] these configurations are constructed from the reference wavefunction by annihilating one electron in an occupied spin-orbital $|\chi_a\rangle$ while creating one electron in a virtual spin-orbital $|\chi_r\rangle$ instead. Similar to the basis set expansion of spin-orbitals introduced earlier, the basis of configurations is then kept fixed, while the coefficients c are optimized in a similar diagonalization procedure with respect to the N-electron wavefunction energies $\mathbf{E}$ as introduced in the Roothaan-Hall equations. While the configurations constructed from the reference wavefunction are not physically realistic "excited states", the eigenvectors belonging to higher energy eigenvalues of the

diagonalized matrix $\mathbf{E}$ are canonical N-electron excited-state wavefunctions $|\Psi_i\rangle$. The additional flexibility from mixing the Hartree-Fock ground state with higher excited configurations is able to recover the exact correlation energy in the limit of including all possible excitations (Full-CI limit) within the chosen basis set size (Hartree-Fock limit). Although the method thus returns an exact solution, the Full-CI limit is impracticably large for most systems of interest, because the space of possible excitations grows in faculties by the number of electrons and orbital space. In practice the CI-expansion is therefore truncated after a certain expansion length, giving rise to the CI-singles (CIS), -doubles method (CISD) and so forth. Take note that the CIS method does not improve on the ground-state energy because matrix elements of the form $\langle\Psi_0|\hat{H}|\Psi_a^r\rangle = 0$ when the effective one-electron Hamiltonian is constructed from the one-electron basis of $|\Psi_0\rangle$ (Brilloun's theorem).

The second relevant method for this dissertation is based on the multi-configuration self-consistent field method (MCSCF). In this also multi-determinantal method, only a specific and much smaller subset of excited determinants is constructed from the initial reference such that the wavefunction reads

$$\big|\,\Psi\big\rangle = c_0\big|\,\Psi_0^{\mathrm{HF}}\big\rangle + \sum_I c_I\big|\,\Psi_I\big\rangle \tag{2.27}$$

However, instead of choosing the basis set of determinants to be fixed, both the coefficients c_I for the Slater determinants as well as their respective spin-orbitals $|\chi_i^{(I)}\rangle = \sum_\mu c_{i\mu}^{(I)}|\phi_\mu\rangle$ are optimized simultaneously. This way, the number of necessary determinants can be greatly reduced, by adding more flexibility within a smaller set of determinants - with the cost of having a generally computationally more demanding task of optimizing both the basis set coefficients, as well as the configurations' coefficients.

Besides these two methods there are several more Post-Hartree-Fock methods that make use of the Hartree-Fock ground state as a reference. For example, the Møller-Plesset perturbation theory[55] is based on adding perturbation terms to the Hamiltonian and construct expressions for correlation-corrected wavefunctions and energies. Another method that shall briefly be mentioned in this regard is Coupled-Cluster theory.[56] It is similar to configuration interaction theory in that it aims at constructing a multi-determinantal wavefunction from the Hartree-Fock reference. However, instead of explicitly expanding the wavefunction, the Coupled Cluster method introduces the so-called cluster operator $e^{\hat{T}}$ that creates excited wavefunctions from the reference. Here the expansion length of $\hat{T}$ gives rise to CCSD, CCSDT and so forth levels of theory analogous to CI theory. The exponential operator is then expanded into a Taylor series that ultimately leads to a different formulation than CI theory.

2.1.3 | Density Functional Theory

At the end of this section covering the foundations of quantum mechanics, a brief introduction on density functional theory (DFT) shall be given, which was used for the purpose of finding the relaxed and partially constrained ground-state geometries for all molecular systems. Also, it serves as a starting point for the introduction of time-dependent density functional theory in the next section.

As explained earlier in the context of Hartree-Fock theory, the calculation of the properties of a wavefunction requires the evaluation of a large number of one- and two-electron integrals, that each need to account for the three spatial dimensions, respectively. In density functional theory, the goal is to express the N-electron wavefunction and all its properties by one object with three spatial dimensions altogether - the electron density

$$\rho(\vec{r}_1) = N \int \cdots \int \left|\Psi(\vec{x}_1, \vec{x}_2, \ldots, \vec{x}_N)\right|^2 d\omega_1 d\vec{x}_2 \ldots d\vec{x}_N \ . \tag{2.28}$$

The general foundation of density functional theory are the two Hohenberg-Kohn theorems.[57] The first one states, that all ground-state properties (i.e. wavefunction, potential and kinetic energy) of an N-electron system are uniquely defined by the ground-state electron density $\rho_0(\vec{r}_1)$. The proof of this theorem is a reduction to absurdity (*reductio ad absurdum*), where one assumes that there exist two wavefunctions $|\Psi\rangle$ and $|\Psi'\rangle$ that have the same density ρ while, however, differing slightly in their respective Hamiltonians $\hat{H}$ and $\hat{H}'$. Then, this would result in ground-state energies of the form

$$\begin{aligned} E_0 < \left\langle \Psi' \middle| \hat{H} \middle| \Psi' \right\rangle &= \left\langle \Psi' \middle| \hat{H}' \middle| \Psi' \right\rangle + \left\langle \Psi' \middle| \hat{H} - \hat{H}' \middle| \Psi' \right\rangle \\ &= E_0' + \int \rho_0(\vec{r}_1)[v(\vec{r}_1) - v'(\vec{r}_1)]d\vec{r}_1 \end{aligned} \tag{2.29}$$

$$\begin{aligned} \text{and} \quad E_0' < \left\langle \Psi \middle| \hat{H}' \middle| \Psi \right\rangle &= \left\langle \Psi \middle| \hat{H} \middle| \Psi \right\rangle + \left\langle \Psi \middle| \hat{H}' - \hat{H} \middle| \Psi \right\rangle \\ &= E_0 - \int \rho_0(\vec{r}_1)[v(\vec{r}_1) - v'(\vec{r}_1)]d\vec{r}_1 \ , \end{aligned} \tag{2.30}$$

where $v(\vec{r}_1)$ and $v'(\vec{r}_1)$ can be any kind of parametrically defined potential, like the attractive forces due to the nuclei. Ultimately, addition of eqs. (2.29) and (2.30) leads to the inequality $E_0 + E_0' < E_0' + E_0$ and thus an indirect proof that there must exist a direct one-to-one mapping between wavefunctions, densities and potential terms.

The second theorem proves the existence of a variational principle in terms of the density, similar as for wavefunctions. It uses the Lagrange-multiplier

approach applying the normalization of the density to the number of electrons as a constraint

$$\frac{\partial \mathcal{L}}{\partial \rho} = E[\rho] - \mu\Big(\int \rho(\vec{r}_1) d\vec{r}_1 - N \Big) = 0 \ , \tag{2.31}$$

where μ is called the chemical potential. To turn these concepts into a practicable computational method, the Kohn-Sham theorem is introduced. Here, one assumes an N-electron wavefunction $|\Psi_s\rangle$ of N non-interacting electrons given in the determinantal form

$$\big|\, \Psi_s \big\rangle = \frac{1}{\sqrt{N!}} \det[\phi_i^{\mathrm{KS}} \phi_j^{\mathrm{KS}} \dots \phi_N^{\mathrm{KS}}] \ . \tag{2.32}$$

where the one-electron wavefunctions $|\phi_i^{\mathrm{KS}}\rangle$ are referred to as spatial Kohn-Sham orbitals. Due to the non-interacting nature of $|\Psi_s\rangle$, they differ from the Hartree-Fock spin-orbitals introduced in section 2.1.1. It is then invoked that the ground-state density resulting from the orthonormal restricted Kohn-Sham orbitals,

$$\rho(\vec{r}) = \sum_i^N \left| \phi_i^{\mathrm{KS}}(\vec{r}) \right|^2 \ , \tag{2.33}$$

exactly reproduces the ground state of an interacting system, when they minimize the energy of a non-interacting reference system instead. The corresponding one-electron Kohn-Sham equation of this reference system reads

$$\Big[-\frac{\nabla_i^2}{2} - \sum_A \frac{Z_A}{r_{iA}} + \int \frac{\rho(\vec{r'})}{|r - r'|} d\vec{r'} + \hat{v}_{\mathrm{xc}}(\vec{r}_i) \Big] \phi_i^{\mathrm{KS}} = \epsilon_i^{\mathrm{KS}} \phi_i^{\mathrm{KS}} \ , \tag{2.34}$$

where the resulting N-electron energy is a density functional of the form:

$$E[\rho] = T_s[\rho] + J[\rho] + E_{xc}[\rho] + \int v(\vec{r}_1)\rho(\vec{r}_1) d\vec{r}_1 \ . \tag{2.35}$$

In this functional, $T_s[\rho]$ and $J[\rho]$ are the kinetic energy in the non-interacting picture and the classical Coulomb interaction between two densities ρ, respectively. The energy with respect to the electron-nucleus attraction is in included in the integral with the external potential $v(\vec{r}_1)$.

To both incorporate the non-classical nature (i.e. exchange, see section 2.1.1) into J as well as correct for the non-interacting behaviour of T_s, the exchange-correlation functional E_{xc} is introduced as a correction term. Since no analytical form for this functional has been found, however, the corresponding potential $v_{xc}(\vec{r}_i) = \frac{\partial E_{xc}[\rho]}{\partial \rho}$ needs to be implemented as an approximate expression. Depending on the level of intricacy of the approximations for E_{xc}, a hierarchy of increasing accuracy (and required computational effort) can be defined. In this work, however, only the most general concepts within this hierarchy (that is

sometimes referred to as *Jacob's ladder* of DFT) shall be introduced briefly.
At the lowest level of this hierarchy stands the local density approximation (LDA), where the electron density is assumed to behave as an uniform electron gas (i.e. *jellium*) in an overall charge-neutral environment. At this level of theory, the exchange-correlation functional $E_{xc}[\rho]$ is determined only locally in the general form:

$$E_{xc}^{\mathrm{LDA}}[\rho] = E_{x}^{\mathrm{LDA}}[\rho] + E_{c}^{\mathrm{LDA}}[\rho] = \int \epsilon_x(\rho)\rho(\vec{r})d\vec{r} + \int \epsilon_c(\rho)\rho(\vec{r})d\vec{r}\,, \tag{2.36}$$

where ϵ_x and ϵ_c correspond to the individual exchange and correlation contributions per particle and volume, respectively. The general forms of these integrals can be derived from considerations within the jellium model and their parametrization was refined by quantum Monte-Carlo calculations.[54] Due to its origin from assuming an uncharged, extended system density, the LDA is a capable tool for the calculation of extended solids, but inapplicable to the molecular studies that were aimed for in this work.
At the second level of theory, the generalized gradient approximation (GGA) is invoked to treat non-uniform densities like in molecules, by inclusion of the first spatial derivative of $\nabla\rho$ within the expressions for ϵ_x and ϵ_c.[58] Further expanding this idea of derivatives then gives rise to the third level, the so-called meta-GGA functionals in which the functionals also depend on the second derivative of the density $\nabla^2\rho$ which is related to the electron's kinetic energy density.[59]
The fourth and last level discussed in here, especially is aimed at improving the description for the exchange energy. This is achieved by replacing a fraction α of the exchange functional $E_x[\rho]$ with the Hartree-Fock exchange energy K^{KS} with respect to eq. (2.18) using the Kohn-Sham orbitals.

$$E_{xc}^{\mathrm{Hybrid}} = E_c[\rho] + (1-\alpha)E_x[\rho] + \alpha K^{\mathrm{KS}} \tag{2.37}$$

These so-called hybrid functionals may additionally be connected to a range-dependence, where specific functionals are applied depending on the inter-particle distance. Moreover, the correlation term E_c may contain also different portions of LDA, GGA or meta-GGA parts. The reasoning behind the hybrid functionals is that DFT is highly performant for approximating correlation energies and short-range exchange terms, while HF theory gives the exact exchange energy contribution (at the same time lacking any correlation energy, however). Since the exchange density functional $E_x[\rho]$ becomes zero for zero density regions, especially non-local long-range interactions between one-electron wavefunctions are typically not well-described by DFT. Hybrid functionals are therefore essential for cases of non-overlapping, but interacting orbitals, like molecules in which long-range excitation channels (i.e. charge-transfer channels) play an important role for the electronic structure and electronic processes.

2.2 | Time-Dependent Quantum Dynamics

In the last section, calculation methods were introduced that are capable of calculating both electronic ground states as well as excited states with respect to a time-independent system Hamiltonian. From such states it is possible to estimate the rate Γ for a state-to-state transition according to Fermi's Golden Rule[60],[61] as

$$\Gamma_{if} = \frac{2\pi}{\hbar} \left| \left\langle \Psi_i \left| \hat{\vec{\mu}} \right| \Psi_f \right\rangle \right|^2 \rho(E) \ , \tag{2.38}$$

where usual SI units were used. In this expression, Ψ_i refers to the initial electronic state and Ψ_f to the final state. The states are connected via the dipole moment operator $\hat{\vec{\mu}}$ (see equation 2.65) and the expression is additionally dependent on the density of states at the energy E.

To practically drive such a state-to-state transition one would, however, need to apply for example a laser field $\vec{E}(t)$ that ultimately turns the time-independent Hamiltonian $\hat{H}_0$ into a time-dependent one. Following this change in the Hamiltonian, the states used in the above expression are in principle no longer eigenstates to $\hat{H}(t)$ - meaning that predictions with respect to Fermi's Golden Rule would no longer provide a good estimate. However, in cases where the changes in the Hamiltonian proceed on a slow timescale, the time-dependent wavefunction approximately stays stationary. This approximation is called *adiabatic approximation* and presents a useful tool for cases of weak field laser excitations in fully discrete states.[62]

In two of the research projects provided in this work, however, the changes in the Hamiltonian happen on very fast timescales or require the accurate description of time-dependent continuum states. Therefore, this second section of the theory chapter therefore aims at introducing a selection of time-depdendent quantum dynamics methods to solve the time-dependent Schrödinger equation (2.2) in an iterative manner according to a time-dependent variational principle. If not highlighted by further citations, the concepts and equations introduced in this section were compiled from the books of Parr and Yang (*"Density Functional Theory of Atoms and Molecules"*)[54] and Breuer and Petruccione (*"The Theory of Open Quantum Systems"*)[63] as well as Meyer, Gatti and Worth (*"Multidimensional Quantum Dynamics"*).[64]

2.2.1 | Time-Dependent Density Functional Theory

Runge-Gross Theorem

Owing to the high efficiency of density functional theory for calculating a ground state with approximate correlation correction, a similar approach is introduced for the solution of the time-dependent Schrödinger equation. For such a

method, one needs to prove a unique one-to-one mapping of the one-electron time-dependent density according to

$$\rho(\vec{r}_1,t) = N \sum_{\sigma_1,\sigma_2,\ldots,\sigma_N} \int\cdots\int |\Psi(\vec{x}_1,\vec{x}_2,\ldots,\vec{x}_N,t)|^2 d\vec{r}_2\ldots d\vec{r}_N \ , \tag{2.39}$$

where the spins σ_i have been summed over to obtain the spinless formulation. The proof of existence for such a mapping can be given according to the Runge-Gross theorem of time-dependent density functional theory (TDDFT). It relies on a starting assumption that any arbitrary external potential $v_{ext}(\vec{r}_1,t)$ can be written as a Taylor-series expansion of the form:

$$v_{ext}(\vec{r}_1,t) = \sum_{k=0}^{\infty} \frac{1}{k!} v_{ext,k}(\vec{r}_1) t^k \ . \tag{2.40}$$

Example choices for time-dependent external potentials include excitation fields $\vec{E}(t)$ and the nuclei-electron Coulomb attraction. Given this series expansion, the theorem proceeds to show that systems with the same initial ground-state density $\rho(\vec{r}_1, t = 0)$ always lead to different time evolutions, if the external potentials differ by more than a purely time-dependent function (i.e. differ by more than a pure phase difference).[65] In other words, if one starts from the same density at $t = 0$, one needs to prove that there are always different outcomes at time t for different external potentials. The condition for the external potentials then read

$$v_{ext}(\vec{r}_1,t) \neq v'_{ext}(\vec{r}_1,t) + c(t) \ , \tag{2.41}$$

where $c(t)$ is the purely time-dependent function. The general proof for the different time-evolutions with respect to the different external potentials can be achieved in two steps. Firstly, it is shown that the current densities

$$j(\mathbf{r},t) = \left\langle \Psi(t) \,\middle|\, \hat{j}(\mathbf{r}) \,\middle|\, \Psi(t) \right\rangle \tag{2.42}$$

$$j'(\mathbf{r},t) = \left\langle \Psi'(t) \,\middle|\, \hat{j}(\mathbf{r}) \,\middle|\, \Psi'(t) \right\rangle \tag{2.43}$$

$$\text{with} \quad \hat{j}(\mathbf{r}) = \frac{1}{2i} \sum_{i=1}^{N} \Big[\nabla_i \delta(\mathbf{r}-\mathbf{r}_i) + \delta(\mathbf{r}-\mathbf{r}_i)\nabla_i \Big] \tag{2.44}$$

have to differ for the time-dependent evolution with respect to the different external potentials v_{ext} and v'_{ext}. Here, the primes to the wavefunction denote that the underlying Hamiltonian includes the primed external potential. In these expressions, $\hat{n} = \delta(\mathbf{r}-\mathbf{r}_i)$ is the density operator that picks out the value of the density at position r_i and is zero everywhere else.

Forming the equations of motion for the expectation values of $\hat{j}(\mathbf{r})$ then yields

$$\frac{\partial}{\partial t} j(\mathbf{r}_1, t) = -i\big\langle \Psi(t) \,\big|\, \big[\hat{j}(\mathbf{r}), \hat{H}(t)\big] \,\big|\, \Psi(t)\big\rangle \tag{2.45}$$

$$\text{and} \quad \frac{\partial}{\partial t} j'(\mathbf{r}_1, t) = -i\big\langle \Psi'(t) \,\big|\, \big[\hat{j}(\mathbf{r}), \hat{H}'(t)\big] \,\big|\, \Psi'(t)\big\rangle \ , \tag{2.46}$$

where the expression in squared brackets denotes the commutator $[\hat{A}, \hat{B}] = \hat{A}\hat{B} - \hat{B}\hat{A}$. Assuming that both systems start from the same initial state $|\Psi(t=0)\rangle$ and taking the difference between the equations of motion at time $t = 0$ yields:

$$\begin{aligned} \frac{\partial}{\partial t}\Big(j(\mathbf{r}, t) - j'(\mathbf{r}, t)\Big)\Big|_{t=0} &= -i\big\langle \Psi(t=0) \,\big|\, \big[\hat{j}(\mathbf{r}), (\hat{H}(t=0) - \hat{H}'(t=0)\big] \,\big|\, \Psi(t=0)\big\rangle \\ &= -\rho_0(\vec{r})\nabla\big[v_{ext}(\mathbf{r}, 0) - v'_{ext}(\mathbf{r}, 0)\big] \ , \end{aligned} \tag{2.47}$$

which proves the difference in external fields. For the second step of the proof,[65] it is necessary to inversely show that given a initial density $\rho(\vec{r}, t = 0)$, the time evolution of this density always results in a non-zero difference for two different current-densities $j(\mathbf{r}, t)$ and $j'(\mathbf{r}, t)$. To prove this, one needs to consider the continuity equation:

$$\frac{\partial \rho(\vec{r}, t)}{\partial t} = -\nabla j(\mathbf{r}, t) \tag{2.48}$$

and show that the $(k+2)^{\text{th}}$ time-derivative with respect to length k of the Taylor series expansion (2.40) is

$$\left(\frac{\partial}{\partial t}\right)^{k+2} [\rho(\vec{r}, t) - \rho'(\vec{r}, t)]\Big|_{t=0} \neq 0 \tag{2.49}$$

for any functional form of $v_{ext}(\vec{r}, t)$, so that the densities according to the different system Hamiltonians start to differ for any infinitesimal time difference. The proof to this second requirement shall, however, only be referenced here for the sake of brevity.[65]

Assuming that there exists a unique mapping between any time-dependent external potential v_{ext} and the time-dependent density this provides a basis for constructing a similar calculation scheme as for time-independent DFT. The corresponding time-dependent formulation of the Kohn-Sham equation (2.34) then reads

$$i\frac{\partial}{\partial t}\,\phi_j(\vec{r},t) = \Big[-\frac{\nabla^2}{2} + v_{ext}[\rho,\Psi_0](\vec{r},t) + \int \frac{\rho(\vec{r'},t)}{|r-r'|} + v_{xc}[\rho,\Psi_0,\Phi_0](\vec{r},t)\Big]\,\phi_j(\vec{r},t) \tag{2.50}$$

Note that the potential terms themselves depend on the ground-state wavefunction at all times both in terms of the interacting wavefunction $|\Psi_0\rangle$ as well as the non-interacting auxiliary wavefunction $|\Phi_0\rangle$ in case of the exchange-correlation functional. Further, they are all assumed to be locally time-dependent, since laser fields, atom positions as well as the exchange-correlation potential may change over time. The locality in time fulfils the Markov condition of a memoryless potential, in that it does not depend on earlier times. In practice, however, only the external potential terms are treated time-dependently, while the exchange-correlation functional is assumed to stay constant over time. This approximation is known as the adiabatic approximation of TDDFT.

Linear-Response Time-Dependent Density Functional Theory

There are two main ways to formulate a calculation scheme based on the time-dependent Kohn-Sham equations, namely the real-time time-dependent density functional theory (RT-TDDFT) as well as the linear-response time-dependent density functional theory (LR-TDDFT). For the purposes of this dissertation, only the linear-response formalism needs to be introduced.
LR-TDDFT considers the determination of the ground-state density's response with respect to small external stimuli like excitation fields of low intensity. The working equations can be derived from perturbation theory,[65] where a small time-dependent perturbation is added to an otherwise time-independent external field

$$v_{ext}(\vec{r},t) = v_{ext,0}(\vec{r}) + \delta v_{ext}(\vec{r},t) \tag{2.51}$$

and in which $\delta v_{ext}(\vec{r}, t \geq 0) = 0$. It is then assumed that the time-dependent density starting from a ground-state density $\rho_0(\vec{r})$ can be expressed as

$$\rho(\vec{r},t) = \rho_0(\vec{r}) + \rho_1(\vec{r},t) + \rho_2(\vec{r},t) + \dots\ , \tag{2.52}$$

where the indices in ρ are referred to as first, second, ... order of density response. In LR-TDDFT, this sum is truncated after the first term $\rho_1(\vec{r},t)$ which is calculated from the density-density response function $\chi(\vec{r}t,\vec{r'}t')$ and the small perturbation as

$$\chi(\vec{r}t, \vec{r}'t') = \frac{\delta(\rho(\vec{r}, t)}{\delta v_{ext}(\vec{r'}, t')} \tag{2.53}$$

$$\rho_1(\vec{r}, t) = \int_0^\infty dt' \int d\vec{r}' \chi(\vec{r}t, \vec{r}'t') \delta v_{ext}(\vec{r'}t') \ . \tag{2.54}$$

The response function may be Fourier transformed with respect to $t - t'$ to yield the convenient spectral decomposition with respect to excitation energy ω (also known as Lehmann representation):

$$\chi(\vec{r}, \vec{r'}, \omega) = \sum_I \Big[\frac{\langle \Psi_0 \,|\, \hat{n}(\vec{r}) \,|\, \Psi_I \rangle \langle \Psi_I \,|\, \hat{n}(\vec{r'}) \,|\, \Psi_0 \rangle}{\omega - \Omega_I + i0^+} - \frac{\langle \Psi_0 \,|\, \hat{n}(\vec{r'}) \,|\, \Psi_I \rangle \langle \Psi_I \,|\, \hat{n}(\vec{r}) \,|\, \Psi_0 \rangle}{\omega + \Omega_I + i0^+} \Big] , \tag{2.55}$$

where the sum runs over I electronically excited-states with respective excitation energies $\Omega_I = E_I - E_0$. When interpreting the response functional closely, one notices that it becomes undefined whenever ω is exactly identical to an excitation energy. This special property of the response function may then be utilised in the formulation of an efficient search formalism that finds the excitation energies and states. Also, note that this resulting equation is formally time-independent.

Casida Equations and Tamm-Dancoff Approximation

The efficient calculation scheme behind LR-TDDFT is based on a matrix diagonalisation formalism that utilizes the so-called Casida equations.[66] Since the derivation of these equations[67] is interesting rather from a mathematical than from a quantum chemical point of view, only the working equations shall be provided in this dissertation. The Casida equations read:

$$\begin{bmatrix} \mathbf{A} & \mathbf{B} \\ \mathbf{B}^* & \mathbf{A}^* \end{bmatrix} \begin{pmatrix} \mathbf{X} \\ \mathbf{Y} \end{pmatrix} = \omega \begin{bmatrix} 1 & 0 \\ 0 & -1 \end{bmatrix} \begin{pmatrix} \mathbf{X} \\ \mathbf{Y} \end{pmatrix} \quad , \tag{2.56}$$

with the matrix elements of the submatrices $\mathbf{A}$ and $\mathbf{B}$ according to

$$A_{ia,jb} = \delta_{ij}\delta_{ab}(\epsilon_a - \epsilon_i) + K_{ia,jb} \tag{2.57}$$

$$\text{and} \quad B_{ia,jb} = K_{ia,jb} \tag{2.58}$$

and the coupling matrix $\mathbf{K}$ given as

$$K_{pq,rs} = \langle \phi_p^{\mathrm{KS}}(\vec{r}_1)\phi_s^{\mathrm{KS}}(\vec{r}_2) \,\big|\, \frac{1}{r_{12}} + v_{xc}(\vec{r}_1, \vec{r}_2, \omega) \,\big|\, \phi_q^{\mathrm{KS}}(\vec{r}_1)\phi_r^{\mathrm{KS}}(\vec{r}_2) \rangle \ . \tag{2.59}$$

The matrices $\mathbf{X}$ and $\mathbf{Y}$ are reflecting the excitation and de-excitation conditions following

$$X_{ia,\sigma}(\omega) = -\Big(\sum_{\sigma'} \sum_{jk} \frac{f_{j\sigma} - f_{k\sigma}}{\omega - (\epsilon_j - \epsilon_k)} \langle \phi_{i\sigma}^{\mathrm{KS}}(\vec{r})\phi_{k\sigma'}^{\mathrm{KS}}(\vec{r}') \,\big|\, \frac{1}{r_{12}} + v_{xc}(\vec{r}, \vec{r}', \omega) \,\big|\, \phi_{a\sigma}^{\mathrm{KS}}(\vec{r})\phi_{j\sigma'}^{\mathrm{KS}}(\vec{r}') \rangle \Big) \times \frac{1}{\omega - (\epsilon_i - \epsilon_a)} \tag{2.60}$$

$$\text{and} \quad Y_{ia,\sigma}(\omega) = -X_{ai,\sigma}(\omega) \ . \tag{2.61}$$

If the coupling matrix $\mathbf{K}$ is assumed to be zero for all matrix elements (Tamm-Dancoff approximation), the eigenvalue problem may be further reduced to yield the secular equation

$$\mathbf{AX} = \mathbf{\Omega X} \tag{2.62}$$

where the final goal is now to obtain a diagonal matrix of energies $\mathbf{\Omega}$. The eigenvectors $\mathbf{X}$ then can practically be turned into the compositions of the excited-states from Kohn-Sham orbitals $|\phi^{\mathrm{KS}}\rangle$ with respect to the ground-state density. The Tamm-Dancoff approximation was used throughout all TDDFT calculations of electronically excited states.

2.2.2 | Time-Dependent Configuration Interaction in Reduced Density Matrix Formulation

Time-Dependent Configuration Interaction

One of the methods that was used to calculate the dynamic time evolution of the electrons is based on solving the time-dependent Schrödinger equation using an N-electron wavefunction of the type:

$$\Psi^{\mathrm{TDCI}}(\mathbf{r}, t) \ = \ \sum_{i=0} D_i(t)\Psi_i^{\mathrm{CI}}(\mathbf{r}) \ . \tag{2.63}$$

In this time-dependent configuration interaction (TDCI) wavefunction,[68] the time-dependence of the CI wavefunction is contained in the expansion coefficients $D_i(t)$ of stationary configuration-state functions (CSF) from CI states $\Psi_i^{\mathrm{CI}}(\mathbf{r})$ which form the ground- and excited-state wavefunctions obtained from CI calculations (see section 2.1.2). Depending on the level of the preceding CI calculation (i.e. CIS, CISD, CISDT, ...) the number of possible CSFs and thus the flexibility

of the TDCI wavefunction increases, eventually including the correlation effects up to the Full-CI limit.
The TDCI method is capable of correctly describing the response of molecular systems and single- as well as multi-photon state-to-state transitions with respect to weak laser fields.[69],[70] The propagation of such a wavefunciton is carried out applying a unitary time-evolution propagator as

$$\begin{aligned} \Psi^{\mathrm{TDCI}}(\mathbf{r},t) &= \hat{U}(t,t_0,\mathbf{r})\ \Psi^{\mathrm{TDCI}}(\mathbf{r},t_0) \\ &= e^{-i(t-t_0)\hat{H}(\mathbf{r},t)}\ \Psi^{\mathrm{TDCI}}(\mathbf{r},t_0)\ . \end{aligned} \tag{2.64}$$

The time-dependent Hamiltonian of this expression in turn is given as the sum of the time-independent electronic Hamiltonian $\hat{H}(\mathbf{r})$ (see equation (2.7)) and an interaction term of the electrons and nuclei for the external field

$$\begin{aligned} \hat{H}(\mathbf{r},t) = \hat{H}_{el}(\mathbf{r}) &+ \hat{\vec{\mu}}\vec{E}(t) \\ = \hat{H}_{el}(\mathbf{r}) &+ \Big(-\sum_{i}^{N}\vec{r}_i + \sum_{A}^{M} Z_A\vec{R}_A\Big)\vec{E}(t)\ . \end{aligned} \tag{2.65}$$

Note that the dipole approximation[71] was applied here and that the positions of the nuclei $\vec{R}_A$ are kept fixed during propagation. The external fields used in this work has the form:

$$\vec{E}(t) = A_0\vec{\varepsilon}\cos(\omega_{0a}t)\ \sin^2\left(\frac{\pi t}{t_s}\right)\Theta(t_s) \tag{2.66}$$

where A_0 is the peak amplitude, $\vec{\varepsilon}$ the unitvector in the direction of the field and ω the excitation frequency (also called carrier frequency). Finally, the product of the Heaviside step function $\Theta(t_s)$ and $\sin^2(\frac{\pi t}{t_s})$ turn the field shape into a single pulse of length t_s that terminates the influence of the external field beyond the time t_s.
When the frequency of the external field matches the energy difference between the ground state and the a^{th} excited state, i.e. $\omega_{0a} = (E_a - E_0)$, a population inversion occurs between these states. This is achieved when the external field parameters A_0 and t_s are chosen in accordance to the so-called π-pulse condition for $\sin^2$-shaped pulses,

$$A_0\frac{t_s}{2} = \frac{\pi}{|\vec{\mu}_{0a}|}\ , \tag{2.67}$$

which is a result of the rotating wave approximation (RWA)[61] in the limit of weak external fields. Here, $\vec{\mu}_{0a}$ is the transition dipole moment from the ground state to the excited state with respect to the laser direction $\vec{\varepsilon}$

$$\vec{\mu}_{0a} = \left\langle \Psi_0^{\mathrm{CI}} \,\middle|\, \hat{\mu} \,\middle|\, \Psi_a^{\mathrm{CI}} \right\rangle\ . \tag{2.68}$$

Finally, it shall be noted that dipole-induced transitions with respect to weak laser fields are mostly one-electron processes. Therefore, CIS is in principle sufficient for describing the general time-dependent response of molecules with respect to weak fields.

Liouville-von Neumann Equation for Closed Quantum Systems

To arrive at the working equations used in the reduced density matrix (RDM)[63] representation of the TDCI-scheme (referred to as ρ-TDCI),[72] the concept of density operators and their time evolution is provided in this section. Note that in the following formulations of the density operator, the notation $|\Psi(t)\rangle\langle\Psi(t)|$ will be used to highlight its operating principle as a projection operator, although it technically is a functional representation with respect to expression (2.1). Density operators are useful constructs to treat scenarios where a single quantum system is insufficient to describe the behaviour of a system. In the state-representation the density operator of a mixed state $\Phi(t)$ is then written as

$$\hat{\rho}(t) = \sum_i p_i(t) \left| \Phi_i(t) \right\rangle \left\langle \Phi_i(t) \right| , \tag{2.69}$$

where $p_i(t)$ is the probability for the mixture of states being in the pure state $\Phi_i(t)$ at time t. Note that the symbol Φ is used instead of Ψ to signify that the states $\Phi_i(t)$ are not necessarily orthogonal with respect to each other, but fulfil the closure relation with $\sum_i p_i = 1$. This constitutes a normalization in the sense that across all possible mixtures of states, the system always is in a certain combination. By using an orthonormal set of time-independent CSFs $|\Psi_j\rangle$, the density operator may be brought into a Hermitian matrix form with elements

$$\begin{aligned} \rho_{jk}(t) &= \left\langle \Psi_k \right| \hat{\rho}(t) \left| \Psi_j \right\rangle \\ &= \sum_i p_i(t) \left\langle \Psi_k \right| \left. \Phi_i(t) \right\rangle \left\langle \Phi_i(t) \right| \left. \Psi_j \right\rangle \\ &= \sum_i p_i(t) d_{k,i}(t) d^*_{j,i}(t) \ . \end{aligned} \tag{2.70}$$

The diagonal elements of this density matrix $\rho_{kk}(t)$ are then the real-positive probability for the mixed state $|\Phi(t)\rangle$ being in the configuration state $|\Psi_k\rangle$. The complex off-diagonal elements $\rho_{jk}(t)$ are the so-called interferences with respect to $|\Psi_k\rangle$ and $\langle\Psi_j|$.

To formulate the time evolution of the density operator, its equation of motion needs to be derived. Without choosing a specific representation, the density operator reads

$$\hat{\rho}(t) = \big|\,\Phi(t)\big\rangle\big\langle\Phi(t)\,\big| \;. \tag{2.71}$$

Taking the time derivative of this expression and minding the product rule leads to

$$\frac{\partial}{\partial t}\hat{\rho}(t) = \Big(\frac{\partial}{\partial t}\,\big|\,\Phi(t)\big\rangle\Big)\big\langle\Phi(t)\,\big| \;+\; \big|\,\Phi(t)\big\rangle\frac{\partial}{\partial t}\big\langle\Phi(t)\,\big| \,. \tag{2.72}$$

Multiplication of both sides with the imaginary unit i and identifying the time-dependent Schrödinger equation $i\frac{\partial}{\partial t}|\Phi(t)\rangle = \hat{H}|\Phi(t)\rangle$ within the expression, one can derive the Louville-von Neumann equation as:

$$\begin{aligned} i\frac{\partial}{\partial t}\hat{\rho}(t) &= \hat{H}\,\big|\Phi(t)\big\rangle\big\langle\Phi(t)\big| \;+\; \big|\Phi(t)\big\rangle i\frac{\partial}{\partial t}\big\langle\Phi(t)\big| \\ &= \hat{H}\,\big|\Phi(t)\big\rangle\big\langle\Phi(t)\big| \;-\; \big|\Phi(t)\big\rangle\big\langle\Phi(t)\big|\,\hat{H} \\ &= \big[\hat{H}, \hat{\rho}(t)\big] \;. \end{aligned} \tag{2.73}$$

Open-System Lindblad- and Reduced Density Matrix Formulation

One of the goals for studying the water-splitting related proton-coupled electron-transfer dynamics in the project presented in [A.4] is to investigate the qualitative coupling of electronic and vibrational states. To include such coupling into an electron dynamics framework, a formulation of the Liouville-von Neumann equation for open quantum systems is required. The resulting formulation then is capable to describe the effects of finite-temperature-induced electronic state transitions.

Open quantum systems are generally the conjunction of an electronic quantum system $\mathcal{S}$ with a respective Hilbert space $\mathcal{H}_\mathcal{S}$ and a bath system $\mathcal{B}$ with $\mathcal{H}_\mathcal{B}$.[63] The combined picture $\mathcal{S}+\mathcal{B}$ then forms a closed quantum space by itself, in which the combined state space is obtained from the tensor product of both subspaces according to

$$\mathcal{H}_{\mathcal{S}+\mathcal{B}} = \mathcal{H}_\mathcal{S} \otimes \mathcal{H}_\mathcal{B} \;, \tag{2.74}$$

where each of the spaces may be described by respective sets of orthonormal basis functions $|\varphi^\mathcal{S}\rangle$ and $|\varphi^\mathcal{B}\rangle$ such that the combined wavefunction takes the form:

$$|\Psi\rangle = \sum_{i,j} \alpha_{ij}\,\big|\varphi_i^\mathcal{S}\big\rangle \otimes \big|\varphi_j^\mathcal{B}\big\rangle \;. \tag{2.75}$$

The total Hamiltonian for describing the combined system then takes the form

$$\hat{H}(t) = \hat{H}_{\mathcal{S}} \otimes \mathbf{1}_{\mathcal{B}} + \mathbf{1}_{\mathcal{S}} \otimes \hat{H}_{\mathcal{B}} + \hat{H}_{\mathcal{SB}}(t) \tag{2.76}$$

where the tensor products with the identities $\mathbf{1}$ in the first two terms ensure that the Hamiltonians act only on the respective other Hilbert spaces such that $\hat{H}_{\mathcal{S}}$ works only $\mathcal{H}_{\mathcal{S}}$ and the other way around. The third term then gives the interaction between the system and bath quantum systems.
In the following, a formalism will be provided, such that the time evolution of the electronic quantum system can be approximated without explicit knowledge about the bath system. The foundation of this is the assumption that the density operator of the combined system at t_0 is separable according to

$$\begin{aligned}\hat{\rho}(t_0) &= \hat{\rho}_{\mathcal{S}}(t_0) \otimes \hat{\rho}_{\mathcal{B}}(t_0) \\ &= \sum_{ij} p_{ij}(t_0) \left|\varphi_i^{\mathcal{S}}\right\rangle\!\left\langle\varphi_i^{\mathcal{S}}\right| \otimes \left|\varphi_j^{\mathcal{B}}\right\rangle\!\left\langle\varphi_j^{\mathcal{B}}\right| ,\end{aligned} \tag{2.77}$$

where the density operator $\hat{\rho}_{\mathcal{S}}$ is referred to as the reduced density operator of the electronic quantum system. The reduced density operator can then be obtained by taking the partial trace with respect to the bath states which is defined as

$$tr_{\mathcal{B}}\big(\hat{\rho}(t_0)\big) = \sum_{ij} p_i j(t_0) \left|\varphi_i^{\mathcal{S}}\right\rangle\!\left\langle\varphi_i^{\mathcal{S}}\right| \left\langle\varphi_j^{\mathcal{B}} \,\middle|\, \varphi_j^{\mathcal{B}}\right\rangle = \hat{\rho}_{\mathcal{S}}(t_0) \ . \tag{2.78}$$

Returning to the Liouville-von Neumann equation (2.73) for the evolution of the density operator $\hat{\rho}(t)$, one can then apply a set of approximations to derive an analogous formulation that covers the time evolution of the reduced density operator for the electronic subsystem including an effective coupling to the bath subsystem (i.e. dissipation) $\hat{\hat{\mathcal{L}}}_D \hat{\rho}_{\mathcal{S}}(t)$ according to

$$i\frac{\partial}{\partial t}\hat{\rho}_{\mathcal{S}}(t) = \big[\hat{H}_{\mathcal{S}}(t), \hat{\rho}_{\mathcal{S}}(t)\big] + i\hat{\hat{\mathcal{L}}}_D \hat{\rho}_{\mathcal{S}}(t) \ . \tag{2.79}$$

The dissipative coupling then takes the form

$$\hat{\hat{\mathcal{L}}}_D \hat{\rho}_{\mathcal{S}}(t) = \sum_{mn} \frac{\Gamma_{mn}}{2} \Big(\big[\hat{C}_{mn}, \hat{\rho}_{\mathcal{S}}(t)\hat{C}_{mn}^{\dagger}\big] + \big[\hat{C}_{mn}\hat{\rho}_{\mathcal{S}}(t), \hat{C}_{mn}^{\dagger}\big] \Big) \ , \tag{2.80}$$

where the so-called Lindblad operators $\hat{C}_{mn} = |\varphi_n^{\mathcal{S}}\rangle\langle\varphi_m^{\mathcal{S}}|$ mediate population transfer between electronic states m and n with a rate Γ_{mn}.[72] In the following, the properties of this electron dynamics description shall be briefly concluded. The full derivation of this so-called Lindblad form of the Liouville-von Neumann equation (or just Lindblad equation) can be found in the book of Breuer and

Petruccione.[63]
Firstly, the method uses the Born approximation which assumes that the coupling between the electronic system and bath only works towards the electronic system, such that the bath density operator becomes time independent. This assumption is valid in the limit of much faster electronic processes compared to the bath.[73] Secondly, it is assumed that the reduced density operator follows Markovian dynamics in that its time evolution is local in time. This means that the time evolution proceeds memoryless such that its immediate evolution does not additionally depend on earlier or later times, but only on its current mixed state.[73] Finally, it is assumed that external fields acting on the coupled system only affect the electronic quantum system and cause no additional coupling between system and bath.
For the purpose of this project, the configuration-state functions that form the TDCI wavefunction (and density operator $\hat{\rho}$) were constructed from the ground- and excited states of linear-response TDDFT calculations. The pseudo-CI CSF Slater determinants of were constructed using the respective Kohn-Sham orbitals. By using LR-TDDFT to obtain the excited states, the resulting hybrid DFT/CI methodology benefits from the favourable scaling of LR-TDDFT for calculating excited states while providing the multi-determinant flexibility for the time evolution of the wavepacket. Further by working in the reduced density matrix formulation, it is possible to include the dissipation dynamics for simulating the thermalization dynamics in an open quantum system.

2.2.3 | Multiconfiguration Time-Dependent Hartree Method

MCTDH Wavefunction

The multiconfiguration time-dependent Hartree method (MCTDH) uses a p-particle wavefunction of the form

$$\begin{aligned}\Psi(q_1,\dots,q_f,t) &= \Psi(\vec{Q}_1,\dots,\vec{Q}_p,t)\\ &= \sum_{j_1=1}^{n_1}\cdots\sum_{j_p=1}^{n_p} A_{j_1\dots j_p}(t)\ \varphi_{j_1}^{(1)}(\vec{Q}_1,t)\dots\varphi_{j_p}^{(p)}(\vec{Q}_p,t) \qquad (2.81)\\ &= \sum_J A_J \left|\,\varphi_J\right\rangle\ , \qquad (2.82)\end{aligned}$$

where q are arbitrary coordinates in f degrees of freedom (DOF) that may in principle be collected inside vectors of the form $\vec{Q} = (q_1, q_2, \dots)$. Since $\vec{Q}$ may likewise only depend on one DOF, the vector arrows will be dropped in all further occurrences of $\vec{Q}$. The wavefunction can then be written as sums of Hartree products of so-called single-particle functions (SPF) $|\varphi_{j_\kappa}^{(p)}\rangle$. The indices j_κ then count the number of n_κ basis functions assigned for the κ^{th} particle and the

variable $A_{j_1,\ldots,j_p}$ gives the coefficient for a specific Hartree product. The complete composition of these $j_1, \ldots, j_p$, as well as the respective Hartree product may be conveniently collected in a joined index J.
Note that so far a universal "particle" wavefunction may be described - meaning that these particles are not necessarily fermions or bosons. The antisymmetry condition for fermions may be recovered by requiring antisymmetrization of $A_{j_1\ldots j_p}$ via

$$\hat{A}_{\kappa,\lambda}\ A_{j_1,\ldots,j_\kappa,\ldots,j_\lambda,\ldots j_p} = -A_{j_1,\ldots,j_\lambda,\ldots,j_\kappa,\ldots j_p} \tag{2.83}$$

and further requiring that the sets $|\varphi^{(\kappa)}\rangle$ are the same for all κ to ensure indistinguishability of the coordinate systems. Without loss of generality, these conditions will be assumed to be met in the further course of this section.
The remarkable feature of the MCTDH wavefunction is that both the configuration coefficients A_J as well as the single-particle functions $|\varphi_J\rangle$ are time-dependent. This way, a highly flexible functional form is obtained that may describe the behaviour of particles efficiently with only few basis functions, which is especially important for describing continuum states. This flexibility comes at the cost of being computationally very expensive in comparison to, for example, the TDCI method.
Since both the coefficients A_J as well as the basis $|\varphi_J\rangle$ are flexible, the wavefunction is not yet unique: One may always construct another wavefunction by scaling the coefficients and basis functions, respectively. To turn the wavefunction into a unique form, a constraint operator $\hat{g}^{(\mathcal{K})}$ is introduced in the following equations of motion.

Equations of Motion and Uniqueness

The general approach to obtain the equations of motion (i.e. 1^{st}-order time derivatives) starts from the Dirac-Frenkel variational principle

$$\left\langle \delta\Psi \,\middle|\, \hat{H} - i\frac{\partial}{\partial t} \,\middle|\, \Psi \right\rangle = 0 \tag{2.84}$$

which translates to the minimum condition for the energy that a small change $\delta\Psi$ in the wavefunction $|\Psi\rangle$ does not cause a change in the system energy with respect to the time-dependent Schrödinger equation (2.2). This way, one obtains the first order differential equations for the time-dependent coefficients $\mathbf{A}$ according to

$$i\frac{\partial \mathbf{A}}{\partial t} = \boldsymbol{\mathcal{K}}\mathbf{A} \tag{2.85}$$

where $\mathbf{A}$ represents the antisymmetric configuration coefficient matrix $A_{JK} = -A_{KJ}$ and $\boldsymbol{\mathcal{K}}$ is the expectation value matrix

$$\mathcal{K}_{JL} = \left\langle \varphi_J \,\middle|\, \hat{H} \,\middle|\, \varphi_K \right\rangle \tag{2.86}$$

The equations of motion for the SPF matrix $\boldsymbol{\varphi}^{(\mathcal{K})}$ then read

$$i\frac{\partial \boldsymbol{\varphi}^{(\mathcal{K})}}{\partial t} = (1 - \hat{P}^{(\mathcal{K})})(\boldsymbol{\rho}^{(\mathcal{K})})^{-1}\boldsymbol{\mathcal{H}}^{(\mathcal{K})}\boldsymbol{\varphi}^{(\mathcal{K})} \tag{2.87}$$

where three new terms are introduced on the right hand side. The first one is a projection operator $\hat{P}^{(\mathcal{K})} = \sum_j |\varphi_j^{(\mathcal{K})}\rangle\langle\varphi_j^{(\mathcal{K})}|$ that ensures that all time changes of the SPFs cover new regions by invoking $(1 - \hat{P}^{(\mathcal{K})})$. The other entities are the mean-field operator matrix $\boldsymbol{\mathcal{H}}^{(\mathcal{K})}$ and the inverse density matrix $\boldsymbol{\rho}^{(\mathcal{K})}$. Both can be obtained straightforwardly from a closely related auxiliary basis set of so-called single-hole wavefunctions $|\Psi_a^{(\mathcal{K})}\rangle$

$$\left|\, \Psi \right\rangle = \sum_a \left|\, \varphi_a^{(\mathcal{K})} \right\rangle \left\langle \varphi_a^{(\mathcal{K})} \,\middle|\, \Psi \right\rangle = \sum_a \varphi_a^{(\mathcal{K})} \left|\, \Psi_a^{(\mathcal{K})} \right\rangle \tag{2.88}$$

where each of the single-hole functions is basically the whole N-particle wavefunction when excluding the SPF set of the $\mathcal{K}^{\text{th}}$ particle, e.g.

$$\left|\, \Psi_a^{(1)} \right\rangle = \sum_{j_2=1}^{n_1} \cdots \sum_{j_p=1}^{n_p} A_{a,j_2\ldots j_p} \left|\, \varphi_{j_2}^{(2)} \ldots \varphi_{j_p}^{(p)} \right\rangle \tag{2.89}$$

Using this auxiliary basis, the matrix elements of the mean-field operator matrix $\boldsymbol{\mathcal{H}}^{(\mathcal{K})}$ and the density matrix $\boldsymbol{\rho}^{(\mathcal{K})}$ are then expressed by

$$\mathcal{H}_{ab}^{(\mathcal{K})} = \left\langle \Psi_a^{(\mathcal{K})} \,\middle|\, \hat{H} \,\middle|\, \Psi_b^{(\mathcal{K})} \right\rangle \tag{2.90}$$

$$\rho_{ab}^{(\mathcal{K})} = \left\langle \Psi_a^{(\mathcal{K})} \,\middle|\, \Psi_b^{(\mathcal{K})} \right\rangle = \sum_{J^{\mathcal{K}}} A^*_{J_a^{\mathcal{K}}} A_{J_b^{\mathcal{K}}} \tag{2.91}$$

where the hole-index coefficient $J_a^{\mathcal{K}}$ works analogously to the former configuration coefficient, leaving out the $\mathcal{K}^{\text{th}}$ particle and replacing it with a numerical value a instead. Since inversion of this density matrix is required for the equation of motion (2.87), division by zero-valued elements would result in numerical instability. In practice, the density is thus regularized to always contain positive, non-zero values.

The uniqueness of the wavefunction is achieved by introducing an arbitrary constraint operator $\hat{g}^{(\mathcal{K})}$ for the time evolution of the SPF basis in the form

$$i\langle \varphi_i^{(\mathcal{K})} \mid \frac{\partial \varphi_j^{(\mathcal{K})}}{\partial t} \rangle = \langle \varphi_i^{(\mathcal{K})} \mid \hat{g}^{(\mathcal{K})} \mid \varphi_j^{(\mathcal{K})} \rangle \tag{2.92}$$

Adding this constraint to the equations of motion finally results in

$$i\frac{\partial \mathbf{A}}{\partial t} = \left(\boldsymbol{\mathcal{K}} - \sum_{\mathcal{K}} \mathbf{g}^{(\mathcal{K})} \right) \mathbf{A} \tag{2.93}$$

$$\text{and} \quad i\frac{\partial \boldsymbol{\varphi}^{(\mathcal{K})}}{\partial t} = \left[(\mathbf{g}^{(\mathcal{K})})^T + (1 - P^{(\mathcal{K})})(\boldsymbol{\rho}^{(\mathcal{K})})^{-1} \boldsymbol{\mathcal{H}}^{(\mathcal{K})} \right] \boldsymbol{\varphi}^{(\mathcal{K})} \tag{2.94}$$

Typical choices for $\mathbf{g}^{(\mathcal{K})}$ are either zero for all $\mathcal{K}$ or $\mathbf{g}^{(\mathcal{K})} = h^{\mathcal{K}}$ which is the analogue to the one-electron core-Hamiltonian introduced in equation (2.16). Depending on the choice of the constraint, the obtained SPFs are minimized with respect to different, additional properties like least motion of the SPFs. However, all of these representations are unitary transformations with respect to each other and likewise minimize the energy.

Product Form Hamiltonian

The remarkable efficiency of the MCTDH calculation method stems, however, not only from the highly flexible wavefunction but also from a large speed-up if the Hamiltonian (and the mean-field operator matrix $\boldsymbol{\mathcal{H}}^{(\mathcal{K})}$, likewise) may be brought into product form of one-particle operators

$$\hat{H}(q_1, \ldots, q_f) = \sum_{r=1}^{n_s} c_r h_r^{(1)}(Q_1) \ldots h_r^{(p)}(Q_p) \tag{2.95}$$

where the each of the n_s terms $h_r(Q_1)$ of the product representation are evaluated on a grid in terms of a discrete variable representation (DVR) of the SPFs. This representation is achieved by expanding the SPF basis $\varphi_j^{(\mathcal{K})}$ into a time-independent basis of so-called *primitive basis functions* $|\chi_k^{(\mathcal{K})}\rangle$

$$\varphi_j^{(\mathcal{K})}(Q_{\mathcal{K}}) = \sum_{k=1}^{N_{\mathcal{K}}} a_{kj}^{(\mathcal{K})} \chi_k^{(\mathcal{K})}(Q_{\mathcal{K}}) \tag{2.96}$$

where the basis functions have to be chosen such, that their matrix representation of the position operator $\hat{Q}^{(\mathcal{K})}$ is diagonal, i.e.

$$\langle \chi_k^{(\mathcal{K})} \mid \hat{Q}^{(\mathcal{K})} \mid \chi_j^{(\mathcal{K})} \rangle = Q_j^{(\mathcal{K})} \delta_{ij} \tag{2.97}$$

$Q_j^{(\mathcal{K})}$ refers to the value at grid point j with respect to the coordinate $Q_{\mathcal{K}}$ of particle $\mathcal{K}$. This special property then turns all off-diagonal matrix elements of fully local operators $\hat{O}_1(Q^{(K)})$ that depend only on one coordinate into zeros and

thus allows the evaluation of such operators in the form of simple sums at the quadrature points $Q_i^{(\mathcal{K})}$.

$$\left\langle \chi_{i_1}^{(1)} \dots \chi_{i_f}^{(p)} \,\middle|\, \hat{O}_1 \,\middle|\, \chi_{j_1}^{(1)} \dots \chi_{j_f}^{(p)} \right\rangle = \sum_{\mathcal{K}}^{p} O_1(Q_{j_1}^{(\mathcal{K})}, \dots, Q_{j_f}^{(\mathcal{K})}) \delta_{i_1 j_1} \dots \delta_{i_f j_f} \tag{2.98}$$

While the kinetic energy operator is already in the general form of such a locally acting operator $\hat{O}_1(Q^{(K)})$, non-local potentials such as the electron-electron repulsion are of the form $\hat{O}_2(Q^{(K)}, Q^{(L)})$ and require the coordinates of two particles. As an approximation, one may however use a fit of sums of products such that any arbitrary potential can be approximated as

$$V^{\text{app}}(Q^{(1)}, \dots, Q^{(p)}) = \sum_{j_1=1}^{m_1} \cdots \sum_{j_p=1}^{m_p} C_{j_1,\dots j_p} v_{j_1}^{(1)}(Q^{(1)}) \dots v_{j_p}^{(p)}(Q^{(p)}) \tag{2.99}$$

with single-particle potentials (SPP) $v_{j_\mathcal{K}}^{(\mathcal{K})}(Q^{(\mathcal{K})})$. Such a fitting procedure is implemented in the Heidelberg MCTDH program suite[64], [74] that was used throughout this work.

Excited States and Propagation

The antsymmetrized MCTDH wavefunction of equation (2.81) does not contain excited electronic states yet. Within this work, however, it was necessary to simulate the time evolution of an excited state. To include excited states, one may thus treat the electronic states in the form of an additional degree of freedom (DOF), i.e. by an additional state function $|\alpha\rangle$ that carries the information about all σ electronic state

$$\big|\Psi\big\rangle = \sum_{j_1=1}^{n_1} \cdots \sum_{j_{p-1}=1}^{n_{p-1}} \sum_{\alpha=1}^{\sigma} A_{j_1 \dots j_{p-1},\alpha} \,\big|\, \varphi_{j_1}^{(1)}\big\rangle \dots \,\big|\, \varphi_{j_{p-1}}^{(p-1)}\big\rangle \,\big|\, \alpha\big\rangle \tag{2.100}$$

This so called *single-set* formulation then uses the same sets of SPFs for each electronic state α. Similarly, the equations of motion need to include this additional degree of freedom as well for treating matrix elements between different electronic states $|\alpha\rangle$ and $|\beta\rangle$. For a constraint of $\mathbf{g}^{(\mathcal{K})} = 0$, these turn into

$$i\frac{\partial \mathbf{A}^{(\alpha)}}{\partial t} = \sum_{\beta=1}^{\sigma} \mathcal{K}^{(\alpha\beta)} \mathbf{A}^{(\beta)} \tag{2.101}$$

$$\text{and} \quad i\frac{\partial \boldsymbol{\varphi}^{(\mathcal{K},\alpha)}}{\partial t} = (1 - P^{(\mathcal{K},\alpha)})(\boldsymbol{\rho}^{(\mathcal{K},\alpha)})^{-1} \sum_{\beta=1}^{\sigma} \boldsymbol{\mathcal{H}}^{(\mathcal{K},\alpha\beta)} \boldsymbol{\varphi}^{(\mathcal{K},\beta)} \tag{2.102}$$

The matrix elements $\mathcal{K}_{JL}^{(\alpha\beta)}$ and $\mathcal{H}_{ab}^{(\mathcal{K},\alpha\beta)}$ are then obtained from applying the Hamiltonian $\hat{H}^{(\alpha\beta)} = \langle\alpha|\hat{H}|\beta\rangle$ according to

$$\mathcal{K}_{JL}^{(\alpha\beta)} = \left\langle \Phi_J^{(\alpha)} \,\middle|\, \hat{H}^{(\alpha\beta)} \,\middle|\, \Phi_L^{(\beta)} \right\rangle \tag{2.103}$$

$$\mathcal{H}_{ab}^{(\mathcal{K},\alpha\beta)} = \left\langle \Psi_a^{(\mathcal{K},\alpha)} \,\middle|\, \hat{H}^{(\alpha\beta)} \,\middle|\, \Psi_b^{(\mathcal{K},\beta)} \right\rangle \tag{2.104}$$

The energy of the MCTDH wavefunction is then minimized according to the variational principle by formally performing a *relaxation* calculation. This means, that one performs a propagation of the wavefunction in negative imaginary time and renormalizes the wavefunction afterwards

$$\Psi(t) = \frac{e^{-\hat{H}t}\Psi(t=0)}{||e^{-\hat{H}t}\Psi(t=0)||} \tag{2.105}$$

Excited states can be obtained by additionally requiring the orthogonality of the states as $\langle\alpha|\beta\rangle = \delta_{\alpha\beta}$. In practice, however, a convenient mathematical scheme called the *improved relaxation* can be applied, when the matrix elements $\mathcal{K}_{JL}^{(\alpha\beta)}$ are only re-evaluated after several propagation steps. This propagation scheme is called the constant mean field (CMF) scheme and relies on the fact that the Hamiltonian matrix elements as well as the products of the mean-field operator matrix $\mathcal{H}_{ab}^{(\mathcal{K},\alpha\beta)}$ and inverse densities $(\boldsymbol{\rho}^{(\mathcal{K},\alpha)})^{-1}$ do not change much over short time intervals. The full intricacies of these methods, as well as the form of the numerical propagation and diagonalisation algorithms (Runge-Kutta, short iterative Lanczos (SIL), Davidson) are, however, regarded as technical details that shall thus only be referenced here.[64] After the relaxation calculation, the propagation of electronic eigenstates only requires the use of a singular-state picture instead of a multi-state picture. Therefore, for all propagation calculations, the electronic state DOF may be removed again.

2.3 | Model System Descriptions and Computational Details

Since each of the investigations pursued in this dissertation has its own unique challenges with respect to system sizes, continuum contributions and the treatment of finite temperatures, different approximations and concepts were used to model the behaviour in each of the systems. Thus, after providing the background of the calculation methods in the last two sections, here, the applied approximations, model systems and computational details used for the separate projects shall be introduced.

2.3.1 | ICD in Charged Paired Quantum Dots

The goal of the first project discussed in this dissertation is investigating the ICD rate in a system of two charged quantum dots in a quantum wire with respect to changes in the geometry of the quantum dots. As schematically explained in the introduction section 1.2, the general prerequisite for the occurrence of ICD is that in an example system A^+−B there exists an excited bound state A^{+*}−B, the relaxation energy of which is larger than the work function for emitting an electron from B. In other words, a minimal working system of one photoexcitable absorber A^+ and one emitter particle B requires at least three one-electron states obeying the following energy conditions[39]

$$E(A^{+*}) > E(B) > E(A^+) \quad \text{with} \quad E(A^{+*}) - E(A^+) > -E(B) \; . \tag{2.106}$$

The surplus energy from the relaxation $A^{+*} \rightarrow A^+$ is then conserved in the form of the kinetic energies of the ejected electron and the Coulomb exploding particles A^+ and B^+. The rate with which the ICD process is driven can then be approximated by the golden rule expression[23]

$$\Gamma \approx \left| \left\langle k(\mathbf{r}) v_i(\mathbf{r}') \left| \frac{1}{|\mathbf{r} - \mathbf{r}'|} \right| v_f(\mathbf{r}) v_f'(\mathbf{r}') \right\rangle \right|^2 , \tag{2.107}$$

where k refers to the ejected electron's continuum one-electron wavefunction, v_i to the one-electron wavefunction of the initial vacancy in A^{+*} and v_f and v_f' to the final electronic state vacancies. Assuming further that the initial and final one-electron wavefunctions do not overlap, this expression can be simplified to yield the ICD rate Γ_{ICD} according to[38]

$$\Gamma_{\mathrm{ICD}} = \frac{3}{4\pi} \frac{\tilde{\sigma}_{\mathrm{E}}(E_{\mathrm{vph}}) \cdot \tau_{\mathrm{A}}^{-1}}{R^6 \cdot E_{\mathrm{vph}}^4} \quad \text{with} \quad E_{\mathrm{vph}} = E(A^{+*}) - E(A^+) \; , \tag{2.108}$$

where $\tilde{\sigma}_{\mathrm{E}}(E_{\mathrm{vph}})$ refers to the absorption cross section of the emitter at the virtual photon energy E_{vph} and τ_{A}^{-1} to the rate of spontaneous emission of the absorber electron. In other words, in the non-overlapping regime, the ICD process can be split up into the respective rates and probabilities for independent absorption of a virtual photon at the emitter and relaxation of the electron from $A^{+*} \rightarrow A^+$ in the absorber.

To study the ICD process for vertically arranged, negatively charged semiconductor quantum dots with varying heights and distances, a system of one absorber quantum dot (AQD) and one emitter quantum dot (EQD) is used. Since charge carriers in semiconducting materials move like in an effective potential of all other crystal lattice atoms and electrons, it is possible to assign an effective mass that depends on the exact material and then model only the behaviour of the free

charge carriers explicitly (effective mass approximation).[75]
Further, in the size regime of quantum dots, the electrons in semiconductor materials such as GaAs experience strong quantum confinement due to their large exciton Bohr radii.[76] This leads to a situation where the excited states become discrete in both energy as well as spatial extension. In such a scenario, the extended system may be collectively described by a single binding potential well.
Combining both of these concepts, a system of two, singly negatively charged quantum dots can be approximately described by two inverse Gaussian potential wells with two explicit electrons occupying one of the wells, each. Assuming a vertical arrangement of the QDs (i.e. growing in $\vec{z}$) with a strong harmonic oscillator confinement in $\vec{x}$ and $\vec{y}$, the wavefunction may be effectively separated into a time-independent function $\Psi(\mathbf{x}, \mathbf{y})$ and a time-dependent function $\Psi(\mathbf{z}, \mathbf{t})$. Considering only the relevant direction $\vec{z}$, a quasi one-dimensional model Hamiltonian for a paired QD (PQD) in a quantum wire can be given as

$$\hat{H}_{\mathrm{PQD}}(z_1, z_2) = \sum_{i=1}^{2} \left(-\frac{1}{2}\left(\frac{\partial}{\partial z_i}\right)^2 + V_{\mathrm{PQD}}(z_i) \right) + V(|z_1 - z_2|)_{\mathrm{1D}}^{(\omega_\perp)} \tag{2.109}$$

where $V_{\mathrm{PQD}}(z_i)$ is the binding potential with respect to the two QDs and $V(|z_1 - z_2|)_{\mathrm{1D}}^{(\omega_\perp)}$ is an effective quasi-1D Coulomb repulsion term, in which the constant contributions of $\Psi(\mathbf{x}, \mathbf{y})$ have been incorporated analytically with respect to the harmonic confinement strength $\omega_\perp$.[77] The PQD potential reads

$$V_{\mathrm{PQD}}(z_i) \;=\; \underbrace{-D_{\mathrm{A}}\; e^{-b_{\mathrm{A}}(z_i + \frac{R}{2})^2}}_{V_{\mathrm{A}}} \; \underbrace{-D_{\mathrm{E}}\; e^{-b_{\mathrm{E}}(z_i - \frac{R}{2})^2}}_{V_{\mathrm{E}}} \tag{2.110}$$

where the absorber QD's potential V_{A} is chosen such that it contains two bound one-electron levels, while the emitter QD's potential V_{E} contains only one bound one-electron level. Further, the energetic positioning of these one-electron levels is tailored such that they fulfil the energetic criterion for ICD (eq. (2.106)). Figure 2.1 schematically summarizes the relevant parameters of the charged paired quantum dot system.
To calculate the ICD rate of this system, the MCTDH formulation of the wavefunction is utilized (see section 2.2.3). In a first step, the ground and excited states of the system are calculated by improved relaxation.[64] The ground state of the system is referred to as A0E0, since it resembles a combination of the one-electronic ground states called A0 and E0, respectively. The ICD-relevant metastable resonance-state A1E0 is used for time propagation. Here, the electron in the absorber QD is in the first excited state, such that the dynamic relaxation A1 $\rightarrow$ A0 allows the ejection of the emitter electron from E0 into the continuum via ICD.

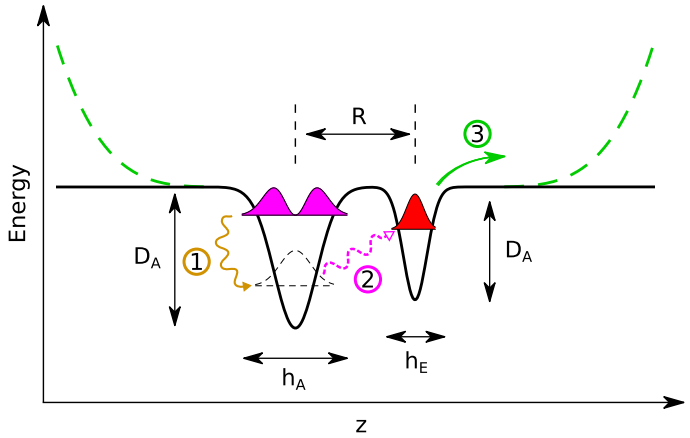

Figure 2.1: Schematic ICD processes in the charged paired quantum dot system with complex absorbing potentials (green dashed lines). The left and right potential wells refer to the absorber and emitter quantum dots with parameters D and h, respectively. Note that heights h were calculated in terms of the full width at half maximum of the inverse Gaussians in all occurrences. The centers of the QDs are apart by the interparticle distance R. Processes 1 to 3 depict the relaxation, virtual photon exchange and emission of the ICD electron, respectively.

For the time propagation, the Hamiltonian

$$\hat{H}_{\text{prop}}(z_1, z_2) = \sum_{i=1}^{2} \left(V_{\text{PQD}}(z_i) - \frac{1}{2}\left(\frac{\partial}{\partial z_i}\right)^2 - i\hat{W}_{\text{L}}(z_i) - i\hat{W}_{\text{R}}(z_i) \right) + V(|z_1 - z_2|)_{\text{1D}}^{(\omega_\perp)} \tag{2.111}$$

is used, that includes complex absorbing potentials (CAP) close to the simulation box edge. This way, the ejected electron is captured by the CAP instead of being reflected back at the infinitely high potential walls of the simulation box (green dashed lines in figure 2.1). Note that despite $\hat{H}_{\text{prop}}(z_1, z_2)$ being practically time-independent, the sudden placement of the electronically excited, metastable eigenstate A1E0 of Hamiltonian (2.109) onto the potential energy surface dictated by the Hamiltonian (2.111) initiates the dynamic relaxation process leading to ICD.

The interaction of the wavefunction with the CAP leads to a decrease in norm over time, according to

$$\frac{\partial}{\partial t} \left|\left| \Psi \right|\right|^2 = -2\eta \left\langle \Psi \,\middle|\, \hat{W} \,\middle|\, \Psi \right\rangle \tag{2.112}$$

where η is the strength parameter of the potential $\hat{W}$.[78] If the CAP is placed sufficiently far away of the initial state, then the norm loss can be used as a measure for determining the ICD rate. Another measure for the ICD rate, is the autocorrelation function $|a(t)|^2 = \langle \Phi_{\text{A1E0}}(\mathbf{z}, t = 0) \,|\, \Psi(\mathbf{z}, t) \rangle$, that reflects how similar the wavefunction $|\Psi\rangle$ at time t is compared to the initial-state function $|\Phi_{\text{A1E0}}\rangle$. Note that the wavefunction symbols were chosen to differ,

since $|\Phi_{\mathrm{A1E0}}\rangle$ is not an eigenstate to the propagation Hamiltonian of eq. (2.109). The interparticle Coulombic decay behaves as an exponential decay with respect to the ICD rate Γ_{ICD}, such that

$$|a(t)|^2 \propto e^{-\Gamma_{\mathrm{ICD}} t} \tag{2.113}$$

may be readily used to extract Γ_{ICD} from the autocorrelation function. Artifacts that occur in the first few propagation steps from $|\Phi_{\mathrm{A1E0}}\rangle$ to $|\Psi(t)\rangle$ typically stem from the above mentioned mismatch of Hamiltonians. Therefore, in praxis the first few time steps are typically discarded for fitting with respect to the exponential behaviour.
All calculations within the ICD project were conducted using the Heidelberg MCTDH program suite.[64],[74] Due to the high flexibility of its wavefunction form, MCTDH is suitable for describing the transition into continuum states. Additionally, the time-dependent treatment naturally incorporates the effects of dynamic electron correlation. The non-local potentials were brought into the appropriate product form with the Potfit algorithm[64] that is also included within the program suite. Further details on the calculation grid and such may be taken directly from the publication of section A.1.

2.3.2 | Database Reconstruction of Total X-Ray Absorption Spectra

The aim of the second research project was to establish a theoretical method that is able to extract local structural features from the generally randomized structure of graphene oxides. As a starting point for this study, the element-specific and surrounding-sensitive nature of X-ray absorption spectra is used. As shown in the work of DeBeer *et al.*,[79] the X-ray absorption (XA) spectra of small molecules with respect to a specific atom K-edge can be calculated as the sum of all possible single electron excitations from the respective localized 1s orbitals. Especially in cases where the 1s orbitals would be chemically equivalent like the chlorine 1s orbitals in their example $TiCl_4$,[79] this leads to a situation where one may instead calculate the excitation spectrum of one of the localized Cl 1s electron once and simply multiply the absorption spectra by four to recover the total absorption intensity. Consequently this shows that the total absorption spectrum of a molecule, can be calculated as the sum of all individual 1s-localized excitations with the specific oscillator strengths

$$f_{0n}^{\mathrm{ed}}(\omega_{0n}) = \frac{2}{3}\,\omega_{0n}\left|\left\langle\, 0 \,\middle|\, \sum_i \vec{r_i} \,\middle|\, n \,\right\rangle\right|^2 \tag{2.114}$$

$$f_{0n}^{\mathrm{md}}(\omega_{0n}) = \frac{2}{3}\,\alpha^2\,\omega_{0n}\left|\left\langle\, 0 \,\middle|\, \sum_i \frac{1}{2}(\vec{l_i} + 2\hat{s}_i) \,\middle|\, n \,\right\rangle\right|^2 \tag{2.115}$$

$$f_{0n}^{\mathrm{eq}}(\omega_{0n}) = \frac{1}{20}\,\alpha\,\omega_{0n}^{3} \sum_{a,b} \left| \left\langle\, 0 \,\middle|\, \sum_{i} \left(r_{i,a} r_{i,a} - \frac{r_i^2}{3}\delta_{ab} \right) \middle|\, n \,\right\rangle \right|^2 \tag{2.116}$$

where f^{ed} corresponds to the electric dipole moment, f^{md} to the magnetic dipole moment and f^{eq} to the electronic quadrupole moment. The N-electron wavefunctions used in these expressions are the ground state $|0\rangle$ and the excited state $|n\rangle$, which can be obtained from LR-TDDFT calculations. For the construction of the core-excited states $|n\rangle$, one electron was excited from one of the localized 1s orbitals into the space of all possible virtual orbitals. The excited states' oscillator strengths therefore implicitly depend on the overlap of the spatially localized 1s core-hole with the virtual space occupied after the respective excitation. Due to the spherical form of the 1s orbitals, there practically exists a radial sensitivity for the oscillator strengths with respect to the immediate chemical surrounding of the excited site. In case the virtual space populated during an excitation is strongly localized at a far away site, the associated oscillator are thus likely to be small. The energetic positioning for the transitions, however, still depend on the energy difference associated with the addressed target virtual space and may still change with respect to even far away chemical groups.

In the case of the studied graphitic π-conjugated systems of graphene oxides, the virtual orbital space is likely to be strongly delocalized. Therefore, it is expected that the individual excitation spectra are strongly influenced by said non-local effects. In the database reconstruction method developed in this work, an approximation is used where instead of the full surrounding, the individual atoms' XA spectra are distinguished only up to a specific number of chemically bonded neighbors with the aim to recover just as much of the non-local nature of the excitations as necessary. The concept of the database method can be explained with the following example:

Consider a conjugated, linear organic molecule with four carbon atoms labelled **ABCD** that are distinguishable by carrying different functional groups. Then the exact theoretical carbon K-edge X-ray spectrum $S(\mathbf{ABCD})$ can be calculated by individually exciting each 1s electron localized at each of the carbon atoms while considering the virtual orbitals of the full molecule and taking the sum of these single excitations

$$S(\mathbf{ABCD}) = S(\mathbf{A}bcd) + S(a\mathbf{B}cd) + S(ab\mathbf{C}d) + S(abc\mathbf{D}) \tag{2.117}$$

where $S(\mathbf{A}bcd)$ refers to an excitation of the 1s electron localized at **A**, while considering excitations into the virtual space spanned across all included atoms b, c and d. Note that the capitalized, bold font atom denotes which atomic site was excited. A zeroth-order approximation to the spectrum $S(\mathbf{ABCD})$ is then given by considering mean spectra $\tilde{S}$ from carbon atoms **A**, **B**, **C**, **D** in any possible environment.

$$S(\mathbf{ABCD}) \approx \tilde{S}(\mathbf{A}) + \tilde{S}(\mathbf{B}) + \tilde{S}(\mathbf{C}) + \tilde{S}(\mathbf{D}) \tag{2.118}$$

Here, the mean spectra $\tilde{S}(\mathbf{A})$ are obtained as a mean spectrum over all possible surroundings for atom **A**

$$\tilde{S}(\mathbf{A}) = \frac{1}{N} \cdot \left(S(\mathbf{A}bef) + S(\mathbf{A}gi) + S(\mathbf{A}llk) + \dots \right) , \tag{2.119}$$

where N is the number of spectra that are included in the mean spectrum of this specific functionalized atom. Note that the individual entries in the sum in parentheses are insensitive to the length of its entries and functionalizations, such that also entries with a different numbers of atoms than "**ABCD**" or atoms with other functional groups e, f, g,... occur. Also note that reducing this scheme to only one entry with a chain-length of one carbon atom results in the original idea of Hitchcock *et al.* for recovering the total spectrum by its most primitive and local components.

Now, consider the first-order approximation

$$S(\mathbf{ABCD}) \approx \tilde{S}(\mathbf{A}b) + \tilde{S}(a\mathbf{B}c) + \tilde{S}(b\mathbf{C}d) + \tilde{S}(c\mathbf{D}) \tag{2.120}$$

where the mean group spectra are required to at least match in their first rescpective neighbor atoms. By invoking the presence of the adjacent functional groups next to the excited center to be the same as in the actual molecule, the entries in the mean group spectra of the type $\tilde{S}(\mathbf{A}b)s$ will recover part of the non-local effects with respect to the virtual orbital space of their neighbors. Note, that also a termination "left from **A**" counts as a neighbor in the sense of being a termination. Therefore, taking this scheme to its extreme of collecting all neighbors (and terminations) into the mean group spectra one ultimately recovers the exact the spectrum.

One quickly realizes, however, that the extreme case is not a reduction of the problem for efficiently approximating the spectrum **ABCD**, since in this case the exact spectra would be contained in the database anyway. Therefore, the database method of mean group spectra becomes a powerful approximation only when the non-local effects extend over a low chain-length of neighbors. In other words, this means that one needs to verify the existence of a cut-off with respect to the number of neighbors beyond which the individual spectra become approximately indistinguishable.

Finally, these functionalization dependent mean group spectra may be used to attempt reconstructing experimentally obtained XA spectra and predict the possible functionalizations in even amorphous samples. As further verification tools,

the prediction may be cross-checked with experimentally obtained elemental compositions. Further, also other K-edge spectra like the oxygen K-edge may be used to simultaneously fit both experimental K-edges to increase the predictive power of the method.
Calculations of the molecular systems were performed with the ORCA program.[80] Further details on the choice of DFT and TDDFT functionals, basis sets and such may be taken from the publication presented in section A.2.

2.3.3 PCET Performance Rating and Dissipative TD-CI Electron Dynamics

To research the structure-property relationship between the oxygen functionalisation and the water-splitting capabilities of N-doped graphene oxide (NGO) quantum dots, a dynamic process needs to be investigated that includes several competing reaction channels. These channels correspond electronic state-to-state transitions due external laser fields, thermally induced vibronic transitions at finite temperatures as well as the dynamic transfer of a hydrogen atom (see figure 2.2).

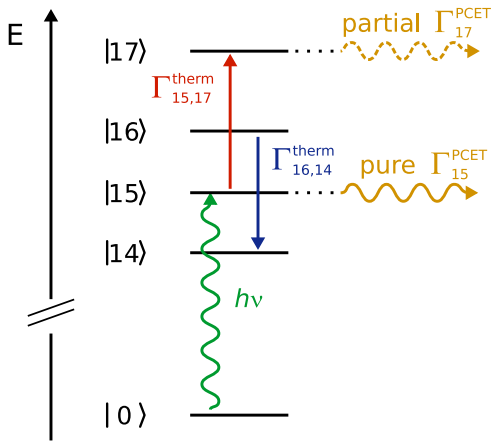

Figure 2.2: Schematic of the considered processes during proton-coupled electron transfer between electronic states $|i\rangle$. The initial excitation (green, $h\nu$) is followed by a vibronic thermalization between several electronically excited states (Γ^{therm}, red and blue). Eventually, upon reaching a more or less pure charge-transfer state with respect to the metric D_n^{CT} (eq. 2.122) , the wavepacket population may leave the system with respect to the combined PCET rate Γ^{PCET} (yellow). Reprinted from manuscript in review at *J. Phys. Chem. C*.[93]

Only when all of these rates are known, one can formulate a time-dependent electron dynamics scheme to simulate the efficiency of the proton-coupled electron-transfer process. To this effect, it is possible to calculate the necessary rates from a candidate NGO catalyst model molecule that has structurally been optimized with respect to the initial electron-transfer step (green wavy line in figure 2.2). The structural optimization proceeds by establishing a metric to rate potential candidate model molecules with respect to their electron-transfer

capabilities. By searching for the optimal candidate molecule structure with respect to this rating function, we avoid that the electron-transfer step is the rate-determining step in the overall proton-coupled electron transfer (PCET).[81] The form of this rating function is

$$F = D_n^{\mathrm{CT}}\ \mu_{0n}\ B_\lambda(\lambda_n, T)\ , \tag{2.121}$$

where D_n^{CT} is the charge-transfer purity for charge-transfer state n and μ_{0n} the transition dipole moment for driving the excitation of this state. The factor D_n^{CT} (2.122) itself is a measure for how much electron density is transferred from a neighboring water molecule onto the NGO model molecule during excitation of state n according to:

$$D_n^{\mathrm{CT}} = \left\langle \Psi_n^h \,\middle|\, \hat{P}_{\mathrm{H_2O}} \,\middle|\, \Psi_n^h \right\rangle \left\langle \Psi_n^p \,\middle|\, \hat{P}_{\mathrm{NGO}} \,\middle|\, \Psi_n^p \right\rangle\ . \tag{2.122}$$

It is obtained as the Mulliken projection $\hat{P}$ of the hole $|\Psi_n^h\rangle$ and particle $|\Psi_n^p\rangle$ wavefunctions onto the respective atomic basis wavefunctions that belong to the water (H_2O) or NGO molecule. Finally, since the desired goal is to initiate the charge transfer with sunlight, these two factors are multiplied with the blackbody radiation intensity of an emitter with a temperature T 5800 K

$$B_\lambda(\lambda, T) = \frac{2hc^2}{\lambda^5} \frac{1}{e^{hc/\lambda k_B T} - 1} \tag{2.123}$$

to weight the expression with the intensity of the sun spectrum at the excitation wavelength for the charge-transfer state. This way, the rating function F takes on high values for pure charge-transfer states with a high transition dipole moment and high sunlight input intensity to drive the excitation. The transition dipole moments and excited-state properties are obtained from TDDFT calculations as described in section 2.2.1.

The transformation into the basis of natural transition orbitals (NTO) is achieved by singular value decomposition (SVD) of the transition density matrices T^n

$$T_{ia}^n = \sum_\sigma \left\langle \Psi_n \,\middle|\, c_{i\sigma}^\dagger c_{a\sigma} \,\middle|\, \Psi_0 \right\rangle \tag{2.124}$$

which gives the overlap between the excited-state wavefunction $|\Psi_n\rangle$ and single-electron excitations of the ground-state wavefunction $|\Psi_0\rangle$ induced by the creation and annihilation operators $c_{i\sigma}^\dagger$ and $c_{a\sigma}$. The SVD of T^n then yields the three elements $T^n = U\Lambda V^\dagger$, where Λ is a diagonal matrix of coefficients reflecting the occupation Λ_{jj} of the respective j^{th} pair of single-hole and single-particle wavefunctions $|\psi_j^h\rangle$ and $|\psi_j^p\rangle$ derived from U and $V^\dagger$ according to

$$\left|\,\psi_j^h\right\rangle = \sum_i U_{ij}\left|\,\phi_i^o\right\rangle \qquad \left|\,\psi_j^p\right\rangle = \sum_i V_{ij}\left|\,\phi_i^v\right\rangle \tag{2.125}$$

$$\left|\,\Psi_n^h\right\rangle = \sum_j \Lambda_{jj}\left|\,\psi_j^h\right\rangle \qquad \left|\,\Psi_n^p\right\rangle = \sum_j \Lambda_{jj}\left|\,\psi_n^p\right\rangle \tag{2.126}$$

After optimization of the candidate molecule through employing this rating scheme to a large set of molecules, the relaxed reaction pathway (RRP) for abstracting a hydrogen from water towards the NGO nitrogen is calculated for the highest rated model molecule. For this, the distance between the water oxygen and the hydrogen atom is gradually increased to fixed values, while all other atomic coordinates are optimized through a DFT geometry optimization routine (section 2.1.3). By curve fitting the energetically lowest-lying, pure charge-transfer states to a parabola function with respect to the O–H distance, one may obtain a harmonic oscillator-like potential. From this potential, the classical oscillation time τ_n^{HT} of a particle with hydrogen-mass is calculated, assuming that the electronic state is conserved during the movement of the hydrogen atom. This oscillation time is assumed to be in the same order of magnitude as the actual time required to transfer a hydrogen atom from water to the NGO model.

Based on the electronic structure and the hydrogen-transfer time, the electron dynamics of the proton-coupled electron transfer is simulated by applying a modified Liouville-von Neumann equation (see section 2.2.2). In this modified version, the time evolution of the reduced density matrix $\hat{\rho}_1(t)$ reads

$$\frac{\partial\hat{\rho}_1(t)}{\partial t} = -\frac{i}{\hbar}\left[\hat{H}_{el},\hat{\rho}_1(t)\right] - \frac{1}{\hbar}\left[\hat{W},\hat{\rho}_1(t)\right]_+ + \frac{i}{\hbar}\left[\vec{\hat{\mu}}\cdot\vec{F}(t),\hat{\rho}_1(t)\right] + \hat{\hat{\mathcal{L}}}_{\mathcal{D}}\hat{\rho}_\infty(\sqcup) \tag{2.127}$$

where an additional anti-commutator term $-\frac{1}{\hbar}\left[\hat{W},\hat{\rho}_1(t)\right]_+$ leads to a norm loss with respect to the hydrogen transfer, in a similar way as the complex absorbing potential introduced in section 2.3.1. The potential operator $\hat{W}$ in this model reads

$$\hat{W} = \sum_n \Gamma_n^{\mathrm{PCET}}\left|\,\Psi_n\right\rangle\!\left\langle\Psi_n\,\right| = \sum_n \frac{D_n^{\mathrm{CT}}}{\tau_n^{\mathrm{HT}}}\left|\,\Psi_n\right\rangle\!\left\langle\Psi_n\,\right| \tag{2.128}$$

Within this expression, every state n is associated with a decay channel Γ_n^{PCET} that reduces the overall norm with a positive, non-zero rate that becomes exactly the inverse hydrogen-transfer time $(\tau_n^{\mathrm{HT}})^{-1}$ in case of pure charge transfer (where D_n^{CT} becomes 1). For all other channels, the rate is modulated by D_n^{CT}. Due to the projection operator $|\Psi_n\rangle\langle\Psi_n|$, the decay rate is also proportional to the momentary population of the respective state, so that charge transfer may

only occur from previously occupied states. Finally, the thermal dissipation introduced in the Louvillian super-operator $\hat{\hat{\mathcal{L}}}_{\mathcal{D}}\hat{\rho}(\sqcup)$ in equation (2.127) couples all states $|\Psi_n\rangle$ and $|\Psi_m\rangle$ to each other, via a Lindblad formalism of the form

$$\hat{\mathcal{L}}_D\hat{\rho}(t) = \sum_{mn} \frac{\Gamma_{mn}^{\text{therm}}}{2}\Big(\big[\hat{C}_{mn}, \hat{\rho}(t)\hat{C}_{mn}^{\dagger}\big] + \big[\hat{C}_{mn}\hat{\rho}(t), \hat{C}_{mn}^{\dagger}\big]\Big) \tag{2.129}$$

where the Lindblad operators $\hat{C}_{mn} = |\Psi_m\rangle\langle\Psi_n|$ steer the population transfer modulated by the individual channels-transfer rates $\Gamma_{mn}^{\text{therm}}$. These rates in turn are determined as a sum of values along a Lorentzian

$$\Gamma_{mn}^{\text{therm}} = \gamma \sum_q \left| \frac{(\gamma/2)^2}{(\Delta E_{mn} - \hbar\omega_q)^2 + (\gamma/2)^2} \right| \text{ , with } E_m > E_n \tag{2.130}$$

for the different vibration frequencies ω_q of the q normal modes of the molecular model system, with a width at half maximum of and scaled by the vibronic coupling strength parameter γ. This coupling strength parameter is therefore a handle to simulate more extended systems than the small model molecules, while keeping the general character of transitions between them in the picture of molecular vibrations ω_q. The effects of finite temperature are then modelled from invoking the detailed balance condition between the backwards and forward reaction rates in SI units $\Gamma_{mn} = \Gamma_{nm} \cdot \exp(-\hbar\Delta E_{mn}/k_B T)$.[83] In this expression k_B is the Bolltzmann constant and T is the temperature.

Initial computation of molecular properties and electronically excited states were performed with the ORCA program.[80] The ORCA output was then imported into the detCI ORBKIT program[82]–[84] to perform the time-propagation in the ρ-TDCI framework. Due to the capability of including the effects of thermal excitations and deexcitations in the reduced density formulation the method offers to study the impact of vibronic coupling in an approximate framework while also including the possibility to incorporate the hydrogen-transfer rate in the form of a complex absorbing term.

3 | Results and Conclusions

The overall goal of this PhD project was to critically investigate how model calculation techniques can be applied to predict the structure-property relationship of energy-related materials for different processes. This chapter therefore summarizes the most important methodologies that were established throughout this research and highlights findings of the individual subprojects in separate sections. At the end of each section, a conclusion is drawn with respect to the importance of the work and perspectives are outlined for future studies.

3.1 | ICD Rate Interdependence with Respect to Paired Quantum Dot Geometry

In the course of this work an established method[39],[85] for calculating the ICD rate of a paired quantum dot model system was used to study the interdependence of the ICD rate Γ_{ICD} with respect to several geometry parameters at once.
Earlier studies successfully probed connections between Γ_{ICD} and individual geometric parameter variations like the interparticle distance R,[39] absorber QD height h_{A}[85] and quantum dot width $r_{\perp}$[85] (i.e. thickness of the quantum wire) in both the explicit 3-dimensional system as well as the pseudo 1-dimensional system. It was found that shorter distances R as well as larger h_{A} lead to increased ICD rates, while a maximum was found with respect to a specific thickness $r_{\perp}$ of the wire. Since there exists no analogous term for the latter parameter in the asymptotic equation (2.108)[38] for predicting the ICD rate of atoms and small molecules, this equation is not necessarily fully transferable to quantum dots.
To further elucidate how the ICD rate changes under geometric control of the charged paired quantum dot system, in this work the remaining unprobed emitter height parameter h_{E} was investigated. Further, a scan for changing several geometrical parameters at the same time was performed to investigate whether there is an interdependence of the ICD rate with respect to R, h_{A} and h_{E}. For this purpose three different inter-particle distances R (88.62 to 108.36 nm) with five different absorber QD heights h_{A} (30.50 to 46.59 nm) and 64 emitter QD heights h_{E} (11.41 to 23.29 nm) were investigated (converted to real units of a GaAs system). Figure 3.1 shows the result of one two-dimensional scan for the parameters h_{E} and h_{A} for a fixed interparticle distance R.

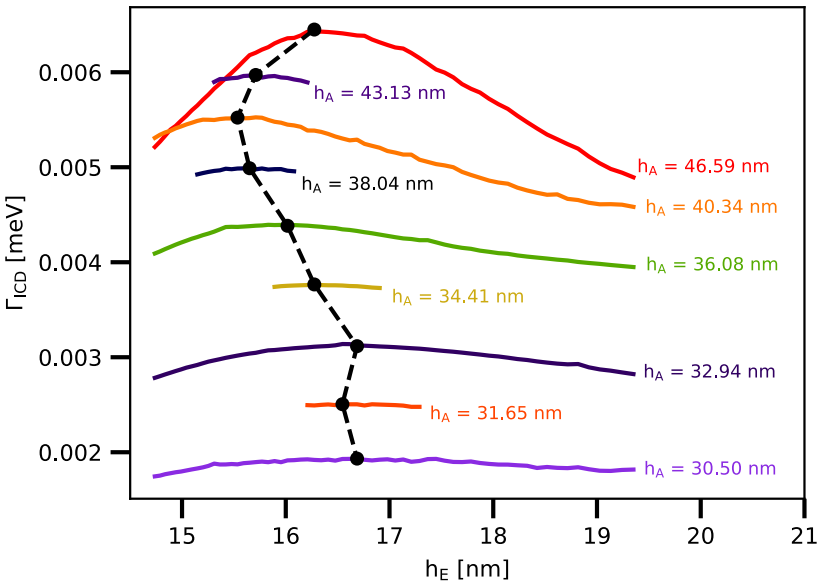

Figure 3.1: ICD rates in different charged PQD geometries with respect to the emitter height h_E and absorber height h_A at the fixed interparticle distance $R = 86.62$ nm. The dashed line connects the maxima of individual sets of parameter scans for better readability. SI units are obtained by applying the effective mass approximation with the material parameters for gallium arsenide (see A.1 for details). Reprint with permission from John Wiley and Sons©, 2017, for F. Weber *et al.*,[86] [A.1].

From this figure, one can confirm the previous finding that larger h_A typically result in larger ICD rates. Further, it can be seen that for a fixed h_A, a maximum ICD rate Γ_ICD can be found for a specific h_E. Although it is not possible to derive a formula for the maximum condition for h_E from a numerical parameter scan, one notices that the maxima of Γ_ICD with respect to the corresponding $h_\mathrm{E}^\mathrm{max}$ results in a rather smooth behaviour (see dashed line in figure 3.1). In fact, it could be shown that performing spline fits with respect to the maxima for different h_A is a valid tool to predict the maxima within small windows. This was confirmed by performing shorter scans around the spline-fit predicted values of $h_\mathrm{E}^\mathrm{max}$ (see short curves in figure 3.1).

Hence, it can be assumed that there exists a general, albeit non-trivial physical meaning to these maximum conditions. Indeed, by monitoring the behaviour of the systems' polarization and Coulomb repulsion between the two electrons with respect to h_E, two opposing effects are found that are likely responsible for the occurrence of the maxima. On the one hand, the Coulomb repulsion which is a measure for the effective distance between the electrons gets smaller for higher emitter QDs. These lower repulsions result in larger effective distances between the electrons R_eff, which in turn is expected to lower the ICD rate according to the asymptotic approximation that predicts a R^{-6} dependency. On the other hand, for higher emitter QDs a higher polarization of the system is found, which can be interpreted as sign for pre-ionization of the emitter electron. In other words,

when the emitter QD becomes more spacious, the electron within the emitter may move further away from the absorber QD's electron to minimize Coulomb repulsion, which reduces the likelihood for ICD due to a lower driving force. At the same time, this displacement of the emitter electron's wavefunction closer to the QD edge, facilitates ejection into the continuum.

Finally, by defining a joint metric called the rate-maximizing height-ratio $\chi(h_\mathrm{A}; R) = \frac{h_\mathrm{A}}{h_\mathrm{E}^\mathrm{max}}$ one can study the interdependence of the process in a direct way. In figure 3.2 the obtained rate maxima Γ_ICD are plotted against the rate-maximizing height-ratios for different interparticle distances R.

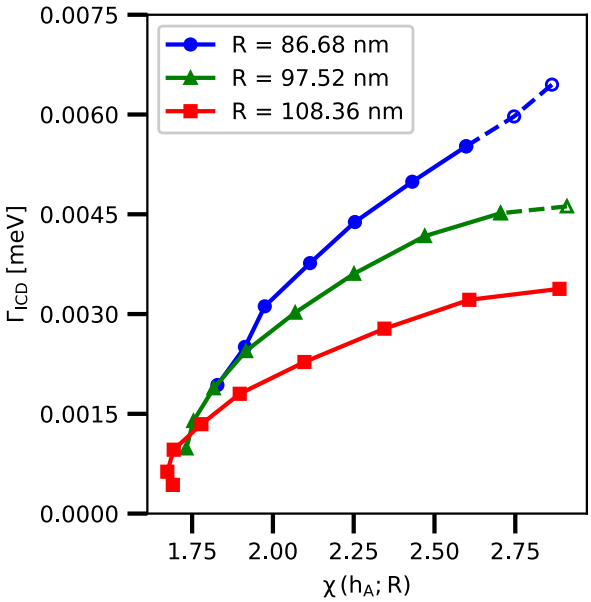

Figure 3.2: ICD rates with respect to rate-maximizing ratios. Note that while χ is independent of any units, it still depicts a specific set-up, such that not any pair of QD that follows a specific ratio will result in a maximum. Dashed lines and hollow markers were used in cases where the potential wells of the absorber and emitter QD started to overlap - thus marking a boundary region to an intra-molecular energy transfer instead of a purely inter-particle one, which is how ICD is defined. Reprint with permission from John Wiley and Sons©, 2017, for F. Weber *et al.*,[86] [A.1].

From this figure, one can reconfirm the trend that lower interparticle distances R generally tend to result in larger ICD rates due to a shorter effective distance between electrons. Further, the maximally achievable rates Γ_ICD seem to branch off from a shared (potentially) ideal behaviour curve for increasing height ratios. Therefore, one may consider these curves as an indicator for the existence of a physical limitation of the ICD process with respect to a true maximum ICD rate. Since recently, calculations for treating the continuum in more than one dimension[87] as well as more than three QD potentials and electrons became tractable,[88] it would be interesting to see in future work if the indicated physical limitations of a maximum ICD rate per emitter can be overcome in systems of

several emitter QDs and whether the general rate-maximizing height-ratios still maximize the overall rate.

3.2 | X-Ray Absorption Response Database for Graphene Oxides

The second project of this dissertation revolves around probing the surrounding-specific carbon K-edge X-ray absorption response of graphene oxides. In the seminal experimental work of Hitchcock *et al.*[89], [90] it was found that for small, saturated organic molecules the experimental carbon K-edge absorption of a larger compound can be qualitatively reproduced by summing up the contributions of individual constituent parts. This way the experimental spectrum of monochloroethane C_2H_5Cl can be approximately obtained by a weighted summation of the experimental spectra of methane CH_4 and monochloromethane CH_3Cl. The reasoning behind this phenomenon was that X-ray response of the 1s electron of the methyl carbon CH_3 behaves approximately as the one in methane, and the monochloromethyl CH_2Cl group would match the behaviour of the monochloromethane, respectively.
Consequently, the X-ray response of carbon 1s electrons can be assumed to be strongly locally dependent on the adjacent functional groups in such kinds of molecules. In their work, Hitchcock *et al.* assumed that the small differences in the summed spectra of saturated organic molecules do mostly occur from differences in the symmetry for the constituents and target molecule. For unsaturated organic molecules, however, the qualitative description was found to break down since energetic shifts of signals occur due to non-local effects of the strongly delocalized virtual space.
In the research projects covered in sections A.2 and A.3 a theoretical calculation method was established that can in principle recover these non-local effects by calculation of a database of surrounding-specific fingerprint spectra. Ultimately, the database can then be used to interpret experimental spectra. However, as outlined in section 2.3.2, the database approach only presents an efficient approximation if the surrounding-sensitivity of the X-ray absorption response is much smaller than the investigated system. By considering a simple model molecule (figure 3.3a)) it could be shown that graphitic model molecules the surrounding-sensitivity for the carbon K-edge reaches only up to two chemical bonds (2-3 Å) even in conjugated π systems.
In the model molecule shown in figure 3.3a), the circle- and diamond-marked atoms correspond to chemically identical atoms that result in fully identical X-ray absorption spectra (see 3.3b)). The triangle-marked atoms, however, are at different distances with respect to the epoxide oxygen while being in a similar surrounding up to two chemical bonds. However, despite being chemically differ-

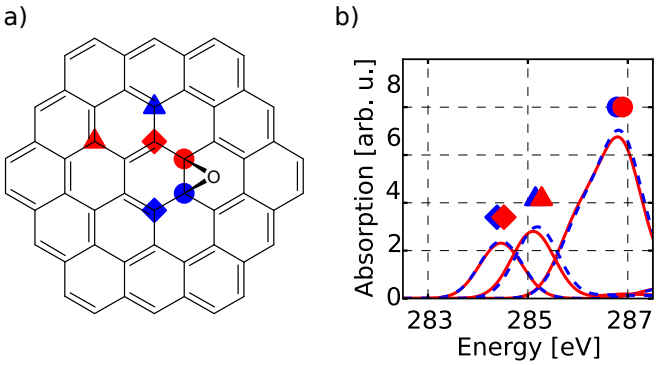

Figure 3.3: Comparison of local XA spectra (b) with respect to a model molecule (a). The spectra shown in (b) correspond to the local single-electron excitations of the 1s electrons at the marked atoms, respective of color and symbol. Reprint with permission of the PCCP Owner Societies© in accordance with the creative commons attribution 3.0 unported licence for F. Weber *et al.*,[91] [A.2], 2019.

ent groups and being embedded in an otherwise fully conjugated π-system, their corresponding X-ray absorption spectra only differ by about 0.1 eV in energetic position, while retaining almost identical intensity.

Following this proof of principle, a database was established using 28 different model molecules with varying functionalization patterns. The database that was obtained this way can cover all possible scenarios within the first-order approximation (also referred to as next nearest-neighbor (NNN) indexing) introduced in equation (2.120). Since this way, 28 exact theoretical spectra S were available, the composition $\tilde{S}$ of these spectra with respect to the first-order approximation was used as a sanity-check of the database.

In figure 3.4 two such comparisons are shown. The black solid lines in both spectra 3.4a) and c) present the exact theoretical result S, whereas the cumulative spectrum is the composition spectrum $\tilde{S}$ in first-order approximation for the two model molecules depicted in 3.4b) and d), respectively. The color-code for the summed-up components of the cumulative sum is a direct result of the atom count for the occurrence of specific groups $\tilde{S}(\mathbf{A}b)$.

From the cross-check it became apparent that this first-order compositions are already capable of reproducing most of the features from the respective exact spectra. Since the first-order database mean group spectra contain the characteristic features of the chemical environment of the excited atom, it is possible to assign peaks in a composed spectrum with respect to specific transition types (e.g. $\sigma^*(C{-}O)$) in the same way as in the analysis of experimental spectra. However, the method additionally provides a quantitative one-to-one mapping of how much a specific group of carbon atoms contributes to a signal.

This one-to-one mapping of intensity to individual group contributions may ultimately be used for fitting also experimental spectra with respect to the database mean group spectra to predict potential chemical compositions and functionaliza-

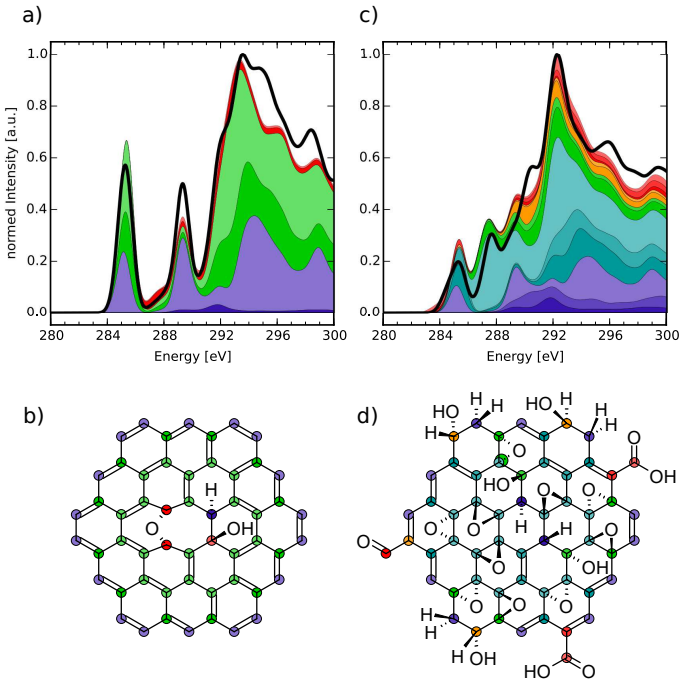

Figure 3.4: Comparison of exact theoretical spectra (black solid lines in (a) and (c)) with database compositions (cumulative sums of different groups, color-coded with respect to the respective carbon atoms) of two model molecules (b) and (d). Reprint with permission of the PCCP Owner Societies© in accordance with the creative commons attribution 3.0 unported licence for F. Weber *et al.*,[91] [A.2], 2019.

tion patterns up to the radius specified by the order of approximation. One such fit is shown in figure 3.5, where the cumulative sum of individual components was collected into four main contributions. The existence of the chemical groups that were identified with the database fit were confirmed by the experimentalists through additional measurements like infra-red spectroscopy (see A.3). The predicted elemental composition from the fitted composition was confirmed to lie within the typical range for graphene oxides.[43]

Finally, especially the one-to-one mapping of intensity to chemical groups allows to in principle identify extended structural regions in experimental spectra of amorphous substances, what makes the method appealing specifically for the study of graphene oxides. However, the methodology is not limited to the carbon K-edge and a simultaneous fit to the oxygen K-edge spectra is likely to improve the quality of the predictions, because the occurrence of any oxidized carbon group in the carbon K-edge fit dictates the occurrence of the same group in the oxygen K-edge fit.

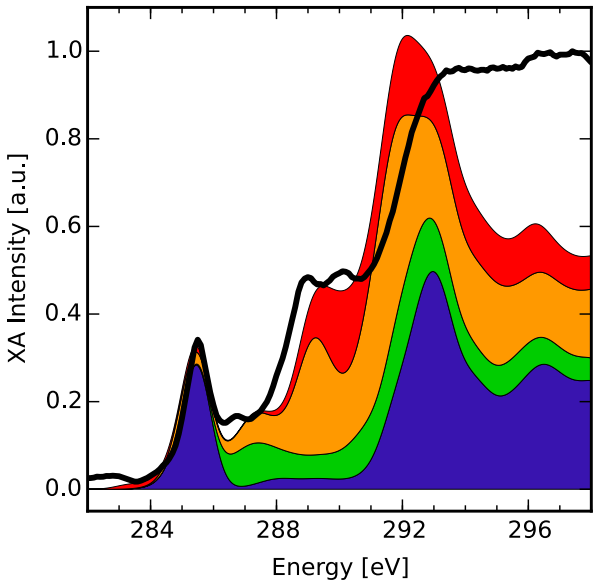

Figure 3.5: X-ray absorption database fit (colored sum spectrum) of an experimental total fluorescence yield measurement of a graphene oxide sample (black solid line). The composition of functional groups may be taken from [A.2]. Reprint with permission of the PCCP Owner Societies© in accordance with the creative commons attribution 3.0 unported licence for F. Weber *et al.*,[91] [A.2], 2019.

3.3 Proton-Coupled Electron-Transfer Dynamics of water splitting at N-doped Graphene Oxides

The third project of this dissertation had the goal to optimize a model QD system with respect to a dynamic process that requires describing an electronic as well atomic movement. The process under investigation is the proton-coupled electron transfer (PCET) in the water-splitting reaction on nitrogen-doped graphene oxide quantum dots (NGO-QD). Here, a water molecule that is close to a reaction site of an NGO-QD can be excited with light in the visible range to transfer both an electron and a proton onto the catalyst in a concerted way. Since this presents the first step in the overall water-splitting reaction it is of large interest to optimize its performance.

In this project, the overall optimization procedure was carried out in two separate steps. In the first step, the general molecular design principles that result in high electron-transfer capabilities from a water molecule onto a model molecular NGO-QD are investigated. The second step is concerned with finding the optimal non-adiabatic coupling strength in a model quantum dot at fixed finite temperature. This coupling strength is connected to the probability of vibronic

state-to-state transitions in the quantum dot which in turn can be controlled through the quantum dot size.

For the first step, a molecular design optimization scheme is applied, where every model molecule is assigned with a rating metric to discover the optimal design principles. The rating metric takes into account the transition dipole moment, the sunlight intensity at the respective excitation energy and charge-transfer purity (see equation (2.122)) for transitions that result in an electron transfer from water onto the model catalyst. This way, the molecular structure-property relations can be optimized with respect to the most efficient electron transfer under sunlight irradiation in a systematic way.

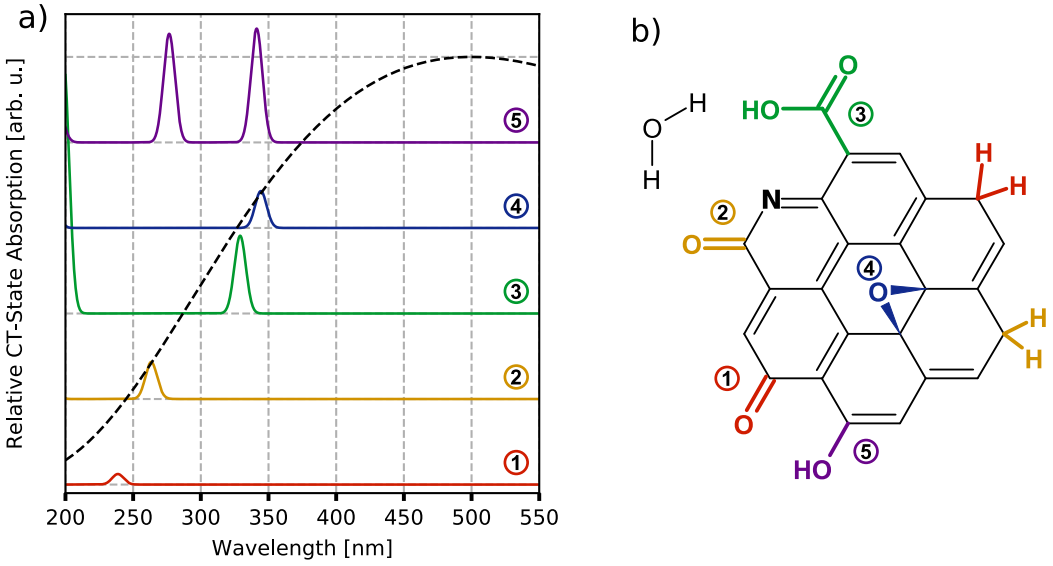

Figure 3.6: Comparison of NGO electron-transfer catalyst designs and performances. For each of the numbers, the respective group was added to the base scaffold shown in (b). The spectra in (a) are obtained from the UV/Vis absorption intensities of the respective molecules. The intensities of each signal in the theoretical line spectrum were weighted by their respective charge-transfer purity D_n^{CT} of eq. (2.122) and each line spectrum was Gauss-broadened with a full-width at half maximum of 5 nm. The dashed black line in the background represents the blackbody radiation spectrum at 5800 K. Reprinted from manuscript in review at *J. Phys. Chem. C*.[93]

The best candidate structure discovered during this molecular design optimization is shown in figure 3.6 along with the CT-purity-weighted absorption intensities in relative scale for each generation of the lead structure until the final candidate. CT-purity-weighting means that the absorption intensity of every excited state n was multiplied with its respective charge-transfer purity D_n^{TC} (see equation 2.122). From the comparison with the blackbody radiation spectrum at 5800 K (i.e. sunlight, dashed line), one can see that the CT-related absorption improves for each consecutive generation of adding a functional group to the scaffold. The highest impact on red-shifting the absorption energy from the ultraviolet regime towards the approximate sunlight radiation maximum was achieved

by addition of the carboxyl group (generation 3), since together with the ketone oxygen (generation 2) the oxygen atoms may form hydrogen bonds towards the water molecule that favours a co-planar arrangement of the water molecule. Addition of the epoxide group (generation 4) and of the phenol hydroxy-group (generation 5) finally red-shift the absorption signal to 341.2 nm and introduce a second charge-transfer channel at about 276.7 nm, while also strongly improving the absorption intensities.

After the candidate model molecule for the second optimization step had been decided upon, the potential energy surface for the dissociation of one hydrogen atom from the water molecule was investigated by calculation of the relaxed reaction pathway (RRP). To do this, constrained geometry optimizations were performed in which one of the O-H distances inside the water molecule was fixed at gradually increasing values while all other atoms were optimized freely. For each of the optimized structures along this reaction coordinate, the excited states were then determined with TDDFT and all excited states were analyzed with respect to their charge-transfer purity D_n^{CT}.

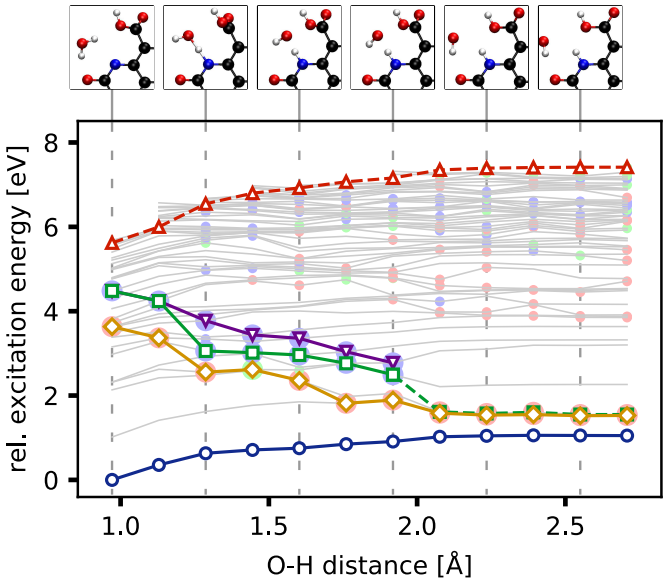

Figure 3.7: Relaxed Reaction Path and excited states for the water-splitting reaction at the NGO interface (below) and snapshots of the active center at highlighted O-H distances (above). The electronic ground state at each geometry is marked with blue circles, the energetically lowest-lying pure charge-transfer state is highlighted with yellow diamonds and partial charge-transfer states are given with green squares and purple triangles. Red triangles at the top indicate the ionization limit. Filled colored dots highlight further pure charge-transfer states (red, $D_n^{\mathrm{CT}} > 0.7$), intermediate charge-transfer states (green, $0.7 > D_n^{\mathrm{CT}} > 0.5$) and partial charge-transfer states (blue, $0.5 > D_n^{\mathrm{CT}} > 0.1$). Reprinted from manuscript in review at *J. Phys. Chem. C*.[93]

As can be seen in figure 3.7, the energetically lowest-lying pure charge-transfer state (yellow diamonds) shows a purely dissociative behaviour, since its total energy decreases for higher O-H distances. This implies that if the water-NGO

complex is brought into this pure charge-transfer state, the water-proton dissociates barrierless and thus leads to the desired product after proton-coupled electron transfer. From this dissociation curve, the time necessary to get from the starting geometry to the final point of the dissociation curve was calculated to be 7 fs using a simple classical molecular dynamics simulation indicating an ultrafast proton-transfer channel. Further, it was found that other relevant charge-transfer channels (green squares and purple triangles) basically followed the same dissociation dynamics. Therefore, it was assumed that each charge-transfer channel would approximately lead to the water-splitting within the same amount of time.

Using this information, the second optimization step for a model quantum dot was carried out. To this effect, an electron dynamics calculation method based on ρ-TDCI (see 2.2.2) was set up to simulate the PCET process in an NGO quantum dot at room temperature (300 K). In this simulation framework the hydrogen transfer is included as an negative imaginary coupling term in the Hamiltonian that affects all charge-transfer states. This means that whenever electron density is excited into one of the charge-transfer channels, the norm of the overall wavepacket decays with respect to the inverse hydrogen-transfer time modulated by the charge-transfer purity of this excited state. This way, the efficiency of the proton-coupled electron transfer can be directly related to the overall norm loss of the wavepacket. The thermally driven transitions between electronic states (i.e. dephasing) are modelled by Lindblad operators according to equation (2.129), where a parameter is introduced that scales the dephasing rates between states to simulate weak, intermediate and strong non-adiabatic coupling.

Using a moderately intense excitation field of 3.51×10^{13} W/cm^2 with a single pulse of 50 fs length and a carrier frequency that matches the excitation energy for the lowest-lying pure charge-transfer state, the electron dynamics shown in figure 3.8 are obtained.

In the initial excitation dynamics (left panel of 3.8) the norm only decreases by a small amount, indicating that despite using a matching excitation energy the charge-transfer states are almost not populated. Indeed, when looking at the populations of the partial and pure charge-transfer states almost no population is transferred to these states (note that the curves were scaled for better readability). The reason for this is that the imaginary potential that drives the hydrogen- and thermal population-transfer channels practically hinders the excitation into the charge-transfer states by causing an ultrafast dephasing between the ground and all other states. In other words the pure ground state in the density matrix to which the resonance condition applies to, is almost never occupied but instead is in constant exchange with other mixed states that are slightly off from the resonance condition. This way, rather than exciting the pure ground state into the desired pure charge-transfer states, a mixed state is excited into a multitude of excited mixed states that mostly consist of non-charge-transfer states.

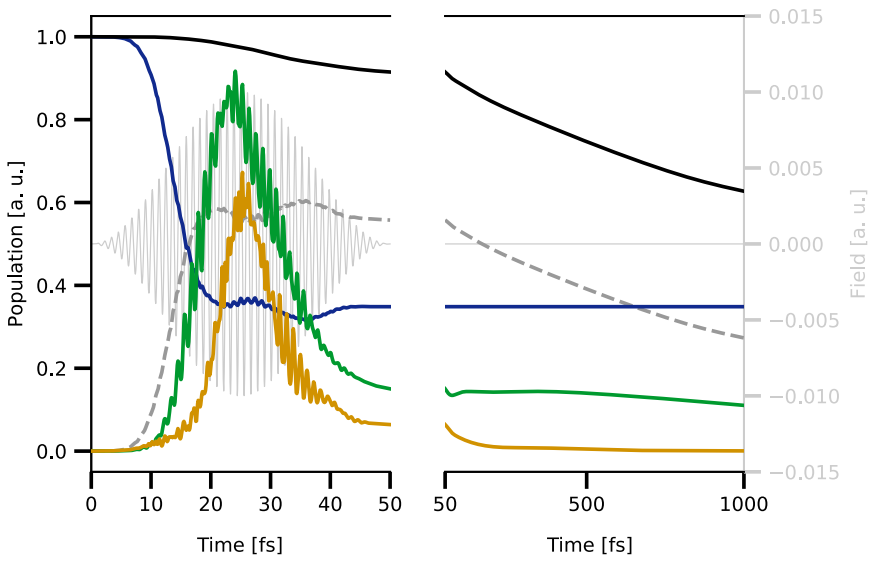

Figure 3.8: Electron dynamics of the proton-coupled electron-transfer process in NGO QDs at 300 K during initial excitation dynamics over 50 fs (left) and after laser-shutdown until 1 ps (right). Shown are the norm (black) the laser field (thin light grey), and populations of the ground state (blue), all pure charge-transfer states (orange, scaled by factor 50), all partial charge-transfer states (green, scaled by factor 20) and the sum of all remaining non-charge-transfer states (dark grey dashed). Reprinted from manuscript in review at *J. Phys. Chem. C*.[93]

In the subsequent field-free propagation (right panel of 3.8), these non-charge-transfer states then slowly cause a norm loss due to secondary PCET by transferring population to partial charge-transfer states via thermalization (i.e. non-adiabatic, vibronic coupling). By probing three different oders of magnitude for the non-adiabatic coupling strengths, the above case was identified to yield the highest overall norm loss. Here, the vibronic state-to-state rates translate to an NGO-QD system with phonon lifetimes of approximately 1 ps. Both higher, as well as lower coupling strengths result in less norm loss due to secondary PCET. The reason for this is, that the secondary PCET route is the most efficient when the thermalization rates towards the charge-transfer states are on a similar order of magnitude as the PCET rate from these charge-transfer states. If the thermalization between states proceeds faster than the PCET, the population-transfer channels back and forth between non-CT channels dominate over decaying via the PCET channels. On the other hand, if the thermalization towards the charge-transfer states is much slower, then the thermalization limits the overall possible PCET rate.

Consequently, it is to be expected that thre phonon lifetime within real quantum dot catalysts (which is closely related to the thermalization times and thus the non-adiabatic coupling) will play an important role for the efficiency of the PCET process. Further, comparing the very fast hydrogen-transfer time with the excitation dynamics it is apparent that the rate-determining factor for PCET is

initiating the electron transfer rather than the hydrogen transfer. Therefore, to maximize the PCET rate it is desirable to find even better active centres than the one proposed here. If the current model system was used as a colloidal catalyst with N active sites that is excited according to the above simulation, the calculated norm loss suggests that it is capable of initiating PCET in about $N \cdot 37\%$ of water molecules in one picosecond. Note, that this mapping of a norm loss to a number of occurrences is valid in the sense that the density matrix formalism, by design, allows to describe probabilities in ensembles of arbitrary size.
To confirm the general predictive power of the proposed model calculation method it is highly desirable to have experimental data on such water-splitting experiments with a known molecular catalysts of tractable system size. Further, a confirmation for the method could also be achieved by studying other molecular systems where experimental data has been collected already, like for the molecules of the graphitic carbon-nitride family.

Bibliography and Resources

Bibliography

[1] Hardin, G., *Science* 162, **1968**, 1243.

[2] Digital copy of the Montreal Handbook 13th edition (**2019**): `https://ozone.unep.org/sites/default/files/2019-08/MP_Handbook_2019_1.pdf` (Accessed Sep. 27th, 2019)

[3] Digital copy of the UNFCCC treaty (**1992**): `https://treaties.un.org/doc/Treaties/1994/03/19940321%2004-56%20AM/Ch_XXVII_07p.pdf` (Accessed Sep. 27th, 2019)

[4] Morton, O., *Nature* 443, **2006**, 19.

[5] BP Statistical Review of World Energy 2019 (BP, **2019**): `https://www.bp.com/content/dam/bp/business-sites/en/global/corporate/pdfs/energy-economics/statistical-review/bp-stats-review-2019-full-report.pdf` (Accessed Sep. 27th, 2019)

[6] Yoshikawa, K., Kawasaki, H., Yoshida, W., Irie, T., Konishi, K., Nakano, K., Uto, T., Adachi, D., Kanematsu, M., Uzu, H., Yamamoto, K., *Nat. Energy* 2, **2017**, 17032.

[7] Charts for surface areas of the planet: `http://www.physicalgeography.net/fundamentals/8o.html` (Accessed Sep. 27th, 2019)

[8] Governmental Information about the Great Lakes: `https://www.glerl.noaa.gov/education/ourlakes/lakes.html` (Accessed Sep. 27th, 2019)

[9] Governmental Information about Japan's area: `https://www.cia.gov/library/publications/the-world-factbook/geos/ja.html` (Accessed Sep. 27th, 2019)

[10] Luceño-Sánchez, J. A., Díez-Pascual, A. M., Peña Capilla, R., *Int. J. Mol. Sci.* 20, **2019**, 976.

[11] Akbari, H., Browne, M. C., Ortega, A., Huang, M. J., Hewitt, N. J., Norton, B., McCormack, S. J., *Solar Energy* 192, **2018**, 144.

[12] Cambié, D., Noël, T., *Top. Curr. Chem.* 376, **2018**, 45.

[13] Chang, X. , Wanga, T., Gong, J., *Energy Environ. Sci.* 9, **2016**, 2177.

[14] Zhang, Q., Hao, F., Li, J., Zhou, Y., Wei, Y., Lin, H., *Sci. Technol. Adv. Mater.* 19, **2019**, 426.

[15] Magelhães, P., Andrade, L., Nunes, O. C., Mendes, A., *Rev. Adv. Mater. Sci.* 51, **2017**, 91.

[16] MacIsaac, D., Kanner, G., Anderson, G., *Phys. Teach.* 37, **1999**, 520.

[17] Kyba, C. C. M., Hänel, A., Hölker, F., *Energy Environ. Sci.* 7, **2014**, 1806.

[18] Ganandran, G. S. B., Mahlia, T. M. I., Ong, H. C., Rismanchi, B., Chong, W. T., *Sci. World J.* 2014, **2014**, 745894.

[19] Pokropivny, V.V., Skorokhod, V.V., *Mater. Sci. Eng. C* 27, **2007**, 990.

[20] Ashoori, R. C., *Nature* 379, **1996**, 413.

[21] Bera, D., Qian, L., Tseng, T.-K., Holloway, P. H., *Materials* 3, **2010**, 2260.

[22] Andrews, D. L., Bradshaw, D. S., *Eur. J. Phys.* 25, **2004**, 845.

[23] Cederbaum, L. S., Zobeley, J., Tarantelli, F., *Phys. Rev. Lett.* 79, **1997**, 4778.

[24] Auger, P., *Comptes Rendus* 180, **1925**, 65.

[25] Thissen, R., Lablanquie, P., Hall, R.I., Ukai, M., Ito, K., *Eur. Phys. J. D* 4, **1998**, 335.

[26] Marburger, S., Kugeler, O., Hergenhahn, U., *Phys. Rev. Lett.* 90, **2003**, 203401.

[27] T. Jahnke, A. Czasch, M. S. Schöffler, S. Schössler, A. Knapp, M. Käsz, J. Titze, C. Wimmer, K. Kreidi, R. E. Grisenti, A. Staudte, O. Jagutzki, U. Hergenhahn, H. Schmidt-Böcking, and R. Dörner, *Phys. Rev. Lett.* 93, **2004**, 163401.

[28] Aziz, E. F., Ottosson, N., Faubel, M., Hertel, I. V., Winter, B., *Nature* 455, **2008**, 89.

[29] Winter, B., *Nucl. Instrum. Methods Phys. Res* 601, **2009**, 139.

[30] Jahnke, T., Sann, H., Havermeier, T., Kreidi, K., Stuck, C., Meckel, M., Schöffler, M., Neumann, N., Wallauer, R., Voss, S., Czasch, A., Jagutzki, O., Malakzadeh, A., Afaneh, F., Weber, Th., Schmidt-Böcking, H., Dörner, R., *Nat. Phys.* 6, **2010**, 139.

[31] Zobeley, J., Santra, R., Cederbaum, L. S., *J. Chem. Phys.* 115, **2001**, 5076

[32] Morishita, Y., Saito, N., Suzuki, I. H., Fukuzawa, H., Liu, X.-J., Sakai, K., Prümper, G., Ueda, K., Iwayama, H., Nagaya, K., *J. Phys. B: At. Mol. Opt. Phys.* 41, **2008**, 025101.

[33] Sisourat, N., Sann, H., Kryzhevoi, N. V., Kolorenč, P., Havermeier, T., Sturm, F., Jahnke, T., Kim, H.-K., Dörner, R., Cederbaum, L. S., *Phys. Rev. Lett.* 100, **2010**, 022706.

[34] Hoener, M., Rolles, D., Aguilar, A., Bilodeau, R. C., Esteves, D., Olalde Velasco, P., Pešić, Z. D., Red, E., Berrah, N., *Phys. Rev. A* 81, **2010**, 021201.

[35] Miteva, T., Kazandjian, S., Kolorenč, P., Votavová, P., Sisourat, N., *Phys. Rev. Lett.* 119, **2017**, 083403.

[36] Votavová, P., Miteva, T., Engin, S., Kazandjian, S., Kolorenč, P., Sisourat, N., *Phys. Rev. A* 100, **2019**, 022706.

[37] Öhrwall, G., Tchaplyguine, M., Lundwall, M., Feifel, R., Bergersen, H., Rander, T., Lindblad, A., Schulz, J., Peredkov, S., Barth, S., Marburger, S., Hergenhahn, U., Svensson, S., Björneholm, O., *Phys. Rev. Lett.* 93, **2004**, 173401.

[38] Averbukh, V., Müller, I. B., Cederbaum, L. S., *Phys. Rev. Lett.* 93, **2004**, 263002.

[39] Bande, A., Gokhberg, K., Cederbaum, L. S., *J. Chem. Phys.* 135, **2011**, 144112.

[40] Choi, W., Lahiri, I., Seelaboyina, R., Kang, Y. S., *Crit. Rev. Solid State Mater. Sci.* 35, **2010**, 52.

[41] Yeh, T.-F., Cihlář, J., Chang, C.-Y., Cheng, C., Teng, H., *Mater. Today* 16, **2013**, 78.

[42] Yeh, T.-T., Teng, C.-Y., Chen, S.-J., Teng, H., *Adv. Mater.* 26, **2014**, 3297.

[43] Hummers, W. S., Offeman, R. E., *J. Am. Chem. Soc.* 80, **1958**, 1339.

[44] Dimiev, A. M., Bachilo, S. M., Saito, R., Tour, J. M., *ACS Nano* 6, **2012**, 7842.

[45] Eigler, S., Hirsch, A., *Angew. Chem. Int. Ed.* 53, **2014**, 7720.

[46] Rozada, R., Paredes, J. I., Villar-Rodil, S., Martínez-Alonso, A., Tascón, J. M. D., *Nano Res.* 6, **2013**, 216.

[47] Matsumoto, Y., Koinuma, M., Ida, S., Hayami, S., Taniguchi, T., Hatakeyama, K., Tateishi, H., Watanabe, Y., Amano S., *J. Phys. Chem. C* 115, **2011**, 19280.

[48] Erickson, K., Erni, R., Lee, Z., Alem, N., Gannett, W., Zettl, A., *Adv. Mater.* 22, **2010**, 4467.

[49] Hammes-Schiffer, S., *J. Am. Chem. Soc.* 137, **2015**, 8860.

[50] Szabo, A., Ostlund, N. S., *"Modern Quantum Chemistry"*, Dover Publications Inc., **1996**.

[51] Planck, M., *"The theory of heat radiation"*, P. Blakiston's Son & Co., **1914**.

[52] Einstein, A., *Ann. Phys.* 322, **1905**, 132.

[53] Newton, I., "Philosophiæ Naturalis Principia Mathematica", original New Latin version of **1687**, scan of English translation from **1846** available at: `https://archive.org/details/newtonspmathema00newtrich` (Accessed Oct. 5th, 2019)

[54] Parr, R. G., Yang, W., *"Density-Functional Theory of Atoms and Molecules"*, Oxford University Press, **1994**.

[55] Møller, C., Plesset, M. S., *Phys. Rev.* 46, **1934**, 618.

[56] Čiǰek, J., *J. Chem. Phys.* 45, **1966**, 4256.

[57] Hohenberg, P., Kohn, W., *Phys. Rev.* 136, **1964**, 864.

[58] Perdew, J. P., Burke, K., Ernzerhof, M., *Phys. Rev. Lett.* 77, **1996**, 3865.

[59] Tran, F., Stelzl, J., Blaha, P., *J. Chem. Phsys.* 144, **2016**, 204120.

[60] Dirac, P. A. M., Bohr, N. H. D., *Proc. R. Soc. Lond. A* 114, **1927**, 243.

[61] Tannor, D. J., *"Introduction to Quantum Mechanics"*, University Science Books, **2007**.

[62] Kato, T., *J. Phys. Soc. Jpn.* 5, **1950**, 435.

[63] Breuer, H.-P., Petruccione, F., *"The Theory of Open Quantum Systems"*, Oxford University Press, **2007**.

[64] Meyer, H.-D., Gatti, F., Worth, G. A., *"Multidimensional Quantum Dynamics"*, Wiley-VCH, **2009**.

[65] Gross, E. K. U., and N. T. Maitra, Chapter on Introduction to TDDFT in *"Fundamentals of Time-Dependent Density Functional Theory"*, Springer, **2012**, 53.

[66] Casida, M. E., Huix-Rotllant, M., *Annu. Rev. Phys. Chem.* 63, **2012**, 287.

[67] Casida, M. E., Phys. Rev. A 51, **1995**, 2005.

[68] Klamroth, T., *Phys. Rev. B* 68, **2003**, 245421.

[69] Krause, P., Klamroth, T., Saalfrank, P., *J. Chem. Phys.* 123, **2005**, 074105.

[70] Krause, P., Klamroth, T., Saalfrank, P., *J. Chem. Phys.* 127, **2007**, 034107.

[71] Hecht, K., *"Quantum Mechanics"*, Springer, **2000**, pp 598.

[72] Tremblay, J. C., Klamroth, T., Saalfrank, P., *J. Chem. Phys.* 129, **2008**, 084302.

[73] Nakatani, M., Ogawa, T., *J. Phys. Soc. Jpn.* 79, **2009**, 084401.

[74] Beck, M. H., Jäckle, A., Worth, G. A., Meyer, H.-D., *Phys. Rep.* 324, **2000**, 1.

[75] Schooss, D., Mews, A., Eychmüller, A., Weller, H., *Phys. Rev. B* 49, **1994**, 17072.

[76] Yoffe, A. D., *Adv. Phys.* 42, **1993**, 173.

[77] Bednarek, S., Szafran, B., Chwiej, T., Adamowski, J., *Phys. Rev. B* 68, **2003**, 045328.

[78] Meyer, H.-D., Lecture Notes "INTRODUCTION TO MCTDH", available online: `https://www.pci.uni-heidelberg.de/tc/usr/mctdh/lit/intro_MCTDH.pdf`
(Accessed Dec. 4th, 2019)

[79] DeBeer George, S., Petrenko, T., Neese, F., *Inorganica Chim. Acta* 361, **2008**, 965.

[80] Neese, F., *WIREs Comput. Mol. Sci.* 8, **2018**, e1327.

[81] Navrotskaya, I., Hammes-Schiffer, S., *J. Chem. Phys.* 131, **2009**, 024112.

[82] Hermann, G., Tremblay, J.C., *J. Chem. Phys.* 145, **2016**, 174704.

[83] Klinkusch, S., Tremblay, J. C., *J. Chem. Phys.* 144, **2016**, 184108.

[84] Hermann, G., Pohl, V., Tremblay, J.C., *J. Comput. Chem.* 38, **2017**, 2378.

[85] Dolbundalchok, P., Peláez, D., Aziz, E. F., Bande, A., *J. Comput. Chem.* 37, **2016**, 2249.

[86] Weber, F., Aziz, E. F., Bande, A., *J. Comput. Chem.* 38, **2017**, 2141.

[87] Haller, A., Peláez, D., Bande, A., *J. Phys. Chem. C* 123, **2019**, 14754.

[88] Langkabel, F., Lützner, M., Bande, A., *J. Phys. Chem. C* 123, **2019**, 21757.

[89] Hitchcock, A.P., Brion, C.E., *J. Electron Spectrosc. Relat. Phenom.* 14, **1978**, 417.

[90] Ishii, I., Hitchcock, A. P., *J. Electron. Spectrosc. Relat. Phenom.* 46, **1988**, 55.

[91] Weber, F., Ren, J., Petit, T., Bande, A., *Phys. Chem. Chem. Phys.* 21, **2019**, 6999.

[92] Ren, J., Weber, F., Weigert, F., Wang, Y., Choudhury, S., Xiao, J., Lauermann, I., Resch-Genger, U., Bande, A., Petit, T., Nanoscale, **2019**, 11, 2056.

[93] Weber, F., Tremblay, J. C., Bande, A., *J. Phys. Chem. C*, submitted **2019**, *in peer-review.*

Further Resources

This document was compiled using the Texmaker (v5.0.3) LaTeX compiler. Pictures displaying data were generated using the matplotlib package for python. Lewis structures of molecules were prepared in the ACD/ChemSketch program (v14.01). The logo on the cover page was designed with the blender software (v2.79b). The licenses for textures used in this graphic were obtained from the texture database at `https://www.textures.com`. Post-processing of vector graphics was done using Inkscape (v0.92.3).

A | Publications

A.1 | Interdependence of ICD rates in paired quantum dots on geometry

Fabian Weber, Emad F. Aziz, Annika Bande
J. Comput. Chem., **2017**, 2141 - 2150

DOI: 10.1002/jcc.24843
URL: `https://doi.org/10.1002/jcc.24843`

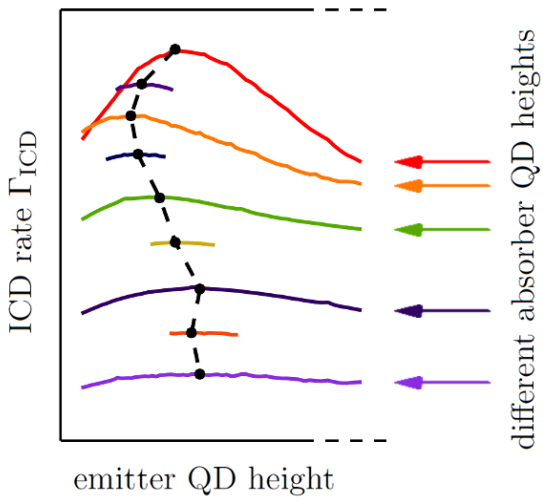

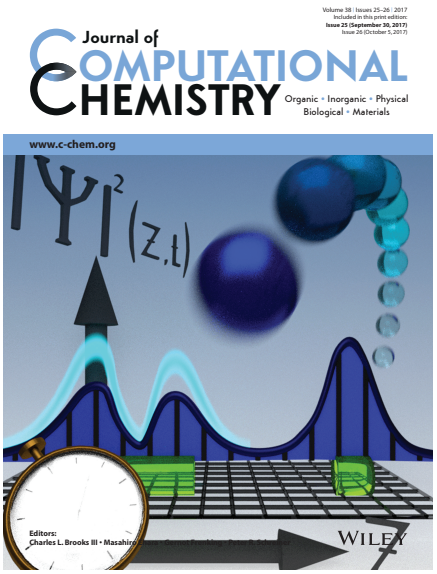

Author Contributions: The initial research plan for this project was laid out by AB. The calculations and analysis of the results was performed by **FW**. The project goals were refined during the research period in a joint meeting of the authors under scientific guidance of AB. The manuscript was written by **FW** under the supervision of AB. The authors agreed on submitting a cover page for this article that was designed by **FW**.

A.2 | Theoretical X-ray absorption spectroscopy database analysis for oxidized 2D carbon nanomaterials

Fabian Weber, Jian Ren, Tristan Petit, Annika Bande
Phys. Chem. Chem. Phys., **2019**, 6999 - 7008

DOI: 10.1039/c8cp06620e
URL: `https://doi.org/10.1039/c8cp06620e`

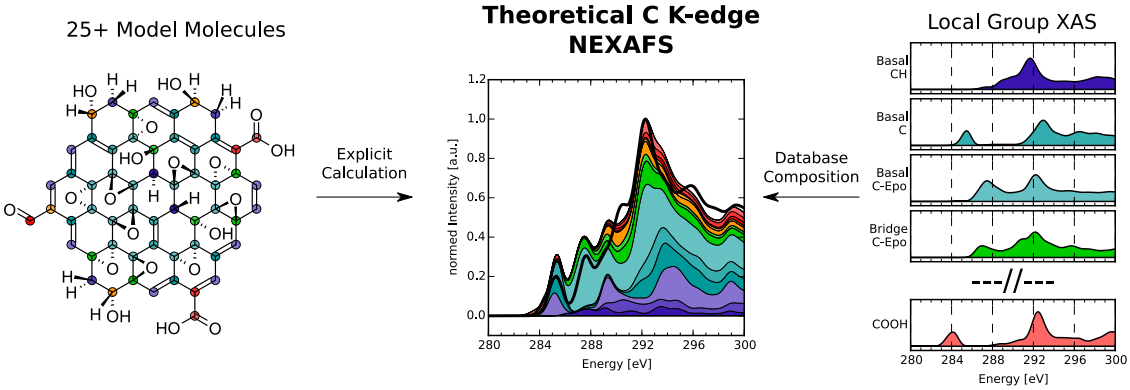

Author Contributions: In the initial calculations on XA absorption spectra for the co-author article A.3 performed by **FW** it became apparent that an individual database project subject to this paper could be formulated. The decision to pursue this research project in parallel to A.3 was made predominantly by the theoretical-chemistry authors AB and **FW**. The set-up of the database framework and the calculation of its entries were performed by **FW**. The goals during ongoing research were refined in joint meetings between all authors. TP and JR provided experimental spectra for a comparison study and supported AB and **FW** with respect to all related questions. The manuscript was prepared by **FW** under scientific guidance by AB and TP. The detailed description of experimental parameters were provided by JR.

A.3 | Influence of surface chemistry on optical, chemical and electronic properties of blue luminescent carbon dots

Jian Ren, Fabian Weber, Florian Weigert, Yajie Wang, Sneha Choudhury, Jie Xiao, Iver Lauermann, Ute Resch-Genger, Annika Bande, Tristan Petit
Nanoscale, **2019**, 2056 - 2064

DOI: 10.1039/c8nr08595a
URL: `https://doi.org/10.1039/C8NR08595A`

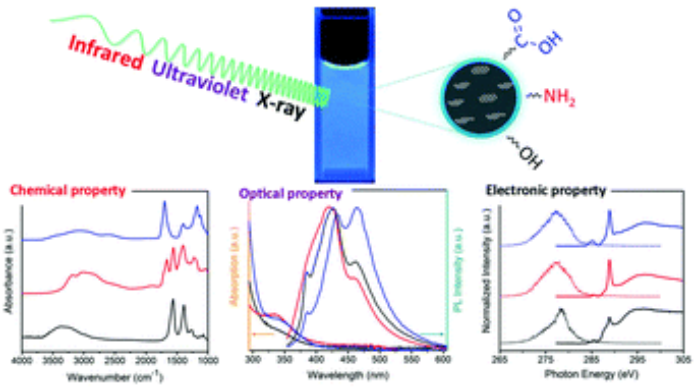

Author Contributions: For this article, AB and **FaWe** provided theoretical simulations for the experimental spectra collected and discussed by the remaining authors. For this purpose, meetings between AB, TP, JR and **FaWe** were held to formulate the relevant goals for the theoretical support. Calculations were performed and analyzed by **FaWe**. The manuscript was written by JR and the discussion of theoretical results was embedded in the manuscript in a jointly manner by JR and **FaWe**.

A.4 | Proton-Coupled Electron-Transfer Dynamics of Water Splitting at N-doped Graphene Oxides

Fabian Weber, Jean Christophe Tremblay, Annika Bande
J. Phys. Chem. C, in review, **2019**

Author Contributions: The project was conceived by AB and **FW** and uses a calculation method provided by JCT. Calculations on the model molecules and electron dynamics were performed by **FW**. The decision on a candidate molecule for the investigation of the proton-coupled electron dynamics was made by AB and **FW**. The classical dynamics calculation for determining the hydrogen-transfer time was carried out by JCT. The program code `detCI@ORBKIT` for the calculation of the electron-dynamics was provided by JCT and has been interfaced to the ORCA program by **FW** and JCT. The manuscript was prepared by **FW** and theoretical and computational details sections concerning `detCI@ORBKIT` were supplemented by JCT. The manuscript was brought into publication form by all authors.

Proton-Coupled Electron-Transfer Dynamics of Water Splitting at N-doped Graphene Oxides

Fabian Weber,[†,¶] Jean Christophe Tremblay,[‡] and Annika Bande[*,†]

†*Department of Locally Sensitive and Time-Resolved Spectroscopy, Helmholtz-Zentrum Berlin für Materialien und Energie GmbH, Hahn-Meitner-Platz 1, 14109 Berlin, Germany*

‡*Laboratoire de Physique et Chimie Théoriques, CNRS/Université de Lorraine – UMR7019, 1 Bd Arago, 57070 Metz, France*

¶*Institute of Chemistry and Biochemistry, Freie Universität Berlin, Arnimallee 22, 14195 Berlin, Germany*

E-mail: annika.bande@helmholtz-berlin.de

Abstract

In this contribution, the proton-coupled electron-transfer process in optimized nitrogen-doped graphene oxide (NGO) model catalysts is studied by means of atomistic simulations. The NGO optimization reveals that especially stabilization of a co-planar water-catalyst complex, as well as electron-withdrawing ketone groups are key features for promoting the initial charge-transfer at excitation wavelengths as low as 341.2 nm. A new model to simulate the dynamics of the overall proton-coupled electron-transfer process in an electron dynamics framework including non-adiabatic decay channels is introduced. Numerical dynamical simulations reveal that an intricate balance between the lifetime associated to vibrational dissipation (i.e. electron-phonon coupling) in the NGO model and the proton-coupled electron-transfer rate determines the overall water-splitting efficiency. December 19, 2019

keywords: molecular modelling, electron dynamics, nitrogen-doped graphene oxide, proton-coupled electron-transfer, water splitting

Introduction

In light of the ever-growing demand for energy generation it has become a central challenge to find more resource-friendly and sustainable ways to generate power. Abstractly speaking, this translates to the goal of finding new processes and materials that generate power using only abundant, non-toxic materials and available sources of energy, while causing only minimal amounts of waste. Although several working prototype methods have been found in the fields of both photovoltaics[1,2] and photochemisty,[3,4,11] none of them can so far compete with current non-sustainable energy generation techniques in terms of power output and production cost. If we therefore additionally desire a comparable efficiency, this adds to the problem the (arguably much harder to fulfil) economic requirements of minimising the costs and time per generated unit of energy while ensuring reliability and accessibility of distribution grids all around the clock.

Considering the possible energy sources, solar energy has become the most extensively studied candidate due to potentially meeting the required output and providing the necessary longevity as a sustainable resource. Although not available at all times to every part of the planet, the solar power of approximately 120 PW[5] hitting our planet could in principle easily cover for the current total energy consumption of roughly 160 PWh[6] per year. One particularly appealing route of harvesting solar energy is via the photochemically driven water splitting reaction, in which sunlight is used for converting water into its components hydrogen and oxygen. Here, the generated hydrogen can be used for producing energy-rich hydrocarbon fuels from carbon compounds[7] similar to an artifical photosynthesis. Since most energy distribution grids in use are based on hydrocarbon combustion, photochemical generation of such fuels therefore offers a most promising way of storing solar energy in a readily useful form that would not require the simultaneous re-design of current power distribution systems.

The formal oxidation and reduction part reactions of the overall water splitting require the transfer of a total of four electrons from water-bound oxygen onto water-bound protons.

Oxidation :	$2\ H_2O$	$\rightarrow$	$O_2\ +\ 4e^-\ +\ 4H^+$
Reduction :	$4H^+\ +\ 4e^-$	$\rightarrow$	$2\ H_2$

However, the requirements for steering this process and the exact interactions between photocatalyst and environment are an ongoing topic of scientific research. The role of the photocatalyst is clearly to promote both the electron-transfer from the water-bound oxygen, as well as the transfer of a water-bound proton. This specific part reaction, which is known as the proton-coupled electron-transfer (PCET)[8,9] has been shown to greatly depend on both a suitable electronic structure for efficient charge separation, as well as the vibration dynamics when considering the transfer of the proton between water and the catalyst. Also, it has been established that this initial activation of the water-catalyst complex is the rate determining step for the overall water splitting, since all following part reactions seem to proceed much faster and without an activation barrier.

Two closely related material classes that are known to undergo this kind of reaction are graphitic carbon-nitrides[10] and nitrogen-doped graphene oxides (NGO).[11] By theoretical studies of the smaller building blocks of carbon-nitride it was found that the nitrogen atoms at the edge of the graphitic sheets act as the proton-accepting units, while the π-network of the carbon-nitride can accept the electron from the water molecule and delocalize it over the molecule.[12,13]

While there are several studies on graphitic carbon-nitrides, the closely related material nitrogen-doped graphene oxide (NGO) has not been studied in a similarly exhaustive way, yet. Although the exact oxygen functionalization pattern is hard to determine,[14,15] there are studies for improving the PCET activity that highlight the importance of binding the dopant nitrogen atoms and functional groups at the edges of the graphitic sheets.[16] This indicates that for NGOs, the PCET mechansim may be working in a similar way as in carbon nitrides.

More interestingly, the effects of the randomized nature of oxygen frunctionalization patterns on its water splitting capabilities are still unclear. To therefore establish a basic understanding for the structure-property relationships in this material class, time-dependent density functional theory (TDDFT) calculations[17] are applied on a large catalogue of differently functionalized NGO model structures to determine their electron-transfer properties. After finding a candidate model that shows a desirable charge transfer state for an absorption in the visible range, we study the PCET dynamics that comprise the first partial step of the water splitting mechanism by applying time-dependent configuration-interaction electron dynamics calculations in the reduced density matrix formulation (ρ-TDCI).[18] Here, thermal vibronic dissipation for the process is included by assuming coupling strengths that reflect different timescales for the fastest possible thermalization time. Additionally, we include coupling hydrogen transfer channels, effectively describing PCET dynamics. This way we can study which order of magnitude for non-adiabatic coupling strengths would be favourable when trying to maximize the PCET rate in an example NGO model.

The article is structured as follows. In section "Procedure and Computational Methods", we give a detailed description of the approaches and theoretical methods used in this work. In the results section, we then show the optimized candidate molecule and explain the structure-property relationships that leads to its performance with respect to excitation (sections "Structural Optimization" and "Relaxed Reaction Path of the Water Dissociation"). Finally, the PCET dynamics are discussed in section "Quantum Dynamics" for different excitation fields and vibronic coupling strengths and the effects of non-adiabatic couplings are discussed.

Procedure and Computational Methods

Optimization of the Model System

To study the photocatalytic water splitting capability of NGO model systems under irradiation with visible light, the first task is to find a reasonably small model system with at least

one charge transfer (CT) state in which an electron is shifted from the water molecule onto the NGO catalyst. Under optimal conditions, the associated excitation wavelength should be close to the maximum intensity of the sunlight emission spectrum at roughly 500 nm,[19] while also showing a high excitation probability, i.e. a high transition dipole moment.

We find such a candidate model system by systematic optimization of the oxygen functionalization pattern on a singly nitrogen-doped, coronene-sized carbon scaffold with one adsorbed water molecule facing the dopant nitrogen atom. This means that several possible locations and types of functionalizations are probed while gradually increasing the oxygen content in the model system. In all these models, the position of the nitrogen atom is kept at the edge position of the candidate structures, since this position has been confirmed as a reasonable reaction site for PCET in other nitrogen-doped molecules.[12,13] To avoid calculation of the complete chemical space of all possible functionalization patterns, a strategy based on rating functions and general chemical intuition was applied when selecting the probed patterns. Naturally, the results and design principles obtained this way will therefore only represent a subset of the overall chemical space of possible configurations.

For determining the CT properties of each candidate structure, *ab-initio* calculations are performed with the ORCA program package.[20,21] In a first step, a density-functional theory (DFT) structure optimization with one water molecule placed close to the NGO-nitrogen is carried out with the CAM-B3LYP functional[22] and the def2-SVP[23] basis set. As further corrections, we utilize Grimme's D3 dispersion correction with Becke-Jones damping[24,25] and add an implicit water environment via the conductor-like polarizable continuum model (CPCM).[28] For speeding up the calculations, the RIJCOSX method[26] is applied in combination with the respective def2-SVP/J auxiliary basis sets.[27]

After geometry optimization, time-dependent density-functional theory (TDDFT) calculations are applied to obtain the properties of the first 100 excited states of the model molecules. These calculations are performed with the same functional and parameters as the geometry optimization, but employ the diffuse def2-SVPD basis set.[29] As has been found

for the graphitic carbon nitrides, the addition of such diffuse basis functions is essential for the correct description of Rydberg-like excited states and the long-distance charge transfer states of water and the NGO molecule.[12]

CT State Characterization and Rating

To choose the best candidate among all probed molecules, a characterization and rating scheme is applied. For this purpose, we first need to quantify the degree to which an excited state describes a charge transfer from water onto the NGO catalyst. For each excited state n, the natural transition orbitals (NTO)[30] are therefore calculated from the respective transition density matrices T^n with elements T^n_{ia}, describing the excitation from the ground state wavefunction Ψ_0 as

$$T^n_{ia} = \sum_\sigma \langle \Psi_n | c^\dagger_{i\sigma} c_{a\sigma} | \Psi_0 \rangle \tag{1}$$

The indices i and a are associated with occupied and virtual molecular orbitals, respectively. Performing a singular value decomposition of the single particle transition density matrices, $T^n = U\Lambda V^\dagger$, yields two orthogonal transformation matrices U and V. These can then be used to construct the excited state in the NTO representation of hole and particle basis wavefunctions ψ^h and ψ^p.

$$\psi^h_j = \sum_i U_{ij}\phi^o_i \qquad \psi^p_j = \sum_i V_{ij}\phi^v_i \tag{2}$$

$$\Psi^h_n = \sum_j \Lambda_{jj}\psi^h_j \qquad \Psi^p_n = \sum_j \Lambda_{jj}\psi^p_n \tag{3}$$

Here, index j runs over all eigenfunctions in the NTO basis and i runs over all occupied (o) and virtual (v) molecular orbitals, respectively. The sum of the respective basis functions with their individual coefficients Λ from the singular value decomposition then yield the total

hole and particle wavefunctions Ψ_n^h and Ψ_n^p for excitation to state n.

To quantify how strongly a CT state transfers one electron from water onto the NGO catalyst, we introduce a metric based on Mulliken projectors. We calculate the hole localization on the water molecule as the expectation value of the hole wavefunction projected onto the atomic basis functions that belong to the water molecule, $\hat{P}_{\mathrm{H_2O}}$. In turn, the particle wavefunction is then projected on all remaining atomic orbitals of the NGO using $\hat{P}_{\mathrm{NGO}} = 1 - \hat{P}_{\mathrm{H_2O}}$, to yield a measure of the particle localization on the NGO. The product of both expectation values yields a measure of the overall CT purity D_n^{CT} of state n that may vary between 0 and 1,

$$D_n^{\mathrm{CT}} = \langle \Psi_n^h | \hat{P}_{\mathrm{H_2O}} | \Psi_n^h \rangle \langle \Psi_n^p | \hat{P}_{\mathrm{NGO}} | \Psi_n^p \rangle \tag{4}$$

This way, a large D_n^{CT} is obtained when the hole is localized on the water molecule and the particle is localized on the NGO model molecule for state n. After identifying the CT states with highest D_n^{CT} among the excited states, each model molecule's water splitting capabilities are rated based on a combination of the excitation energy E_{CT} closest to the sun's emission spectrum, the CT purity D_n^{CT} and the respective transition dipole moments. The rating function F is of the form

$$F = D_n^{\mathrm{CT}} \ \mu_{0n} \ B_\lambda(\lambda_n, T) \tag{5}$$

Here, D_n^{CT} is the CT purity of the energetically lowest lying CT state that shows a purity of at least $D_n^{\mathrm{CT}} > 0.7$ and μ_{0n} is the associated absolute transition dipole moment between ground and excited state. Finally, the function B_λ is the black body radiation intensity at the excitation wavelength λ_n at temperature T

$$B_\lambda(\lambda, T) = \frac{2hc^2}{\lambda^5} \frac{1}{e^{hc/\lambda k_B T} - 1} \tag{6}$$

When using a temperature of 5800 K, one qualitatively obtains the spectral intensity

distribution of sunlight.[19] Consequently, the rating function F assumes large values for pure CT states that have high transition dipole moments and a favourable excitation energy with respect to the sunlight spectrum.

Dissipative Many-Electron Dynamics

For the most promising model molecule, an analysis of the many-electron dynamics is performed to understand the timescales of electronic excitation and hydrogen transfer processes in NGO catalysts. The separate reaction channels with their respective rates Γ relevant for the PCET dynamics simulation are schematically depicted in figure 1.

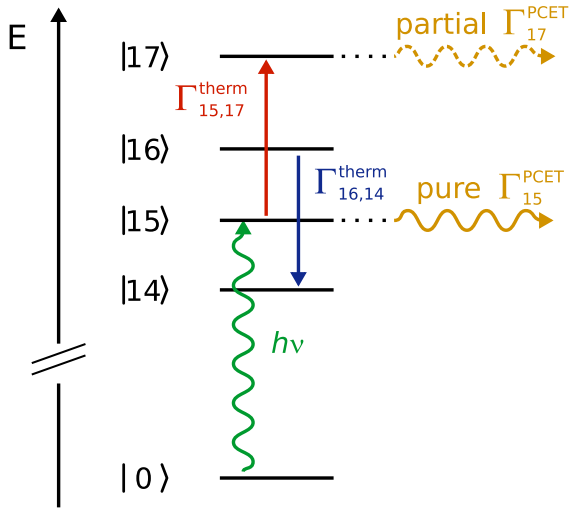

Figure 1: Schematic depiction of the reaction channels related to the PCET dynamics between electronic states $|n\rangle$. The green wavy line ($h\nu$) depicts the external field excitation. Straight vertical lines are thermal (de)excitation in blue and red, respectively. The proton-coupled electron-transfer processes (yellow) lead away horizontally from the ground state geometry. The rate of hydrogen-transfer is modulated by the charge transfer purity D_n^{CT} (see section "Hydrogen Transfer Rate"), leading to lower rates for partial charge transfer (dashed yellow) than for pure charge transfer states.

Firstly, the initial vertical excitation is driven by an external field (shown in fig. 1 with a green wavy arrow) that excites the ground state $|0\rangle$ to a mixture of excited states $|n\rangle$. These states in turn may then horizontally leave the system via PCET channels (yellow wavy arrows) that are a combination of the inverse hydrogen transfer time and the purity D_n^{CT} of

the respective CT state (see equation 12 below). Finally, all states may exchange population via thermalization (red and blue arrows). These thermalization channels allow excited states without an PCET channel to undergo a secondary PCET process via exchanging population with PCET-active states. The details of how we obtain these rates, as well as how to drive the quantum dynamics calculation with implicit vibration-induced relaxation and hydrogen-transfer will be summarized below.

Time-dependent Configuration Interaction Theory

Dissipative electron dynamics is studied here by means of the time-dependent configuration interaction method[31–33] in its reduced density matrix formulation (ρ-TDCI).[18] Formally, a basis of many-electron pseudo-eigenstates is used to represent the reduced density matrix (RDM) of the N-electron system as

$$\hat{\rho}(t) = \sum_{mn} \rho mn(t) |\psi_m\rangle\langle\psi_n| \tag{7}$$

The many-electron pseudo-eigenstates are computed from time-dependent density functional theory (TDDFT) and approximated as linear combinations of singly-excited configuration state functions, $|\Phi_a^r\rangle$,

$$|\psi_n\rangle = A_0\Phi_0 + \sum_{ar} A_a^r |\Phi_a^r\rangle \tag{8}$$

In the present work, the coefficients A_a^r for the excitation from an occupied orbital a to a virtual orbital r are obtained by re-orthonormalizing the many-body pseudo-eigenstates from a TDDFT calculation at the optimal ground state geometry of the system. This hybrid TDDFT/CI formalism was shown to provide good energetics in similar charge transfer systems while retaining the computational scaling of the configuration interaction singles method.[34–36]

The RDM evolves according to the Liouville von Neumann equation

$$\frac{\partial\hat{\rho}(t)}{\partial t} = -\frac{i}{\hbar}\left[\hat{H}_{el},\hat{\rho}(t)\right] - \frac{1}{\hbar}\left[\hat{W},\hat{\rho}(t)\right]_{+} + \frac{i}{\hbar}\left[\vec{\hat{\mu}}\cdot\vec{F}(t),\hat{\rho}(t)\right] + \hat{\hat{\mathcal{L}}}_D\hat{\rho}(t) \tag{9}$$

where $\hat{H}_{el}$ is the Hamiltonian of the N-electron system, and the third term on the right-hand-side represents the coupling of the molecular dipole $\vec{\hat{\mu}}$ with a time-dependent external field $\vec{F}(t)$. The second term involves the anti-commutator over an absorbing potential which mimics the loss-of-norm due to hydrogen transfer, as will be discussed below. Assuming Markovian interaction with the environment, the dissipative Liouvillian super-operator in its Linblad form reads

$$\mathcal{L}_D\hat{\rho}(t) = \sum_{mn}\frac{\Gamma_{mn}}{2}\Big(\big[\hat{C}_{mn},\hat{\rho}(t)\hat{C}^{\dagger}_{mn}\big] + \big[\hat{C}_{mn}\hat{\rho}(t),\hat{C}^{\dagger}_{mn}\big]\Big) \tag{10}$$

where $\hat{C}_{mn} = |\psi_n\rangle\langle\psi_m|$ are so-called Lindblad operators that mediate the transfer from state ψ_m to ψ_n at a rate $\Gamma^{\text{therm}}_{mn}$, introduced in the next subsection. Using ansatz (7) for the RDM leads to linear equations of motions that can be integrated numerically using a pre-conditioned adaptive step-size Runge-Kutta algorithm,[37] as implemented in GLOCT.[18,38] All matrix elements required for propagating the RDM are computed from the pseudo-eigenstates, Eq. (8), using the open-source post-processing program package ORBKIT.[36,39,40] To model the behaviour of isotropic orientation in solution, all results are averaged over excitations using pulses polarized along the three cardinal directions $\{x, y, z\}$.

Vibration-induced Energy Relaxation

Non-adiabatic coupling to the system vibrations leads to energy relaxation and thermalization among the many-electron states used to represent the RDM. By using first-order time-dependent perturbation theory it was shown that energy relaxation induced by electron-vibration coupling approximately scales as the inverse of the square of the energy difference between two electronic states.[41] Here, the non-adiabatic relaxation rate Γ_{mn} between electronic states m and n is computed as the sum of the individual contributions of each vibra-

tional mode q, subject to Lorentzian broadening

$$\Gamma_{mn}^{\text{therm}} = \gamma \sum_q \left| \frac{(\gamma/2)^2}{(\Delta E_{mn} - \hbar\omega_q)^2 + (\gamma/2)^2} \right| \text{ , with } E_m > E_n \tag{11}$$

The upward rates are obtained by detailed balance, $\Gamma_{nm}^{\text{therm}} = e^{E_{mn}/K_b T \Gamma_{mn}}$. These are required, since we consider the system at finite the temperature $T = 300$ K. The normal mode frequencies ω_q are obtained from numerical vibrational analysis of the NGO candidate molecule at the ground state geometry, while the ΔE_{mn} are the associated electronic energy differences from the excited states at the same geometry. The parameter γ is introduced as a measure for the maximum possible relaxation rate from state n to m via non-adiabatic coupling, and its effect on the many-electron dynamics will be discussed below. Additionally, the parameter is directly related to a relaxation lifetime via the Lorentzian width.

Hydrogen Transfer Rate

Provided the molecule is electronically excited to a CT state, the water molecule is expected to fragment into a hydroxyl radical and a hydrogen atom that is transferred to the NGO catalyst. This hydrogen transfer from water to NGO is expected to strongly impact the laser excitation dynamics and compete with vibronic relaxation induced by non-adiabatic coupling (i.e. thermalization). To provide a combined picture of electronic excitation and hydrogen transfer dynamics, we introduce in Eq. (9) a negative imaginary potential of the form

$$\hat{W} = \sum_n \Gamma_n^{\text{PCET}} |\Psi_n\rangle\langle\Psi_n| = \sum_n \frac{D_n^{\text{CT}}}{\tau_n^{\text{HT}}} |\Psi_n\rangle\langle\Psi_n| \tag{12}$$

where τ_n^{HT} is the duration associated with the hydrogen transfer process. The role of this imaginary potential is to absorb the outgoing flux of hydrogen, which ultimately reduces the overall norm of the wavefunction. Assuming that the reaction is completely irreversible, the loss of norm yields a measure for the rate of combined electron and hydrogen transfer

dynamics - i.e. the PCET process. Since the desired final product is an uncharged hydroxyl and NGO+H complex that can only be obtained from an equally strong proton and electron transfer (i.e. the pure charge transfer case of $D_n^{\mathrm{CT}} = 1$), the rate at which a given state n is annihilated, $1/\tau_n^{\mathrm{HT}}$, is modulated by its CT character D_n^{CT}, obtained from the previous NTO analysis (see Eq. (4)). This will be discussed in more detail in the results section.

We estimate the decay time τ^{HT} from the vibrational period of the atom on the lowest-lying charge transfer state with the highest D_n^{CT}. A relaxed reaction path (RRP) for the water splitting reaction of the candidate NGO system is first constructed by performing constrained structure optimizations of the ground state DFT level (cf. section "Relaxed Reaction Path of the Water Dissociation") where the O-H bond of the water molecule facing the nitrogen is constrained to different lengths. Subsequent TDDFT calculations at each of these geometries yield potential energy curves of multiple electronically excited states along the reaction coordinate. The first pure CT state, identified by following the energetically lowest lying state with the largest D_n^{CT} along the RRP, is then fitted to a harmonic potential centered at proton transfer geometry. We define the decay time for the hydrogen transfer τ_n^{HT} as the time required for the hydrogen atom (mass $M = 1.00797$ a.m.u.) to decay towards the minimum of the pure CT state, starting from the pure CT state in the ground state geometry. Throughout all subsequent electron dynamics simulations, the hydrogen transfer time estimate of $\tau_n^{\mathrm{HT}} = 7\,\mathrm{fs}$ is used.

Results and Discussion

Structural Optimization

The NGO model molecule developed in this study is obtained after five stages of successive functional group addition to the N-doped coronene base structure (total number of 158 model structures, see ESI for more information). The excitation properties of the most suitable candidate at each stage are collected in table 1 and figure 2 shows which structural features

were added at each stage. The final candidate NGO model shows an extended π-conjugated network that contains two ketone groups (stages one and two), as well as one carboxyl group (stage three). This special arrangement allows the water molecule to be hydrogen-bonded in co-planar fashion to both one of the carboxyl oxygen atoms as well as the ketone oxygen added in stage one. Further, the electron withdrawing effects of the oxygen atoms overall facilitate the transfer of a p-electron from the water molecule to the π-system of the NGO molecule, effectively red-shifting the excitation wavelength for the pure CT state from 186.3 nm in the unfunctionalized pristine case to 341.2 nm in the proposed candidate NGO model (compare table 1).

By addition of the epoxy group to the model molecule at stage four, the excitation wavelength is again red-shifted, while however strongly lowering the transition dipole moment. Therefore, although the phenol group of stage five slightly blue-shifts the excitation wavelength and lowers the charge transfer purity D_n^{CT} for the pure CT state, it causes a much better transition dipole moment again - which is why this last modification still provides an improvement. It shall also be noted that the introduction of hydroxyl groups saturating a π-bond with -OH and -H generally leads to a blue-shift of the excitation wavelength for almost all probed cases. Since a blue-shift of the excitation energy will lead away from the optimum of 500 nm, this indicates hydroxyl groups are unfavourable for optimising the electron-transfer properties.

Among the first 100 excited states of the final candidate molecule, only the two states number 15 and 80 (numbering according to the ORCA[20] output) qualify as pure charge transfer states with D_n^{CT} of at least 0.70. Besides these two, there exist ten additional states with D_n^{CT} values of at least 0.10, which shall be referred to as partial CT states in the following.

The hole and particle NTO wavefunctions (cf. equation 2) that describe the pair of energetically lowest-lying partial and pure CT states are shown in figure 3. From these NTO wavefunctions one can see that the hole wavefunction of the partial CT state 14 is

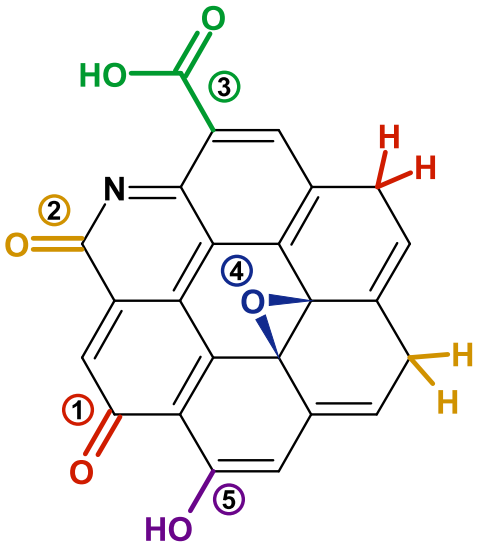

Figure 2: Development of the final candidate molecule. Numbers and colors indicate what changes were introduced in which stage.

also localized on the NGO catalyst's carboxyl group, while the pure CT state 15 shows an almost exlcusive localization on the water molecule. Note that the numbering of states according to ORCA[20] is not necessarily ordered energetically. The particle wavefunctions of both pure and partial CT states are essentially identical and spread over the π-conjugated ketone groups and adjacent pristine C atoms. This analysis of the electronic structure in terms of energies and densities has already several implications for the molecular design principles of efficient NGO catalysts. Firstly, it shows that the charge transfer to the NGO can be facilitated by adding electron-withdrawing substituents to the π-system, because it lowers the energy of the particle wavefunction. However, due to the particle wavefunctions being so similar for partial and pure CT states, such adjustments result in a red-shift for the excitation wavelength of both the partial as well as pure CT states in comparable magnitude.

Secondly, since the hole wavefunction is the only substantial difference between the partial and pure CT state's NTOs, the only way of favouring a pure CT over partial CT is to disfavour the partial CT state's hole wavefunction. In the proposed final candidate structure (as shown in figures 2 and 3), this is achieved by a push-pull asymmetry introduced with the carboxyl group, relative to the ketones. While the carboxyl group is electron-rich, it is

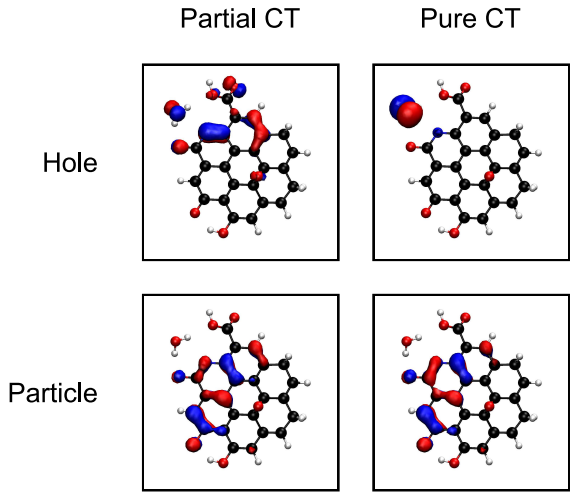

Figure 3: Hole and particle wavefunction of the energetically lowest-lying partial CT state 14 and pure CT state 15 in a contour plot with a cutoff of ±0.05.

Table 1: Charge transfer characteristics of the different generations of NGO model molecules. Numbers in parentheses reflect states that come closest to the pure/partial state description, while missing the requirement of $D_n^{\mathrm{CT}} > 0.70$ and $D_n^{\mathrm{CT}} > 0.10$, respectively.

Development Stage	**exc. wavelength pure/part. [nm]**	D_n^{CT} **pure/part.**	$\lvert\vec{\mu_{0n}}\rvert^2$ **pure/part. [au]**
Pristine	186.3 / 170.5	0.75 / 0.18	1.18 / 2.07
Stage 1	(238.7) / (298.9)	(0.66) / (0.08)	(0.01) / (0.01)
Stage 2	(270.1) / 263.3	(0.38) / 0.22	(0.001) / 0.08
Stage 3	329.0 / (306.6)	0.89 / (0.03)	0.05 / (0.04)
Stage 4	344.4 / (310.0)	0.93 / (0.02)	0.03 / (0.02)
Stage 5	341.2 / 276.6	0.89 / 0.14	0.08 / 0.39

also electrophilic, thus disfavouring the formation of a hole in this region. This is reflected by the large drop in D_n^{CT} of the lowest partial CT state from stage two to three (see table 1).

Finally, it shall be noted that the arrangement of the water molecule with respect to the NGO seems to be important for the CT process. While the water molecule is rather randomly oriented with respect to the O-H-N bond in the first stages of the candidate development, all of the 16 structures of the last functionalization stage only feature a co-planar arrangement and two O-H-O hydrogen bonds instead.

Relaxed Reaction Path of the Water Dissociation

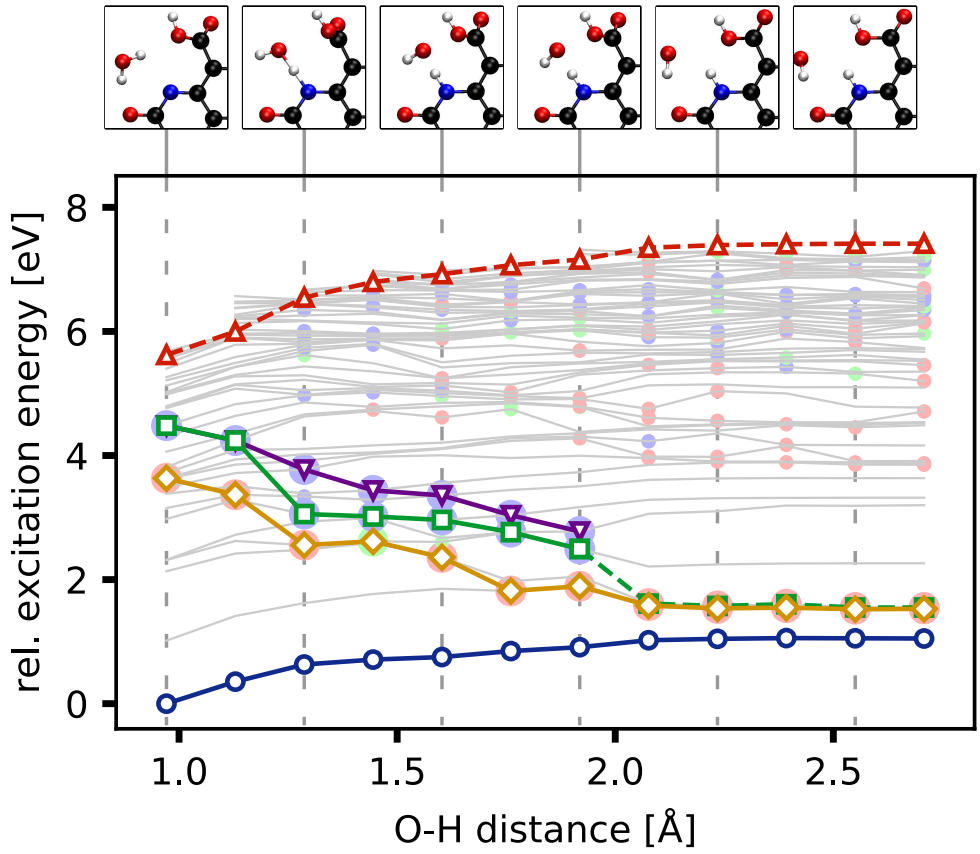

Figure 4: Relative energies of the electronic ground state (blue circles), lowest-energy pure CT (yellow diamonds) and partial CT states (green squares and violet downwards triangles) and the ionization limit (red upwards triangles) as function of the O-H bond distance. Additionally, the adiabatic states are shown in the background according to their energetic ordering at each geometry with gray thin lines. Colored dots highlight states of pure ($D_n^{\mathrm{CT}} > 0.7$, red), intermediate partial ($0.7 > D_n^{\mathrm{CT}} > 0.5$, green) and partial CT character ($0.5 > D_n^{\mathrm{CT}} > 0.1$, blue) The NGO+H active site geometries are displayed in the upper panels at selected distances.

The RRP was obtained by a constrained geometry optimization of the NGO water complex, where the O-H bond closer to the NGO nitrogen was elongated in sequential steps. The upper panels of figure 4 show cutouts of the molecular structures featuring the elongation of the O-H bond that eventually leads to the formation of an N-H bond between the NGO and the former water-proton. The proton transfer is accompanied by a rotation of the carboxyl group around the distance of 1.4 Å, such that the repulsion by the free electron pairs of the

water-oxygen is minimized. In the lower panel of figure 4, the relative energies of the ground state (blue circles), as well as the energetically lowest lying partial and pure CT states (green squares and yellow diamonds, respectively) are given along the relaxed reaction path (i.e. O-H distances). Note that state numbers may change between geometries due to state crossings or changes in CT character. Consequently, only the energetically lowest-lying pure as well as a pair of partial CT states are highlighted by following the dominant charge transfer numbers at each of the geometries. Further, the CT states are labelled at each geometries according to their strength, separated in pure CT ($D_n^{\mathrm{CT}} > 0.7$, red), intermediate partial CT ($0.7 > D_n^{\mathrm{CT}} > 0.5$, green), and weak partial CT ($0.5 > D_n^{\mathrm{CT}} > 0.1$, blue). Finally, the ionization limit (red triangles) is estimated from the cation energy at the same geometry.
As one can see, the dissociation of the O-H bond is energetically unfavourable in the electronic ground state (blue circles) since the energy increases along the reaction coordinate. For the pure and partial CT states (yellow diamonds and green squares/violet triangles, respectively) the dissociation is favourable, thus confirming the general possibility of driving the PCET reaction after excitation into such states. The dynamical behaviour in the partial and pure CT states is nonetheless expected to be different. At a distance approaching 1.3 Å, the hydrogen atom becomes shared between the nitrogen atom of the NGO and the OH fragment. This leads to a mixing of the state characters, as seen from the reduction of the CT purity D_n^{CT}. The partial CT character is also spread over many states, bracketed by the green and violet lines. This strong character mixing implies that hopping between these states will occur rapidly, leading to an overall return of the hydrogen towards the original NGO+water conformation. This can be inferred from the behaviour of the adiabatic potential energy curves in grey, that all favor this conformation. On the contrary, the pure CT state has little overlap with all other states in this energy window due to its very different character. The branching ratio for dynamics in this state will thus be strongly biased towards the hydrogen transfer, as coupling to the states favoring the original NGO+water conformation is weak. This branching ratio can be included in the dynamics by modulating the PCET

rate according to the degree of charge transfer D_n^{CT}, as described in the theory section.

For distances larger than 1.92 Å, the partial (dashed line) and pure CT states energies become almost identical. This energy convergence towards the pure CT state is caused by the partial CT states splitting, with one adopting a pure CT character beyond this distance. The reason for this can be understood from the changes in the bonding situation: While the pure CT related electron originates from the p orbital perpendicular to the H-O-H plane (cf. figure 3), the in-plane p orbitals are used for forming the O-H bonds. For longer O-H distances, however, one of the in-plane p orbitals is now available for donating an electron to the NGO catalyst molecule, as well. This behaviour can be confirmed by analyzing the D_n^{CT} values at the different distances for both the pure and partial CT states (see figure 5a)). Here, one finds that for larger distances the partial CT states D_n^{CT} values (green squares) approach the pure CT state beyond a distance of 2.0 Å. Additionally, there is a local minimum in the pure CT and local maximum in the partial CT states' D_n^{CT} close to an O-H distance of 1.5 Å, which is indicative of either a local avoided crossing or a conical intersection between the potential energy surfaces of partial and pure CT states around that distance.

Since the ground and CT states become energetically close for large O-H distances, there is in principle a possibility for either of the states to return to the ground state potential energy surface and thus towards the undesired initial reactand geometry. When analyzing the absolute transition dipole moment $|\mu_{0n}|^2$ for the partial and pure CT states in figure 5b), however, one notes that with increasing distances, it becomes smaller and smaller, making a return to the ground state potential surface less likely. Finally, we indirectly confirm the biradical final product at approximately 2.6 Å by analyzing the Mulliken charge of the fragments of the electronic ground state (figure 5c)). The fragments were chosen such, that the oxygen and hydrogen of the former water molecule build up one fragment (OH), and the NGO molecule and the transferred hydrogen build up the other (NGO+H). Since the OH fragment (red triangles) shows a negative charge and the NGO+H complex (blue circles) a positive one at the largest separation, the charge transfer states that purely transfer one

electron from the OH fragment onto the NGO+H complex need to be charge-neutral on each fragment.

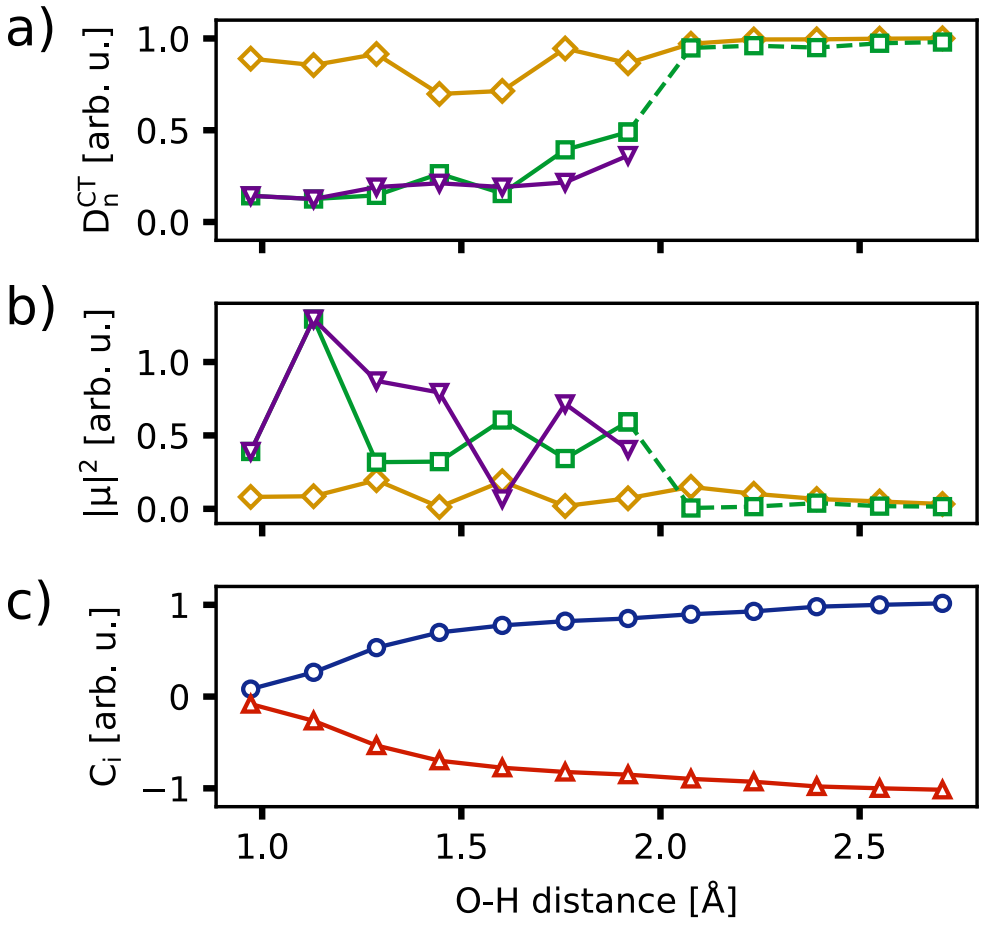

Figure 5: D_n^{CT} values (a) and magnitude of the transition dipole moments $|\mu_{0n}|^2$ (b) for transition from ground state into the pure (yellow diamonds) and partial CT states (green squares and purple triangles) at different OH bond lengths. Panel (c): Partial Mulliken charges C_i on the NGO+H fragment (blue circles) and OH fragment (red triangles) are given for the electronic ground state.

Quantum Dynamics

The quantum dynamics for the PCET step of the water splitting reaction can be treated in an explicit electron dynamics framework with implicit nuclear dynamics implemented through the hydrogen transfer rate $\frac{1}{\tau_n^{\mathrm{HT}}}$ as introduced in section "Dissipative Many-Electron Electron Dynamics". In the following, we shall split the discussion of our findings into one

section for the dynamics during the initial excitation pulse and one section for the dynamics after the pulse. In all cases, the state populations shown below are an average for three individual excitation dynamics with linearly x, y and z polarized external fields. This way, the behaviour of an isotropic arrangement of NGO-water complexes is obtained.

To test the behaviour of the NGO-water complex for various excitations, different parametrizations for both the external field as well as the non-adiabatic thermalization rate γ are used. For the external field, the numbers chosen mimic readily available laboratory lasers. We probe three different pulse lengths t_s (25, 50 and 100 fs) and two different amplitudes (0.001 au and 0.01 au). Since the amplitudes translate to relatively weak peak intensities of 3.51×10^{12} and 3.51×10^{13} W/cm^2, respectively, we do not expect that ionization with respect to multi-photon processes play a role for the dynamics. The frequency of the carrier pulse is fixed to 0.134 au (341.2 nm), which corresponds to the excitation energy of the lowest lying pure CT state (see Table 1).

The thermalization rates γ, were chosen such that the minimal thermalization time $\tau_\gamma = \frac{1}{\gamma}$ of each individual vibration channel corresponds to 10, 1 and 0.1 ps, respectively. These translate to testing cases of weak, intermediate, and strong non-adiabatic coupling between the electronic states with respect to molecular vibrations. In all cases, the propagation after the laser pulse was continued until the respective thermalization time τ_γ.

Initial Excitation Dynamics

In the following, the simulations for using a pulse length of 50 fs shall be discussed in detail. The results of other laser set-ups may be taken from table S.II in the electronic supplementary material. To understand the trends for the dynamics during the external field excitation for different PCET scenarios, we discuss the left halves of figures 6a-f). Here, panels a-c) correspond to the external field amplitude with 3.51×10^{12} W/cm^2 peak intensity (shown in the background in light gray), while panels d-f) reflect scenarios with 3.51×10^{13} W/cm^2 peak intensity. Each panel contains information about the time-dependent norm

(black), ground state population (blue) as well as the sum over all pure and partial CT state populations (orange and green, respectively). Additionally, the sum of excited states that cannot decay via hydrogen transfer (furthermore called "non-CT states" with $D_n^{\mathrm{CT}} < 0.1$) is given as a dashed gray line. Note that the populations of partial and pure CT states were scaled for better readability. The panels of each column differ by their thermalization times that can be found in the lower left corner of each panel.

From panels a-c one can see that in the initial excitation period of 50 fs the norm stays virtually the same for all values of τ_γ, while the ground state populations decrease in a similar fashion in all three cases by about 13%. The lost ground state population is almost exclusively transferred to non-CT states in all three cases (note the scaling by a factor 1000 for the CT states). This shows that during excitation using a weak pulse, no norm-reducing PCET occurs, although the excitation frequency is tuned resonant with the lowest lying pure CT state. The reasons are twofold: First, the imaginary potential term associated with each partial and pure CT state (cf. equation 12) effectively changes the energetic resonance condition for the laser excitation, thus leading to a lowered transition probability in general. Second, due to the ultrafast hydrogen transfer rates ($\frac{1}{7\mathrm{fs}} = 0.14\mathrm{fs}^{-1}$), population of these states would be immediately removed, leading to an immediate decrease in the wavepacket norm. The ultrafast hydrogen transfer rate also has the nefarious effect of inducing dephasing between the ground and CT states on the same femtosecond timescale. As the initial and final states lose their coherence due to this dephasing, population transfer via coherent laser interaction with light becomes almost impossible. The inefficiency of the excitation process can be overcome by a stronger perturbation of the system. Therefore, it is only around the laser field peak intensity, when the excitation probability bebcomes higher than the PCET rate, that population of pure CT states can be observed.

When focusing on the populations of the partial CT states, one sees that the cases of weak and intermediate vibronic coupling (panels a) and b), respectively) strongly differ from the case of strong vibronic coupling (panel c)). While the populations stop increasing

after the maximum laser amplitude for a) and b), it continues growing over a much longer time and to a higher overall value for scenario c). The reason for this difference is most likely connected to the different thermalization rates between states compared to the PCET rates of the partial CT states: In scenarios a) and b) the fastest thermalization rates are of the order of $\Gamma_{mn} = 0.1\text{ps}^{-1}$, which is relatively slow compared to the partial PCET rates $\frac{D_n^{\text{CT}}}{\tau^{\text{HT}}} = \frac{0.1}{7fs} = 0.014\text{fs}^{-1}$. Therefore, after the population via the laser becomes slower than the PCET rate, the partial CT populations start to monotonously decrease. In case of strong vibronic coupling, however, the fastest thermalization rates between states are of the order of magnitude 0.01fs^{-1}, therefore potentially competing with some of the partial CT channels.

When using lasers with higher peak intensities, d-f), one can see a much more pronounced depopulation of the ground state to approximately 0.4, associated with an immediate loss of norm. However, due to fast decoherence between the ground and CT states as discussed above, most of the excited population is still transferred to non-CT states. As was the case for weaker intensity pulses, the three regimes of vibronic coupling strengths show no strong differences in the behaviour of the norm, the ground state, and the non-CT populations.

Although the partial and pure CT state populations are overall much higher compared to excitations with weak laser fields, the three cases behave similar to each other with respect to these PCET-active states. Again, one notices that the partial CT state population in Fig. 6f) is much higher for short thermalization times (note the different scaling factor for the green and orange curves). However, one also notices that the pure CT states show a different behaviour for the strong vibronic coupling case, since its peak population is even less than half of the peak population in the other two coupling regimes. The reason for this may be that the PCET rates become comparable to that of the thermalization. Since it is hard to see from the panels a-c), this behaviour cannot be confirmed for the weaker external field.

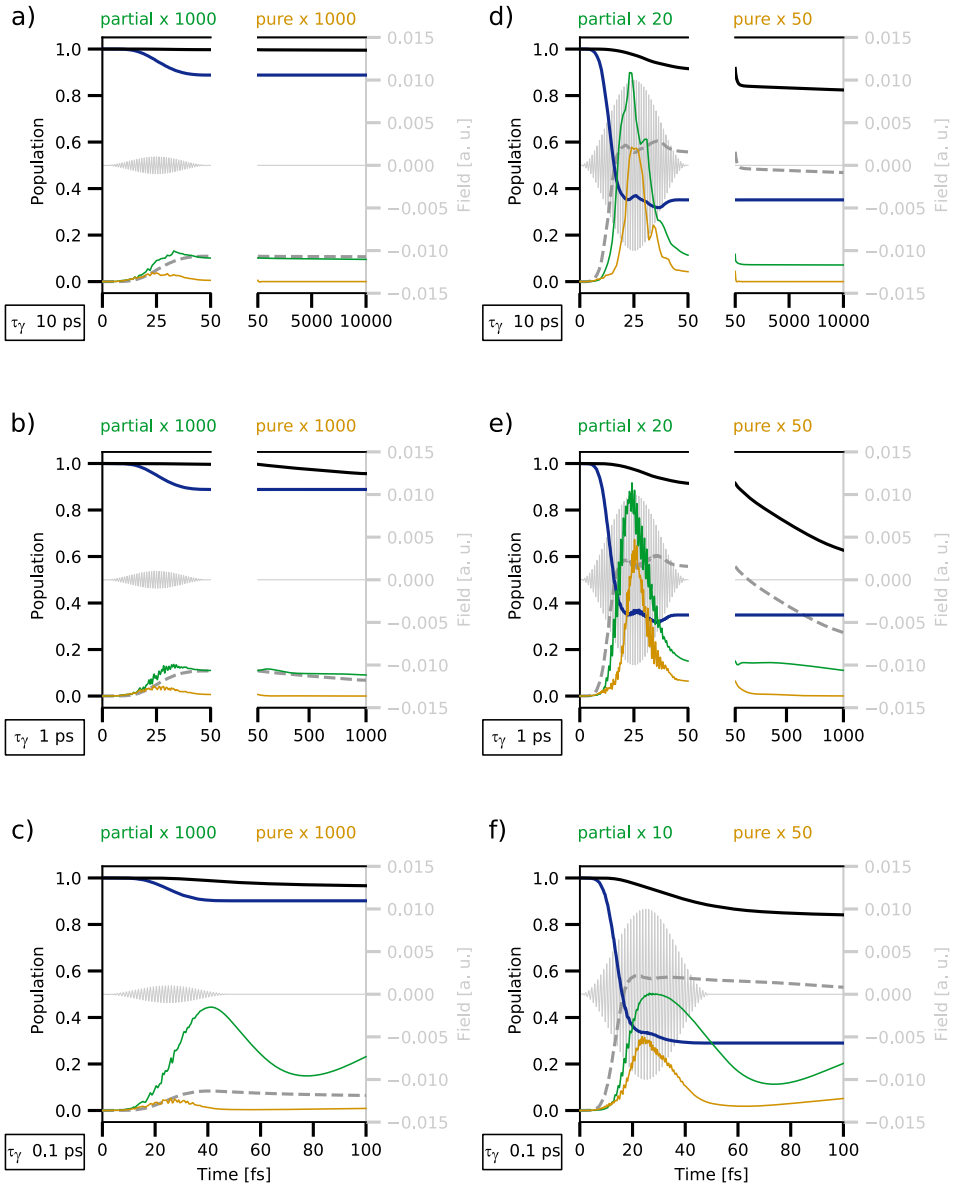

Figure 6: Model PCET dynamics for excitation with different external field amplitudes and thermalization times τ_γ. Shown are the norm (black), ground state (blue) as well as the sums of all pure CT states (orange) and partial CT states (green) as a function of time. The external field is shown in light grey with respect to the second y-axis. The sums of pure and partial states were scaled for better readability as indicated above the panels. Note, that some pictures have been split into an excitation period and post-excitation period.

Thermalization Dynamics

Next, we focus on the dynamics after the laser excitation for the scenarios depicted in the right halves of figures 6a-f). First, one notices that regardless of the thermalization

parameter, the ground state population does not change with time in any of the scenarios. The reason is that the energetic difference between the ground and excited states is too large to be overcome for any of the probed vibronic coupling strengths. While the transfer rates between ground and excited states are indeed finite and non-vanishing, they tend to be of the orders of $\approx 10^{-12}$ fs^{-1} (i.e. 1 s^{-1}) and are therefore not noticeable on the probed timescales.

When focusing on the cases of lasers with low peak intensities a-c), one finds that for the weak and intermediate vibronic coupling strengths (panels a) and b)), the partial and pure CT state populations stay virtually constant as well. While the pure CT states start off the thermalization dynamics with virtually zero population, the partial CT states are re-populated through thermalization at a similar rate as their PCET decay. Eventually, for very high thermalization rates, scenario c) even shows an increase of the partial CT states population close to the end of the propagation. This can be explained by the thermalization rates that become competitive with the PCET rates.

When turning to the thermalization-induced norm loss, we note that for $\tau_\gamma = 1$ ps (panels b) and e)), the norm loss is the highest. We further notice that it is almost the same as the decrease in the sum of all non-CT states, indicating that the losses are caused by secondary processes – i.e. non-PCET states populating partial or pure CT states, that may then decay through the hydrogen transfer channel (see section "Dissipative Many-Electron Electron Dynamics").

The same behaviour for both the state populations as well as the norm loss can be found for the higher amplitude excitation scenarios d-f), albeit in a much more pronounced fashion. Especially for the intermediate vibronic coupling scenario shown in panel e), the final norm is at 0.63 – indicating that almost half of the NGO-water complexes have initiated a PCET process after the simulation time of 1 ps. Again, a high efficiency of the secondary PCET for the non-CT states can be observed.

Since neither the partial nor the pure CT state populations change drastically, it is reasonable to assume that the important thermalization processes leading to the secondary

PCET are of the same order of magnitude as their connected PCET channels. Also, since the faster hydrogen transfer time for a pure CT state is 7 fs while the shortest possible thermalization time is of the order of 1 ps for this case, one would expect that the secondary decay channels causing the norm loss need to be connected to "non-CT $\rightarrow$ weak partial CT $\rightarrow$ hydrogen transfer" processes rather than to pure CT states when following the same timescale difference argument as discussed for the excitation dynamics.

To prove this hypothesis, the thermalization rates for the most prominent excited non-CT states are compared with the rates of their respective target PCET channels. To find which states are the most prominent, a series of thermalization dynamics with initial population in each of the individual excited non-CT state is performed. This allows to extract the state-specific norm losses originating from thermalization processes. Weighting each state-specific norm loss with the state populations at the end of the laser pulse in the actual dynamics, the non-CT states can be sorted according to their importance for the secondary PCET.

Fig. 7 depicts the detail of the thermalization dynamics for scenario e). The bold gray dashed line represents the sum of all non-CT states that decrease at almost identical rate than the overall norm (black line). When taking the seven non-CT states with the highest importance for the secondary PCET (thin colored lines), one may decompose the gray line further into the sum of important (dashed blue line) and unimportant non-CT states (dashed red line). The blue dashed line again decreases similarly to the gray one while the red dashed line follows a slower decay. This is indicative that the excited non-CT states with higher secondary PCET efficiency are responsible for the observed norm loss. Note that the blue line converges monotonically to the gray dashed line when including more partial contributions.

Analyzing individual thermalization rates $\Gamma_{mn}^{\mathrm{therm}}$ (cf. equation 11) of the seven dominant states m towards all other states n, one recognizes that the timescales for thermalization and hydrogen transfer processes are of similar magnitude in some cases. In particular, states 7, 58, 63, and 64 have PCET rates of a few picoseconds, comparable with the thermalization regime $\tau_\gamma = 1\mathrm{ps}$. However, these states have almost no initial population and therefore

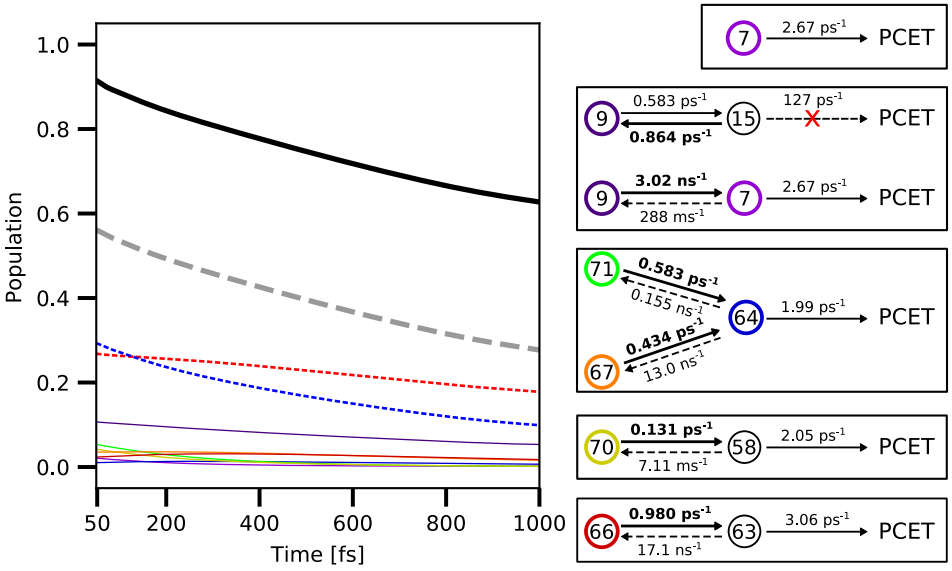

Figure 7: Left panel: Detailed thermalization dynamics for τ_γ=1 ps and peak intensity 3.51 10^{13} W/cm^2 (as in figure 6e)). The bold black line represents the norm of the wavefunction, and the gray dashed line represents the sum of all non-CT states. The thin solid lines represent the seven most important non-CT states that decay via secondary processes. The thin dashed blue and red lines give the sum of these seven states and all remaining non-CT states, respectively. Right panel: Secondary hydrogen transfer channels of the seven most important non-CT states. Circled numbers refer to the n-th electronic state, numbers above the arrows reflect the individual thermalization/PCET rates. The bold circles are color-coded as the populations in the left panel.

do not strongly contribute to the decay in a direct PCET process. They are, however, suitable for *indirect* PCET decay via secondary thermalization from neighbouring excited non-CT states. After the pulse of 50 fs duration, direct PCET has contributed to the depopulation of the short-lived CT states and only partial CT-states remain populated. The dominant contributions stem from states 9, 66, 67, 71, and 72 in the case presented in Fig. 7. The equilibrium for these states is strongly biased towards states 7, 58, 63, and 64, which present a thermal stability comparable to their PCET rates. Consequently, PCET and further thermalization become competitive, which explains why this specific choice of pulse duration and thermalization rate leads to the highest light-to-proton transfer efficiency, as documented by the largest overall loss-of-norm after thermalization. In general, these considerations explain why both lower or higher thermalization times τ_γ potentially lead to

less secondary thermalization norm loss. For $\tau_\gamma = 10$ ps, the thermalization rates become too slow compared to even the lowest hydrogen transfer rates, and the populations remain trapped in the states or slowly return to the global ground state. On the other hand, for a lower $\tau_\gamma = 0.1$ ps, thermalization becomes too fast and dominates PCET, while reducing the excitation probability by increasing the dephasing rate.

It can be inferred from these simulations that the efficiency of the PCET process can be enhanced by optimizing the non-adiabatic couplings of the electron dynamics to the NGO phonons, such as to maximize the relative importance of the secondary PCET process induced by thermalization.

Conclusion

In this work we provide a detailed discussion of the proton-coupled electron-transfer (PCET) dynamics for the water splitting by as nitrogen-doped graphene oxide (NGO) model molecule. In a first step, we determine important functionalization patterns that facilitate the initial charge transfer (CT) step from water onto NGO. It is observed that a π-conjugated network of electron-withdrawing groups is important for stabilising the particle wavefunction on the NGO catalyst such that the excitation wavelength shifts form the ultraviolet regime towards the visible light spectrum. Additionally, a co-planar arrangement of the water molecule is found to be important for lowering the excitation energy further.

Using an optimized model containing all important molecular features for the charge transfer state, the dissociative nature of the charge transfer states is confirmed by calculating the reaction pathway for the hydrogen transfer reaction. The dissipative many-electron dynamics of the proton-coupled electron-transfer is studied by means of the time-dependent configuration interaction in its reduced density matrix variant (ρ-TDCI). The coupling of the electron dynamics to the phonons of the NGO model is computed from normal mode analysis and using a phenomenological scaling constant that determines the thermalization

timescale in the system. The vibrational lifetime of the pure charge transfer state, which is found to be ~ 7 fs, is used to define a hydrogen transfer rate. It enters the dynamics as a loss-of-norm channel, which quantifies the efficiency of the hydrogen transfer process. The computational setup allows simulating laser excitations of a water NGO complex at finite temperatures, as well as the PCET and thermalization dynamics, to determine their relative timescale and efficiency.

From these simulations, we find that applying a short field at relatively high peak intensity leads to a important norm loss in the water NGO complex of 0.09 directly after the laser pulse. It is also observed that thermalization of longer-lived partial charge transfer states can increase the PCET yield on the picosecond timescale. For the optimal combination found in this work (50 fs pulse with 3.51 10^{13} W/cm^2 peak intensity and a thermalization rate $\tau_\gamma = 1\,\text{ps}$), slightly more than a third of an ensemble of NGO-water complexes would undergo water splitting at room temperature. Comparing these timescales to the ultrafast hydrogen transfer time in a CT state, we observe that the rate of water splitting is strongly limited by the efficiency of the initial optical excitation, largely due to the rapid dephasing in the system. An intricate balance between non-adiabatic thermalization pathways and the hydrogen transfer indicates the importance of considering temperature and vibronic coupling in the design of such materials for applications in nanoscopic devices. From the probed vibronic coupling strengths, we conclude that thermalization lifetimes of the order of 1 ps are desirable for devices that are operating at room temperature. The thermalization lifetime, which is related to phonon lifetimes, could be controlled by optimizing dopant and defect concentrations in NGO catalysts, as well as by modifying the size of the active site.

Acknowledgements

We thank the Volkswagen foundation for financial support (Freigeist Fellowship No. 89525).

References

(1) Yoshikawa, K., Kawasaki, H., Yoshida, W., Irie, T., Konishi, K., Nakano, K., Uto, T., Adachi, D., Kanematsu, M., Uzu, H., Yamamoto, K. Silicon heterojunction solar cell with interdigitated back contacts for a photoconversion efficiency over 26%. *Nature Energy* **2017**, *2*, 17032.

(2) Gaspar, H., Figueira, F., Pereira, L., Mendes, A., Viana, J. C., Bernardo, G. Recent Developments in the Optimization of the Bulk Heterojunction Morphology of Polymer: Fullerene Solar Cells. *Materials* **2018**, *11*, 2560.

(3) Mosconi, D., Mazzier, D., Silvestrini, S., Privitera, A., Marega, C., Franco, L., Moretto, A. Synthesis and Photochemical Applications of Processable Polymers Enclosing Photoluminescent Carbon Quantum Dots. *ACS Nano* **2015**, *9*, 4, 4156.

(4) Testa, C., Zammataro, A., Pappalardo, A., Sfrazzetto, G. T. Catalysis with carbon nanoparticles. *RSC Adv.* **2019**, *9*, 27659.

(5) Morton, O. A new day dawning? Silicon Valley sunrise. *Nature* **2006**, *443*, 7107, 19.

(6) BP Statistical Review of World Energy 2019 (BP, **2019**); https://www.bp.com/content/dam/bp/business-sites/en/global/corporate/pdfs/energy-economics/statistical-review/bp-stats-review-2019-full-report.pdf (Accessed Sep. 7th, 2019).

(7) Chang, X., Wang, T., Gong, J. CO2 photo-reduction: insights into CO2 activation and reaction on surfaces of photocatalysts. *Energy Environ. Sci.* **2016**, *9*, 2177.

(8) Hammes-Schiffer, S. Proton-Coupled Electron Transfer: Moving Together and Charging Forward. *J. Am. Chem. Soc.* **2015**, *137*, 8860.

(9) Shimizu, T., Sugiura, M., Noguchi, T. Mechanism of Proton-Coupled Electron Transfer

in the S0-to-S1 Transition of Photosynthetic Water Oxidation As Revealed by Time-Resolved Infrared Spectroscopy. *J. Phys. Chem. B* **2018**, *122*, 9460.

(10) Wang, X., Maeda, K., Thomas, A., Takanabe, K., Xin, G., Carlsson, J.M., Domen, K., Antonietti, M. A metal-free polymeric photocatalyst for hydrogen production from water under visible light. *Nature Materials* **2009**, *8*, 76.

(11) Yeh, T.-F., Cihlář, J., Chang, C.-Y., Cheng, C., Teng, H. Roles of graphene oxide in photocatalytic water splitting. *Mater. Today* **2013**, *16*, 78.

(12) Ehrmaier, J., Karsili, T. N. V., Sobolewski, A. L., Domcke, W. Mechanism of Photocatalytic Water Splitting with Graphitic Carbon Nitride: Photochemistry of the Heptazine-Water Complex. *J. Phys. Chem. A* **2017**, *121*, 4754.

(13) Ehrmaier, J., Janicki, M. J., Sobolewski, A. L., Domcke, W. Mechanism of photocatalytic water splitting with triazine-based carbon nitrides: insights from ab initio calculations for the triazine–water complex. *Phys. Chem. Chem. Phys.* **2018**, *20*, 14420.

(14) Dreyer, D. R., Park, S., Bielawski, C. W., Ruoff, R. S. The chemistry of graphene oxide. *Chem. Soc. Rev.* **2010**, *39*, 228.

(15) Weber, F., Ren, J., Petit, T., Bande, A. Theoretical X-ray absorption spectroscopy database analysis for oxidised 2D carbon nanomaterials. *Phys. Chem. Chem. Phys.* **2019**, *21*, 6999.

(16) Chang, D. W., Baek, J.-B. Nitrogen-Doped Graphene for Photocatalytic Hydrogen Generation. *Chem. Asian J.* **2016**, *11*, 1125.

(17) Runge, E., Gross, E. K. U. Density-Functional Theory for Time-Dependent Systems. *Phys. Rev. Lett.* **1984**, *52*, 997.

(18) Tremblay, J. C., Klamroth, T., Saalfrank, P. Time-dependent configuration-interaction

calculations of laser-driven dynamics in presence of dissipation. *J. Chem. Phys.* **2008**, *129*, 084302.

(19) Delgado-Bonal, A. Entropy of radiation: the unseen side of light. *Sci. Rep.* **2017**, *7*, 1642.

(20) Neese, F. The ORCA program system. *WIREs Comput Mol Sci* **2012**, *2*, 73.

(21) Neese, F. Software update: the ORCA program system, version 4.0. *WIREs Comput Mol Sci* **2018**, *8*, 1327.

(22) Yanai, T., Tew, D. P., Handy, N. C. A new hybrid exchange–correlation functional using the Coulomb-attenuating method (CAM-B3LYP). *Chem. Phys. Lett.* **2004**, *393*, 51.

(23) Schäfer, A., Horn, H., Ahlrichs, R. Fully optimized contracted Gaussian basis sets for atoms Li to Kr. *Chem. Phys.* **1992**, *97*, 2571.

(24) Grimme, S., Antony, J., Ehrlich, S., Krieg, H. A consistent and accurate ab initio parametrization of density functional dispersion correction (DFT-D) for the 94 elements H-Pu. *J. Chem. Phys.* **2010**, *132*, 154104.

(25) Grimme, S., Ehrlich, S., Goerigk, L. Effect of the Damping Function in Despersion Corrected Density Functional Theory. *J. Comput. Chem.* **2011**, *32*, 1456.

(26) Neese, F., Wenmohs, F., Hansen, A., Becker, U. Efficient, approximate and parallel Hartree–Fock and hybrid DFT calculations. A 'chain-of-spheres' algorithm for the Hartree–Fock exchange. *Chem. Phys.* **2009**, *356*, 98.

(27) Weigend, F. Accurate Coulomb-fitting basis sets for H to Rn. *Phys. Chem. Chem. Phys.* **2006**, *8*, 1057.

(28) Cossi, M., Rega, N., Scalmani, G., Barone, V. Energies, Structures, and Electronic Properties of Molecules in Solution with the C-PCM Solvation Model. *J. Comput. Chem.* **2003**, *24*, 669.

(29) Rappoport, D., Furche, F. Property-optimized Gaussian basis sets for molecular response calculations. *J. Chem. Phys.* **2010**, *133*, 134105.

(30) Martin, R. L. Natural transition orbitals. *J. Chem. Phys.* **2003**, *118*, 4775.

(31) Klamroth, T. Laser-driven electron transfer through metal-insulator-metal contacts: Time-dependent configuration interaction singles calculations for a jellium model. *Phys. Rev. B* **2003**, *68*, 245421.

(32) Vanne, Y.V. and Saenz, A. Numerical treatment of diatomic two-electron molecules using a B-spline based CI method. *J. Phys. B: At. Mol. Opt. Phys.* **2004**, *37*, 4101.

(33) Greenman, L., Ho, P.J., Pabst, S., Kamarchik, E., Mazziotti, D.A., Santra, R. Implementation of the time-dependent configuration-interaction singles method for atomic strong-field processes. *Phys. Rev. A* **2010**, *82*, 023406.

(34) Hermann, G., Tremblay, J.C. Ultrafast photoelectron migration in dye-sensitized solar cells: Influence of the binding mode and many-body interactions. *J. Chem. Phys.* **2016**, *145*, 174704.

(35) Klinkusch, S., Tremblay, J. C. Resolution-of-identity stochastic time-dependent configuration interaction for dissipative electron dynamics in strong fields. *J. Chem. Phys.* **2016**, *144*, 184108.

(36) Hermann, G., Pohl, V., Tremblay, J.C. An open-source framework for analyzing N-electron dynamics. II. Hybrid density functional theory/configuration interaction methodology. *J. Comput. Chem.* **2017**, *38*, 2378.

(37) Tremblay, J. C., Carrington Jr., T. Using preconditioned adaptive step size Runge-Kutta methods for solving the time-dependent Schrödinger equation. *J. Chem. Phys.* **2004**, *121*, 11535.

(38) Tremblay, J.C., Klinkusch, S., Klamroth, T., Saalfrank, P. Dissipative many-electron dynamics of ionizing systems. *J. Chem. Phys.* **2011**, *134*, 044311.

(39) Hermann, G., Pohl, V., Tremblay, J.C., Paulus, B., Hege, H.-C., Schild, A. ORBKIT: A modular python toolbox for cross-platform postprocessing of quantum chemical wavefunction data. *J. Comput. Chem.* **2016**, *37*, 1511.

(40) Pohl, V., Hermann, G., Tremblay, J.C. An open-source framework for analyzing N - electron dynamics. I. Multideterminantal wave functions. *J. Comput. Chem.* **2017**, *38*, 1515.

(41) Hermann, G., Tremblay, J. C. Laser-Driven Hole Trapping in a Ge/Si Core-Shell Nanocrystal: An Atomistic Configuration Interaction Perspective. *J. Phys. Chem. C* **2015**, *119*, 25606.

Selbstständigkeitserklärung

Hiermit erkläre ich, dass ich die vorliegende Arbeit selbstständig verfasst habe und keine anderen als die aufgeführten Hilfsmittel und Quellen verwendet habe. Alle Ausführungen, die aus anderen Werken übernommen wurden, wurden als Quellen kenntlich gemacht.

Zusätzlich versichere ich, dass diese Dissertation nur in Zusammenhang mit diesem Promotionsverfahren steht und diese Arbeit in keiner anderen Form vorher veröffentlich wurde.